Advanced Computational Electromagnetics for Metasurfaces

Original
Advanced Computational Electromagnetics for Metasurfaces / Verni', Francesco. - (2020 Aug 25), pp. 1-96.

Publisher:
Politecnico di Torino

Published
DOI:

ScuDo
Scuola di Dottorato ~ Doctoral School
WHAT YOU ARE, TAKES YOU FAR

Doctoral Dissertation
Doctoral Program in Electrical, Electronics and Communications Engineering

Advanced Computational Electromagnetics for Metasurfaces

Francesco Vernì

* * * * * *

Supervisor
Prof. G. Vecchi

Doctoral Examination Committee:
Prof. D. R. Wilton, University of Houston
Prof. M. J. Mencagli, University of North Carolina

Politecnico di Torino
April 29, 2020

I hereby declare that, the contents and organisation of this dissertation constitute my own original work and does not compromise in any way the rights of third parties, including those relating to the security of personal data.

. . . .
Francesco Vernì
Turin, April 29, 2020

Summary

This Thesis work has been devoted to numerical methods for the design of metamaterial antennas, and in particular to its relevant meta-surface (MS) version. Metamaterials, and especially metasurfaces, have been one of the most relevant recent additions to the design of electromagnetic devices, and in particular antennas.

Metasurface antennas are based on sub-wavelength textures- usually called *unit cells* - and extend to sizeable electrical lengths. This makes their full-wave (i.e. unapproximated) analysis challenging. However, the effect of the sub-wavelength texturing is well approximated, on the relevant wave scale, by a homogenized impedance boundary condition (IBC). Numerical analysis with the IBC is a lot less demanding than the analysis of the actual layout of the antenna, but IBC is especially important in the design phase of the antenna.

Designing the antenna via the spatial profile of the IBC allows to break the design task in two: 1) design of the IBC distribution; 2) design of the individual unit cells that locally yield the desired value of the surface impedance.

Throughout, the background numerical formulation of the problem has been in terms of surface integral equations (IEs), that is commonly called "Method of Moments" (MoM); it is discretized with finite elements defined on triangles and known as Rao-Wilton-Glisson (RWG) functions. The MoM operations are carried out with an FFT-based fast factorization.

The design is approached as an optimization process for the spatial distribution of the IBC; use of full-wave simulation in this optimization cycle is made possible by aggregating the underlying RWG functions into entire-domain basis functions, in the form of waveguide modes. It is shown that this is advantageous in terms of the total numerical resources required in the optimization process. The scheme is applied to the design of two relevant classes of metasurface antennas.

The important issue of the structure needed to launch the wave that then propagates on the IBC radiating surface is then addressed. Finally, solutions obtained with the IBC and the full layout are compared with one another, and against measured data of realized antennas.

Acknowledgements

The author is extremely thankful to Dr Francavilla for his essential support in the early stage of this work. Special acknowledgements also to Dr Righero and Dr Scarabosio for being excellent collaborators and co-authors of the work presented in this thesis. Thanks to all the collaborators at the LINKS foundation and the LACE group in Turin. Thanks to Professor Grbic for having always made me feel an active member of his outstanding research group at the University of Michigan. Thanks to Professors Maci, Martini, Albani — my very first mentors at the University of Siena — and the people of Wave-Up. They shared relevant information about the test cases. Thanks to the referees for having chosen to dedicate their precious time to review the manuscript. Last but *first*, thanks to my *maestro* Professor Vecchi; life would have been *tougher* without your inestimable teachings.

Contents

List of Tables

List of Figures

Chapter 1

Overview

This chapter has the purpose of charting a roadmap of the research carried out and reported in this thesis document. The chapter aims to sketch the "big picture", and will dispense with systematic referencing — all relevant literature is referenced instead in the other chapters.

The entire work has been devoted to numerical methods for the design of metamaterial antennas, and in particular to its relevant meta-surface (MS) version. Metamaterials, and especially metasurfaces, have been one of the most relevant recent additions to the design of electromagnetic devices, and in particular antennas. These antennas, at least in the microwave to the mm-wave range, are made out of standard materials (e.g. metalized dielectric slabs), and realized with standard fabrication technologies (like printed circuit board), yet being well suited to fabrication with advanced manufacturing like 3D printing in some cases. Apart from the build-up inherent in the *meta* prefix, metasurfaces have emerged instead as a very valuable *paradigm* to understand complex wave phenomena, and to *design* components, and especially antennas, that simply did not exist before — like flat, centre-fed, low-loss, high-gain broadside radiating antennas.

Metasurface antennas are based on sub-wavelength textures — usually called *unit cells* — and extend to sizeable electrical lengths. This makes their full-wave (i.e. unapproximated) analysis challenging (and often difficult to attack with standard commercial solvers). However, the effect of these sub-wavelength texturing is well-approximated, on the relevant wave scale, by a "smeared out", homogenized impedance boundary condition (IBC). This IBC is a continuous distribution, and it is usually spatially varying- or "modulated"- to generate the desired radiation properties. Modulation is on a relatively slow scale, comparable with the free-space wavelength. As a result, numerical analysis with the IBC is a lot less demanding than the analysis of the actual layout of the antenna; however, that task is not doable with all commercial software, and at any rate, will require some care (see below).

However, the real power the IBC description is in the *design* of MS components. Designing the antenna via the spatial profile of the IBC allows one to break the design task in two: 1) design of the IBC distribution; 2) design of the individual unit cells that locally yield the desired value of the surface impedance. The latter task is usually done in the approximation of local periodicity; in the typical procedure, one chooses a given unit-cell geometry, described by a few parameters (e.g. a tilted ellipse) and maps the value of achieved impedance over these; design of the unit cells is then achieved with lookup tables or more sophisticated mappings. It is easy to gain an advantage over the full design in which all parameters of all unit cells need to be determined simultaneously, with the full-wave solution at each step. Indeed, to this date, such a full process has not yet been reported in the open literature.

The work reported here has addressed design-oriented numerical methods for the analysis of metasurface antennas. Throughout, the background numerical formulation of the problem has been in terms of surface integral equations (SIE), discretized with (finite) boundary elements (BEM); that is commonly called "Method of Moments" (MoM) in the antenna community. The structures of interest are made of metal patches or slots on a (thin) layered dielectric, and the latter is approximated as infinitely extended; it is well known that this significantly reduces the necessary numerical effort without missing any of the relevant phenomena. The unknown field quantity is a surface current density (both for the simulation of the actual metalizations and for the IBC approximation); it is expressed as a linear combination of finite elements defined on triangles and well known as Rao-Wilton-Glisson (RWG) functions.

The baseline MoM is known to have intractable numerical costs for large problems; here, we aim at numbers of unknowns upward of 100K. The so-called Fast Factorization approaches, based on the convolutional nature of the kernel of the IE, are then mandatory. Here we will use an FFT-based scheme.

Most of this work will deal with the Impedance Boundary Condition (IBC) approximation, coherently with the design orientation, and in particular most of chapters 2 and 3. Indeed, the basic integral-equation formulation for the approximation of IBC is outlined in Chap. 2. The employed formulation involves the "transparent" version of the IBC; unlike its "opaque" (one-sided) version, it requires full modeling of the (grounded) slab, but this turns out to be necessary to afford a stable MoM system.

Chapters 2 and 3 employ entire-domain basis functions in the form of waveguide modes. These are however dealt with as "aggregate" basis functions, i.e. as linear combinations of the RWG of the underlying discretization. This has a number of advantages, i.e. use of existing and well-tested code, and availability of fast factorization for all involved algebra. The advantage of these entire-domain basis functions is primarily in the reduced number required to represent typical solutions with respect to RWG. However, no aggregate function set can escape the $\mathcal{O}(N^2)$ asymptotic limit in matrix fill time and $\mathcal{O}(N^3)$ solve time (although the latter appears later)[1], where N is

---

[1] A. Freni, P. De Vita, P. Pirinoli, L. Matekovits and G. Vecchi, "Fast-Factorization Acceleration of MoM Compressive Domain-Decomposition," *IEEE Transactions on Antennas and Propagation*, vol. 59, no. 12, pp. 4588-4599, Dec. 2011.

the number of underlying RWG. Instead, the reason why this approach is convenient is primarily (and contrary to some current opinions) because of its *cumulative* advantage in optimization instances, where multiple solutions are necessary. This is described in Chap. 2, and put in practice in the optimizations of Chap. 3.

Chapter 4 deals with the full metalization layout (unit cell), and the important issue of the structure to launch the wave that then propagates on the IBC radiating surface. Solutions obtained with IBC and the full layout are compared with one another and against measured data of realized antennas. The feeding structure almost invariably involves vertical metalizations, that are known to slow the solution in the layered-medium formulation; an ad-hoc factorization is then described to ease that burden.

Chapter 2

On the Use of Entire-Domain Basis Functions and Fast Factorizations for the Design of Modulated Metasurface

This chapter reports the pre-print version of the published article [40].
Entire-domain, spectral basis functions have witnessed recent interest in the integral-equation (IE) analysis of large metasurface (MS) antennas modeled via homogenized impedance boundary conditions (IBC). We present a formulation employing classical Galerkin test via Rao-Wilton-Glisson (RWG) functions, yet assembled to represent entire-domain div-conforming basis functions for the shape of interest (e.g. circular/coaxial WG modes). On the one hand, the rationale is that entire-domain, spectral basis functions afford a significant economy in the number of necessary unknowns; on the other hand, being expressed as combination of RWG functions, reaction integrals are computed with optimum cost via fast methods. This is applied to reduce the cost of the optimization process used to design MS antennas based on spatially modulated reactance profiles. The authors support the method proposed, presenting criteria to define the entire domain functions, considering the overall numerical complexity in an optimization framework, and providing convergence analysis and numerical results for holographic leaky-wave antennas, relevant in the MS context.

2.1 Introduction and Motivations

In this chapter we show the use of entire domain basis functions (EBF) for the surface integral equation (SIE) analysis and design of metasurfaces. Metasurfaces are planar single- or multi-layer configurations of electrically thin metamaterial composed of sub-wavelength building blocks usually printed on dielectric (e.g. [1]) or more recently metal-only manufactured (e.g. [7]). Due to their peculiar ability to manipulate electromagnetic waves in microwave and optical regimes, metasurfaces find an extensive range of applications for blocking, absorbing, concentrating, dispersing, or guiding waves [4].

In the initial stages of the design, MS are typically described through IBC, leading to the definition of a spatially variable surface impedance tensor [2]. It is worth noting that different boundary conditions such as the generalized sheet transition conditions (GSTC) [6, 8] can be defined and adopted for a more general description of the MS [39].

Moreover, MS antenna radiation is well described in terms of a continuous slowly varying electric sheet tensorial reactance interacting with a surface wave, which is gradually transformed into a leaky wave [14]. The typical design of MS antennas starts from an approximate analytic determination of the surface impedance, which allows the antenna to radiate a required field. This is followed by the optimization phase, which of course requires the numerical solution for each intermediate profile until the radiated field fits within the given field-mask. This means that all the cost function evaluations during the optimization involve the solution of the associated integral equation for variable impedance profiles but always for the same geometry (i.e. antenna shape). The goal of an efficient optimization is therefore to minimize the numerical cost associated to the entire optimization cycle, as opposed to that for a single solution.

This goal is here pursued by the combination of a “background” standard full-wave fast-solver for the SIE— based on the transparent IBC-electric field integral equation (EFIE) [18] and RWG basis function [24]—and a set of orthogonal (or quasi-orthogonal) entire-domain basis functions. This “spectral” basis allows a significant reduction in the number of unknowns necessary for a given quality of the results; the open issue with this basis is how to compute the associated reaction integrals (entries of the system matrix stemming from Galerkin test). The latter task is here performed using a fast solver that can handle large planar structure with (proven) optimal computational cost [5].

Entire domain basis functions have been revamped recently in the context of MS analysis [29, 19, 20, 21]. These basis functions are typically associated with the spectral domain version of the MoM solution to the SIE. In order to be effective, this usually implies that the two-fold Fourier transform of the basis/test functions has to be known in a form that allows a fast numerical evaluation of the reaction integrals [22, 17]. Closed form EBF are readily available from WG theory (e.g. [30]) as orthogonal modes satisfying Neumann or Dirichlet boundary conditions and known for several separable geometries. A generalization of these modes has also been introduced by the authors of [15, 16] to deal with arbitrary shapes and include the field singularity at the edge.

WG modes, under certain conditions, yield div-conforming basis functions as required for the EFIE part of the SIE. For canonical shapes, non div-conforming bases have been devised for which only the coplanar reaction integrals are evaluated in closed form; this was done for circular [29, 20], or the stretched elliptical version [21]. A closed form spectral solution might look appealing for our purpose, however there are interesting configurations for which the reaction integrals have been not computed, such as when two MS are cascaded along the z-axis (i.e. [35, 36]) or the MS is composed of portion of canonical geometries (i.e. [23]). In this work we do not need to know the Fourier transform of the EBF since the reaction integrals are evaluated between conventional RWG basis/test functions using space domain Green's functions for multi-layered media [31].

The electrical dimension of a MS antenna is often tens of wavelengths; therefore the number of unknowns when using RWG basis functions is very large, especially because high permittivity substrates are typically considered. The iterative solution necessarily implied by a fast-factorization solver with a large number of DoF has a cost that renders the optimization process very expensive; moreover, the linear systems to be solved are often poorly conditioned. Conversely, spectral basis functions defined over the whole antenna result in reducing the number of necessary DoF, and in a regularization of the systems [11]. On the whole, the use of these functions accelerates repeated solutions.

As mentioned before, in this work we compute the reaction integrals for the entire-domain basis functions, via projection onto the usual RWG space. This allows a considerable flexibility and more complex geometries, e.g. annular rings, by simply using the WG modes associated to the relative support. The annular (ring) geometry is especially relevant in practice, as often the feeding region of the antenna is not part of this design stage and the actual geometry of circular MS antennas is annular instead of a full circle; on the other hand, the spectral basis for this case is simply the set of the Coaxial WG modes.

The remainder is organized as follows: in sect. 2.2, we discuss how to use the transparent IBC-EFIE discretization scheme in an optimization framework, in which a different IBC profile is considered at each optimization step. In sect. 2.3, div-conforming entire-domain basis functions are build from the WG theory and used to factorize the IBC-EFIE MoM system. In sect. 2.4 we present the criteria guiding the WG mode set is selection. The sect. 2.5 explains the advantages of the system compression when the reaction integrals between EBF are computed from reaction integral between RWG functions expressed in a fast factorization. Moreover, we show an example of the regularization effect of the EBF compression. In sect. 2.7, we present a convergence analysis of the compressed IBC-EFIE and numerical results with scalar and tensorial holographic MS antenna, which validate the method for circular and annular-ring domains. Preliminary results about circular domains are presented in the conference paper [9]. The notation used in this paper is summarized in the Appendix A for the sake of consistence and conciseness.

2.2 MoM Formulation

Different numerical approaches have been studied and adopted for the simulation of MS antennas based on guided surface waves. Most of them suffer from instability problems in the cases of interest, while the penetrable model of the IBC, which only models the thin sheet of patches, together with an EFIE yields a stable discretization and accurate results [18]. Hence, we adopt the transparent IBC-EFIE with mixed element surface discretization (i.e. via RWG basis/test functions [24]) together with a fast Fourier transform (FFT) based fast-solver for planar structures (i.e. GIFFT method [5]). The MS is represented by an electrically thin planar surface Σ with $\hat{\boldsymbol{z}}$ as its (outward) normal unit vector. Here, penetrable boundary conditions relates the fields on both sides of Σ as:

$$\boldsymbol{E}_t^{av}|_\Sigma = \frac{1}{2}\left(\boldsymbol{E}_{\Sigma^+} + \boldsymbol{E}_{\Sigma^-}\right) = \boldsymbol{\mathcal{Z}}_s \cdot \left[\hat{\boldsymbol{z}} \times \left(\boldsymbol{H}_{\Sigma^+} - \boldsymbol{H}_{\Sigma^-}\right)\right] \tag{2.1}$$

where the superscript *"av"* stands for "average", indicating that we evaluate the average of the E-field on either sides, Σ^+ and Σ^-, of the MS. The tensorial sheet impedance, $\boldsymbol{\mathcal{Z}}_s$, is defined and spatially modulated all over Σ. The tensor $\boldsymbol{\mathcal{Z}}_s$ is denoted by a bold and calligraphic font. More details about the formulation can be found in [18]. The SIE formulation for the equivalent current $\boldsymbol{J}$,

$$\boldsymbol{J} = \hat{\boldsymbol{z}} \times \left(\boldsymbol{H}_{\Sigma^+} - \boldsymbol{H}_{\Sigma^-}\right), \tag{2.2}$$

reads:

$$Z_0 \hat{\boldsymbol{z}} \times \hat{\boldsymbol{z}} \times \boldsymbol{\mathcal{L}}(\boldsymbol{J}) - \boldsymbol{\mathcal{Z}}^s \cdot \boldsymbol{J} = \hat{\boldsymbol{z}} \times \hat{\boldsymbol{z}} \times \boldsymbol{E}^i \tag{2.3}$$

with $Z_0 = \sqrt{\mu_0/\varepsilon_0}$ the wave impedance in vacuum, $\boldsymbol{E}^i$ the incident field, and

$$\boldsymbol{\mathcal{L}}(\boldsymbol{f}) = \int_\Sigma \boldsymbol{\mathcal{G}}^{\boldsymbol{EJ}}(\boldsymbol{r}, \boldsymbol{r}') \cdot \boldsymbol{f}(\boldsymbol{r}') d\boldsymbol{r}' \tag{2.4}$$

the Electric Field Integral Operator (EFIO) with $\boldsymbol{\mathcal{G}}^{\boldsymbol{EJ}}$ the multi-layer dyadic Green's function when only electric sources are considered. The multi-layer formulation employed in the remainder is the mixed-potential "Formulation-C" introduced by Michalski et al. in [31]. We approximate the unknown current $\boldsymbol{J}$ as a linear combination of N_Λ RWG basis function $\boldsymbol{\Lambda}_\ell$, namely

$$\boldsymbol{J} \approx \boldsymbol{J}^\Lambda = \sum_{\ell=1}^{N_\Lambda} J_\ell^\Lambda \boldsymbol{\Lambda}_\ell, \tag{2.5}$$

and we test the integral equation (2.3) on the same RWG functions $\boldsymbol{\Lambda}_m$, with $m = 1, \ldots, N_\Lambda$, in a classical Galerkin fashion (MoM), obtaining the linear system

$$\left(\underline{\underline{Z}} - \underline{\underline{Z}}^s\right) \underline{J}^\Lambda = \underline{b}^\Lambda, \tag{2.6}$$

where the matrices entries are:

$$\begin{aligned} Z_{m\ell} &= \langle \boldsymbol{\Lambda}_m ; \boldsymbol{\mathcal{G}}^{\boldsymbol{EJ}} ; \boldsymbol{\Lambda}_\ell \rangle \\ Z_{m\ell}^s &= \langle \boldsymbol{\Lambda}_m ; \boldsymbol{\mathcal{Z}}^s \cdot \boldsymbol{\Lambda}_\ell \rangle. \end{aligned}$$

The m-th element of the right-hand side is:

$$b_m^\Lambda = \langle \mathbf{\Lambda}_m; \boldsymbol{E}^i \rangle. \tag{2.7}$$

Due to the large electrical size of the structures, this discretization based on RWG functions cannot be used in practice in optimization problems, even using a fast-solver. The use of EBF reduces the dimension of the system matrix and often allows for a direct inversion, which, when possible, bypasses some issues arising from the use of iterative methods, and keeps the complexity of the single solution negligible compared to the overall complexity of the whole optimization process.

On one hand, letting $\mathbf{\Psi}_\ell$ be the ℓ-th EBF to be used to approximate the solution $\boldsymbol{J}$,

$$\boldsymbol{J} \approx \boldsymbol{J}^\Psi = \sum_{\ell=1}^{N_\Psi} J_\ell^\Psi \mathbf{\Psi}_\ell, \tag{2.8}$$

Galerkin testing of (2.3) with basis functions $\mathbf{\Psi}_\ell$ leads to a system formally identical to (2.6). This is the case of [29, 19, 20, 21].

On the other hand, if EBFs $\mathbf{\Psi}_\ell$, with $\ell = 1, \ldots N_\Psi$, are expressed as a linear combination of RWG basis functions,

$$\mathbf{\Psi}_\ell = \sum_{p=1}^{N_\Lambda} \Psi_{p\ell} \mathbf{\Lambda}_p, \tag{2.9}$$

all terms in the entire-domain basis MoM can be expressed using terms appearing in the RWG MoM. This can be done by weighted residual procedure, enforcing that the difference between $\boldsymbol{J}^\Lambda$ and $\boldsymbol{J}^\Psi$ is outside the space spanned by the RWG set, i.e. zero when tested over the set of RWG $\mathbf{\Lambda}_p$, with $p = 1, \ldots, N_\Lambda$:

$$\langle \mathbf{\Lambda}_p, \boldsymbol{J}^\Lambda - \boldsymbol{J}^\Psi \rangle = 0. \tag{2.10}$$

which results in the linear system

$$\underline{\underline{\Psi}}^T \left(\underline{\underline{Z}} - \underline{\underline{Z}}^s \right) \underline{\underline{\Psi}}\, \underline{J}^\Psi = \underline{\underline{\Psi}}^T \underline{b}^\Lambda, \tag{2.11}$$

where $\underline{\underline{\Psi}}$ is the basis change matrix containing the coefficients $\Psi_{p\ell}$ in (2.9). The basis change matrix entries of course depend on the chosen EBF, but also on how these latter are projected on the RWG space. We will explicitly deal with both points in sect. 2.3.3.

For any further use, once the coefficients J_ℓ^Ψ have been determined, the current can be easily expressed using RWG functions as

$$\boldsymbol{J}^\Psi = \sum_{p=1}^{N_\Lambda} \left(\sum_{\ell=1}^{N_\Psi} \Psi_{p\ell} J_\ell^\Psi \right) \mathbf{\Lambda}_p, \tag{2.12}$$

From (2.11) it appears clear that once we have computed $\underline{\underline{\Psi}}$ and $\underline{\underline{Z}}$ and stored $\underline{\underline{\Psi}}^T \underline{\underline{Z}}\, \underline{\underline{\Psi}}$, if we want to change the values of $\underline{\underline{Z}}^s$, the only computation needed is related to the latter matrix which has a negligible cost (i.e. scaling as the cost of matrix-vector product with a Gram matrix).

Hence, the system looks well suited for being solved multiple times, each time with different values of the tensorial sheet impedance, $\boldsymbol{\mathcal{Z}}_s$. In fact, an optimization algorithm will generally look for the optimal spatial modulation of the sheet impedance $\boldsymbol{\mathcal{Z}}^s$, with a cost function defined by typical antenna design parameters (i.e. Maximum Directivity, SSL, etc.) depending on the far-field of the obtained solution. Different optimization algorithms may be used (e.g. Genetic, Particle Swarm, Simulated Annealing), but, in any case, all of them require the evaluation of far-field for current distributions obtained from different impedance profiles. A rapid computation of these currents is then mandatory for an efficient optimization.

2.3 Div-Conforming Entire-Domain Basis Functions

The use of MS implies sub-wavelength geometrical details [4, 6] all over, and MS antennas are usually electrically very large. It follows that MS are intrinsically a multiscale problem; however, a consistent body of literature has shown that most of the design can be done via MS homogenization with IBC: the associated problem is then at a macroscale, with impendance modulations on the scale of the wavelength. This makes it possible to tackle the optimization task with full-wave solutions of the "approximate" (IBC) model. At this macroscale, in fact, the number of spatially-resolved basis functions, namely RWG, is tolerable; however, "macro" basis functions with spectral resolution can afford a further reduction of the necessary degrees of freedom, which is crucial in an optimization endeavor. A pictorial rendering summarizing the considered scenario is shown in Fig. 2.1.

We analyze here how to build div-conforming EBF, well suited for dealing with the IBC-EFIE, and their practical implementation in MoM codes.

2.3.1 Div-Conforming Enforcement

Div-conforming EBF can be obtained directly from WG modes. As $\boldsymbol{J} = \hat{\boldsymbol{n}} \times \boldsymbol{H}$, with $\boldsymbol{J}$ an electric current, $\hat{\boldsymbol{n}}$ the unit vector normal to the WG cross section, and $\boldsymbol{H}$ the magnetic field, it is convenient to define WG-type basis functions via the magnetic eigenfunctions, namely $\mathbf{h}$ in [30]. The WG eigenmodes are continuous with bounded derivatives everywhere in the interior of the WG cross section (in fact, they are infinitely continuous), but with a possible jump at the domain boundary, since $\boldsymbol{J}$ must be zero outside the domain; hence, the div-conforming requirement amounts to requiring that $\boldsymbol{J}$ has vanishing normal component at the domain boundary. This corresponds to vanishing tangent $\boldsymbol{H}$ field, or PMC, boundary condition to the transverse Helmholtz eigenproblem. With $\hat{\boldsymbol{n}} = \hat{\boldsymbol{z}}$, the sought for $\hat{\boldsymbol{z}} \times \mathbf{h}$ are the electric eigenfunctions, $\mathbf{e} = \hat{\boldsymbol{z}} \times \mathbf{h}$. In turn, it is easy to see [17] that the electric eigenfunctions $\mathbf{e}$ for the present PMC wall corresponds to the magnetic eigenfunctions $\mathbf{h}$ for the PEC wall, with TE and TM interchanged. Being div-conforming, these basis functions correctly express the Electric Field Integral Operator, and are able to approximate the entire solution space [17].

2.3.2 Geometry

As for the geometry, while circular domains cover most current antenna designs, it is worth noting that many other different geometries (e.g. triangular, rectangular, annular, elliptical) and portions thereof, can be explored by applying the same considerations

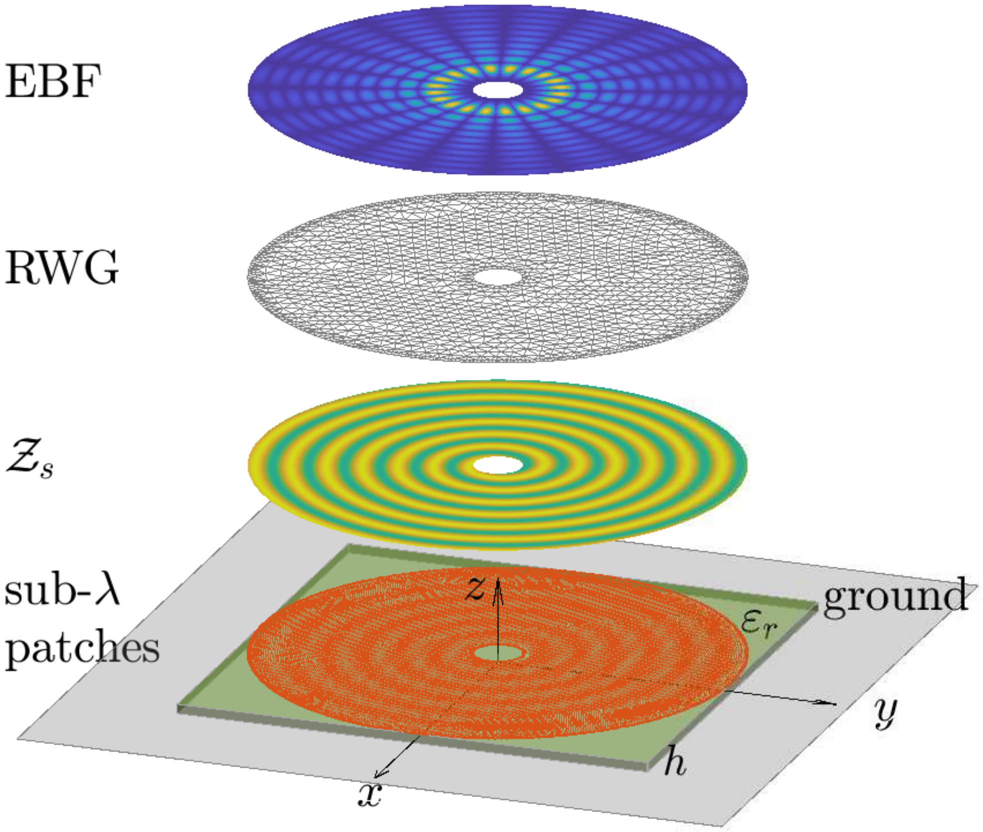

Figure 2.1: On the bottom, a representation of a sub-wavelength metallic patch arrangement printed in an annular region on a grounded dielectric slab (thickness h_d and and permittivity ε_r). Floating on the top, a possible homogenized impedance profile with spiral shape (and annular support) defined at the upper interface of the grounded dielectric slab. Moving up, RWG spatial discretization and CXWG spectral discretization, respectively.

adopted in the following. In this article, both circular and annular EBFs are used. As the region around the feed structure is typically left non patterned, it is convenient to avoid having to define the impedance there. Keeping the current on the feeding region may lead to unphysical solutions, especially when an optimization algorithm looks for optimal impedance values out of the actual domain of the impedance, which is annular. This issue is effectively solved with basis functions defined on an annular domain.

The functions composing $\mathbf{h}$ can be explicitly found in chapter 2 of [30] for rectangular, circular, coaxial (i.e. annular) and elliptical WG. Both circular and coaxial modes follow a double indexing mn for the zeros of the axial (m) and radial (n) components which is shown for the coaxial case also in Fig.2.2. To put the reader at ease, details about $\mathbf{h}$ are reported in Appendix B.

2.3.3 Basis Change Matrix Entries

The analytic expression of the ℓ-th mode, $\mathbf{h}_\ell$, is used to find the RWG representation of the EBF $\boldsymbol{\Psi}_\ell$ used in (2.11). The coefficients $\Psi_{p\ell}$, with $p = 1, \ldots, N_\Lambda$, are obtained via weighted-residual, enforcing that the difference between the analytic expression $\mathbf{h}_\ell$ and its RWG representation $\boldsymbol{\Psi}_\ell$ be outside the space spanned by the RWG set,

$$\langle \boldsymbol{\Lambda}_q ; \mathbf{h}_\ell - \boldsymbol{\Psi}_\ell \rangle = 0, \ \ \forall q = 1, .., N_\Lambda. \tag{2.13}$$

By writing $\boldsymbol{\Psi}_\ell$ as in (2.9) and rearranging the terms, we have the linear system

$$\sum_{p=1}^{N^\Lambda} \Psi_{p\ell} \langle \boldsymbol{\Lambda}_q ; \boldsymbol{\Lambda}_p \rangle = \langle \boldsymbol{\Lambda}_q ; \mathbf{h}_\ell \rangle, \ \ \forall q = 1, .., N_\Lambda, \tag{2.14}$$

to be solved for $\Psi_{p\ell}$. Each column of the matrix $\underline{\underline{\Psi}}$ is then obtained solving (2.14). This step represents a negligible computational cost, as the Gram matrix $\langle \boldsymbol{\Lambda}_q ; \boldsymbol{\Lambda}_p \rangle$ in the left-hand side of (2.14) is very sparse, positive-definite, and with condition number $\mathcal{O}(1)$, so that convergence with an iterative solver (e.g. Conjugate Gradient) is attained within few iterations.

2.4 Mode Set Selection

As already recognized in [20], for radiation assessment, the solution can in principle be restricted to spatial frequencies up to free-space wavenumber k_0. Spectral filtering is intrinsically more stable with spectral bases (i.e. orthogonal entire-domain basis functions) than with RWG (this can be ascertained elaborating on the results in [10] and [11]). We employ here a more conservative spectral truncation, to capture the spatial variations implied in the surface wave manipulation of the surface wave on the MS antenna. As the EFIE operator is a high-pass, and its inverse a low-pass, we choose the spectral content of the basis so as to correctly represent the term associated to the modulated surface impedance (this is akin to the physical optics (PO) part of the magnetic field integral equation (MFIE)).

Based on the spectral content of the impedance profile, a-priori spectral truncation can be assumed in order to select a conservative number of modes which also guarantees an acceptable error on the far-field. In order to estimate the number of modes to retain in the compression, empirical tests to represent possible impedance profiles along radial and axial cuts with a certain number of modes can be performed at a negligible cost. Conservative selections are taken to guarantee that the modes will be able to describe (up to a certain approximation error) the full-wave solution. The plot in Fig. 2.2 represents the spectral division adopted throughout the paper when an impedance profile

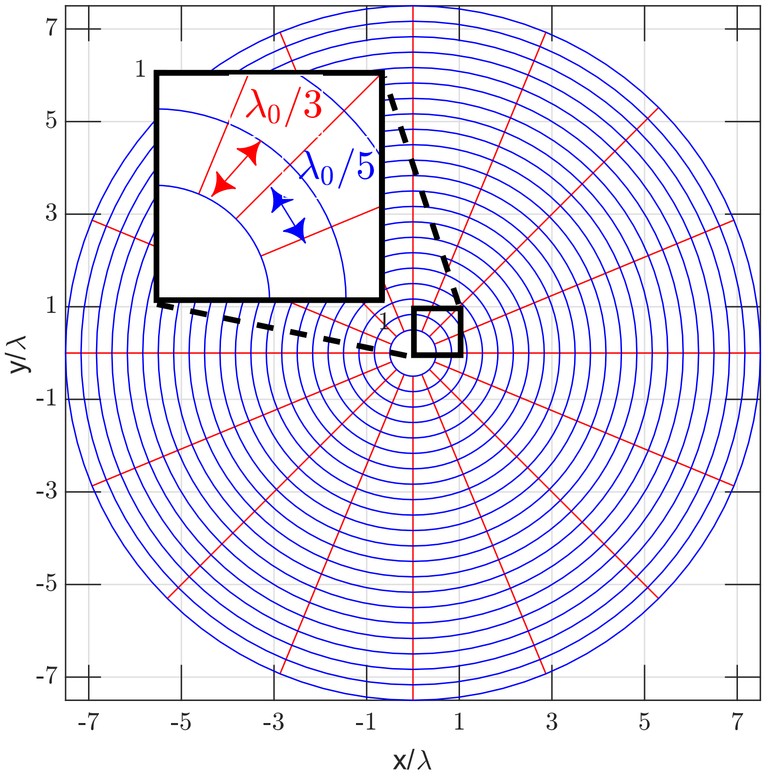

Figure 2.2: Map of the zeros along radial (blue) and axial (red) components of the highest order mode used in this work for an annular antenna of radius $7.5\lambda_0$, λ_0 is the free-space wavelength. The chosen order allows to follow a $\lambda_0/3$ spatial variation along $\hat{\boldsymbol{\rho}}$ and a $\lambda_0/5$ spatial frequency variation along $\hat{\boldsymbol{\phi}}$ at the inner radius: $\lambda_0/2$. At these spatial frequencies, the total number of modes along $\hat{\boldsymbol{\rho}}$ and $\hat{\boldsymbol{\phi}}$ are 22 and 8, respectively, which results in $N_\Psi = 742$.

defined on a annular region and having a strong symmetry along the ϕ axis is considered. In this case, only a few axial modes are needed to accurately describe the axial variation of the impedance and consequently the MoM solution. Further considerations about the number of modes are presented in sect. 2.5 and Sec. 2.7.

Finally, a related consideration has to be made about the minimal underlying RWG discretization to be used in association with the use of the entire-domain spectral basis. It is apparent that the spatial discretization, i.e. the RWG mesh edge size, has to be sufficient to correctly describe the highest spatial frequency involved in the spectral basis.

2.5 Compression

In this section we discuss two important issues of the proposed method: a) the overall numerical complexity of the implied system matrix compression, and b) the regularization effect of the basis.

The spectral basis representation drastically compresses the system allowing computation of compressed solution for various impedance profiles at the cost of $\mathcal{O}(N_\Psi^3)$; this cost could be lowered using an iterative solver, as we will see that the spectral basis significantly improves convergence, but we will retain the assumption of direct factorization. On the other hand, the computational cost of the compression is $\mathcal{O}(N_\Psi N_\Lambda \log(N_\Lambda) + N_\Lambda N_\Psi^2)$. This cost is due to the N_Ψ -based matrix-vector multiplications needed to perform the $\underline{\underline{Z}}\,\underline{\underline{\Psi}}$ part, followed by matrix-matrix multiplication of the $N_\Lambda \times N_\Psi$ matrix $\underline{\underline{\Psi}}^T$ by the $N_\Psi \times N_\Lambda$ matrix $\underline{\underline{Z}}\,\underline{\underline{\Psi}}$. This constitutes an initial overhead that has to be recovered during optimization, and thus sets the break-even. This point is examined in Fig. 2.3, which reports an estimate of the computational cost of repeated solutions, as needed by an optimization algorithm, as a function of the number of optimization steps. Data refer to a circular support with different radii, with dielectric constant $\varepsilon_r = 6.15$; Λ indicates RWG solutions, Ψ EBF solutions. The number of radial modes allows to follow a $\lambda_0/3$ spatial frequency variation along $\hat{\boldsymbol{\rho}}$, as shown before in Fig. 2.2. For all examined sizes (radii), the computational advantage is in excess of a factor of 10.

2.6 Numerical Regularization

The proposed use of a spectral basis aides the convergence, yielding a stable well-conditioned system. These enhanced performances apply to both the convergence rate when using iterative solvers for the system solution, and the stability of the solution with respect to mesh size.

In the metasurface context, standard RWG discretizations typically result in poorly conditioned systems with a poor convergence; an example of this is shown in Figs. 2.4

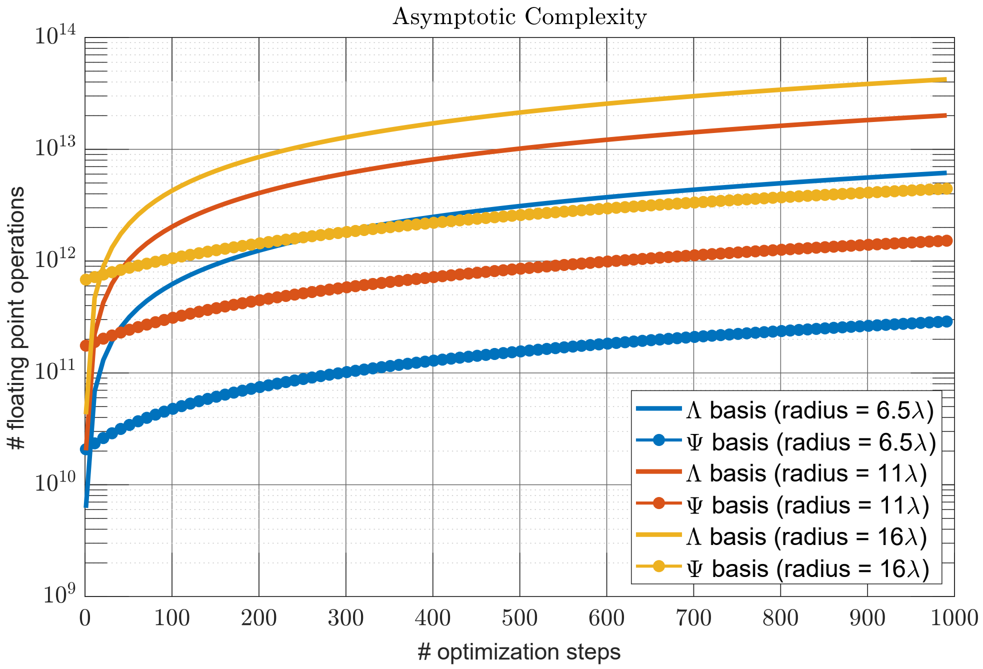

Figure 2.3: Estimate of floating point operations as a function of the number of optimization iteration for different problem sizes. We assume a permittivity of $\varepsilon_r = 6.15$ and a number of modes to follow a $\lambda_0/3$ spatial frequency variation along $\hat{\boldsymbol{\rho}}$.

and 2.5, both referring to a grounded dielectric substrate with central vertical probe excitation (see sect. 2.7) and $\varepsilon_r = 10.8$ with a PEC disc (i.e. $\underline{\underline{Z}}^s = 0$) with a radius of $3\lambda_0$. Here and in the following we indicate by λ_r the wavelength in the dielectric substrate at the operation frequency, i.e. $\lambda_r = \lambda_0/\sqrt{\varepsilon_r}$, where ε_r is the relative permittivity of the substrate. The iterative solver used belongs to the Krylov subspace methods and is indeed the generalized minimal residual method (GMRES). Three different extensions are considered as follows: (a) combined with a preconditioning method, (b) with a restart parameter r, and (c) in its flexible version. For more details about Krylov subspace methods the reader is referred to [37].

The RWG basis functions, as all sub-sectional bases, are well known to yield a matrix conditioning that worsens with mesh increasing density. Thus, with the aim of showing regularization, we consider both a very dense (Fig.2.5a) and a very coarse (Fig.2.5c) RWG discretization, with a mesh size $h \approx \lambda_r/3$, i.e. close to the Nyquist limit. For the case of a dense discretization, a mesh size $h \approx \lambda_r/15$ is taken. The induced current density for dense discretization is shown in Fig.2.5a and is taken as reference; the relative residue has a convergence path which follows the yellow line in Fig.2.4. Both for coarse and denses meshes, following the procedure in sect. 2.4 we retained 330 entire-domain CWG basis functions, obtaining a fast convergence rate (see blue line in Fig.2.4) and

Table 2.1: Summary of results obtained for a PEC disc on dielectric substrate, with central vertical probe excitation (see sect. 2.7) at $f = 17$ GHz and $\epsilon_r = 10.8$.

Fig. 2.5	Fig.2.4 line	Mesh Size	DoF	r-GMRES	κ	Num. of Iter.
(a)	purple	$\lambda_r/15$	7×10^4	7×10^4	-	1800
(b)	blue	$\lambda_0/10$	330	330	50	8
(c)	yellow	$\lambda_r/3$	7×10^3	250	2000	1800
(d)	red	$\lambda_r/3$	7×10^3	7×10^3	2000	1000

an accurate solution for both cases.

For the small problem, the system can be either solved directly or iteratively allowing for a convergence test, especially useful because the value of the residual is only a partial indication of the achieved accuracy. The RWG system has a condition number (in 2-norm) $\kappa_\Lambda \approx 2000$ which decreases to $\kappa_\Psi = 50$ after compression with the spectral CWG basis, exhibiting an evident conditioning effect. While, with this coarse mesh discretization, the condition number of the RWG system is relatively small ($\kappa_\Lambda = \mathcal{O}(N_\Lambda)$), convergence is slow, as seen in Fig.2.4; as expected and mentioned above, the compressed system instead converges very rapidly. We observe that this convergence rate, while not dramatic per se, is not acceptable in the perspective of a real-life structure with a radius above 10 wavelengths. In fact, analysis of the solution in Fig. 2.5d shows that with RWG after 1000 iterations the current is still significantly different from the reference one, as shown in Fig.2.5d; convergence to a more accurate solution is obtained with more than 1800 iterations. Obviously, this coarse discretization is not always sufficient for a stable solution; for example in Fig. 2.5c a restarted GMRES, with restart parameter $r = 250$, shows a solution affected by spurious oscillations, which is also the case when other techniques, such as incomplete LU (ILU) precoditioner and flexible GMRES [37], are used to improve the convergence path. Table 2.1 summarizes together the results showed in Fig. 2.4 and Fig. 2.5 and explained throughout sect. 2.5. The numerical results for real-life structures, including convergence analysis, are presented in sect. 2.7.

2.7 Convergence Analysis and Numerical Results

In this section we use holographic antennas, with isotropic and anisotropic surface impedance, to numerically illustrate and validate the use of div-conforming EBF based on WG modes to compress surface integral equations in MS simulations. Moreover, it is worth noting that in most of the analytic design procedures involving EBF, the modulated impedance and the basis functions are defined over a full circular domain, see

Fig. 2.6 for an example taken directly from [14]. This means that the induced current, expanded with EBF, is defined even on the region where the feed will eventually be positioned (yellow triangles in Fig. 2.6). Such a discretization of the IBC-EFIE leads to sub-optimal designs, especially when the cost function in the optimization procedure involves antenna matching as well.

There are various approaches to deal with this issue. Two of them are (a) to neglect the error introduced by the feeder at this stage of the design, and (b) to force the solution, obtained over the full domain, to be zero inside the feed region: this second alternative is chosen, for instance, by the authors of [19]. When circular EBF are used (i.e here the CWG or the Fourier-Bessel used in [19]), the problem of dealing with the feeder region always arises. The generality of the method and the results presented here, on the contrary, allows us to easily avoid the circular domain, defining annular domains and compress the system using the CXWG modes.

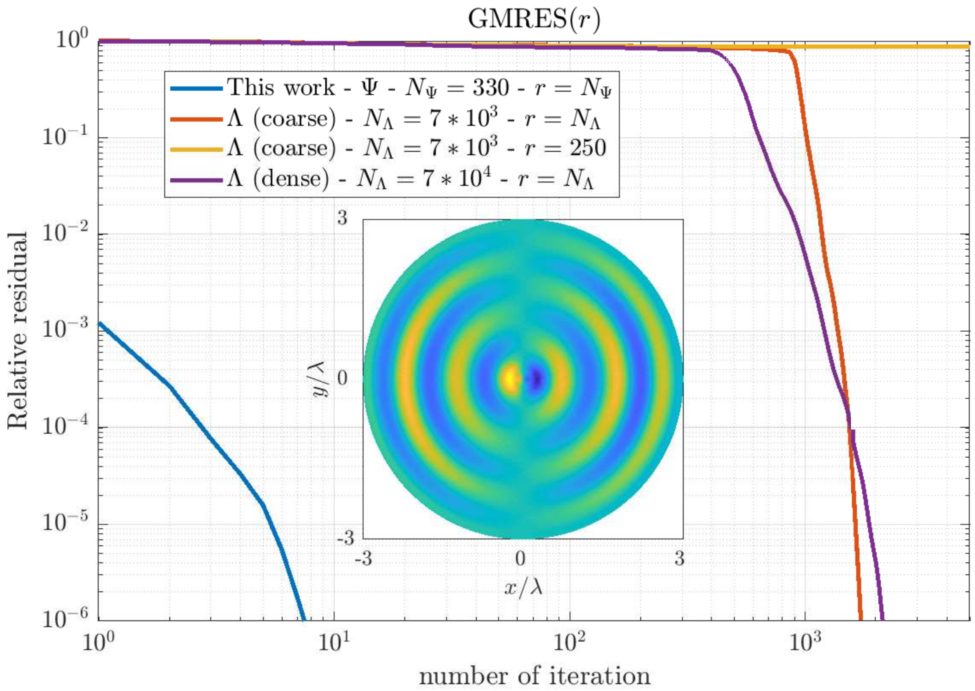

Figure 2.4: Convergence history of iterative solutions: relative residual of GMRES iterative solver. Blue line: convergence history with EBF spectral basis, GMRES with no restart (small number of unknowns). The other lines refer to RWGs, red and purple: GMRES with no restart, for coarse and dense discretization, respectively; yellow: restarted GMRES for the coarse mesh, with restart parameter r comparable to N_Ψ. Please note the log scale in the number of iterations. In the central box, the real part of the induced current obtained with a dense discretization, which is also taken as accuracy reference; a zoomed version is depicted in Fig.2.5a.

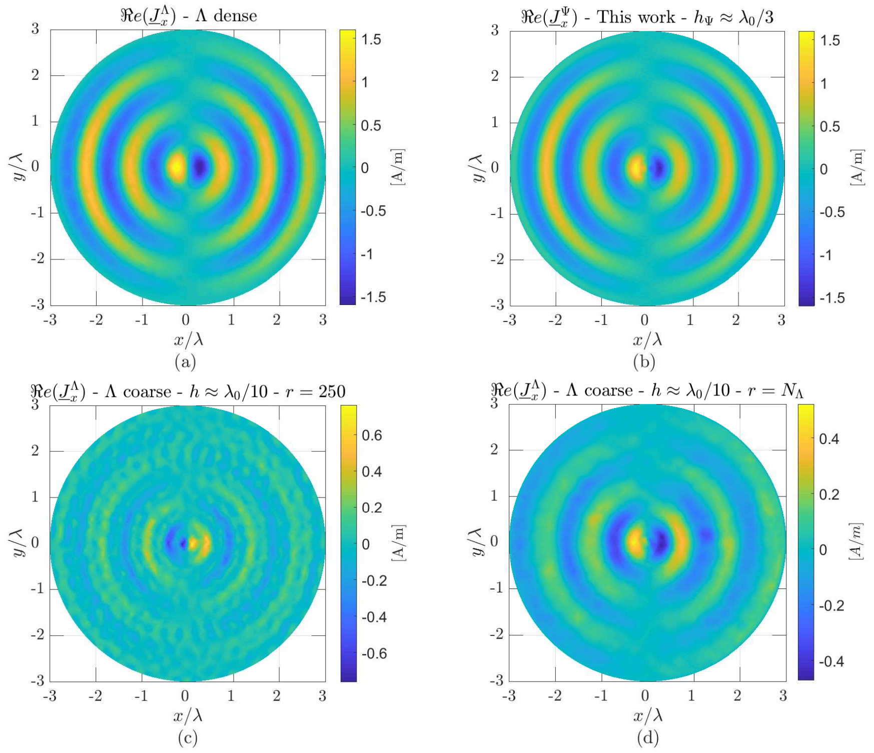

Figure 2.5: Real part of the induced current. (a) GMRES iterative solver solution with dense RWG discretization (purple line in Fig.2.4), (b) GMRES iterative solver solution of compressed system with 330 EBF (blue line in Fig.2.4), (c) GMRES iterative solver solution with a coarse discretization (the solution is obtained with a GMRES restart parameter $r = 250$, yellow line in Fig.2.4), (d) GMRES iterative solution with coarse discretization after 1000 iterations (red line in Fig.2.4).

In the following, the RWG (Λ, uncompressed) solution over an annular domain is taken as reference as the closest representation to the physical structure of the antenna. In this case, the solution is computed via GMRES with a Krylov space large enough to achieve the desired convergence performance. sect. 2.7.1 shows the controllability of the error on surface current and on the directivity for a design of interest, a MS antenna with scalar impedance. Finally, the analysis of a larger MS antenna with tensorial surface impedance is reported in sect. 2.7.2. Table 2.2 summarizes the geometrical data for both examples.

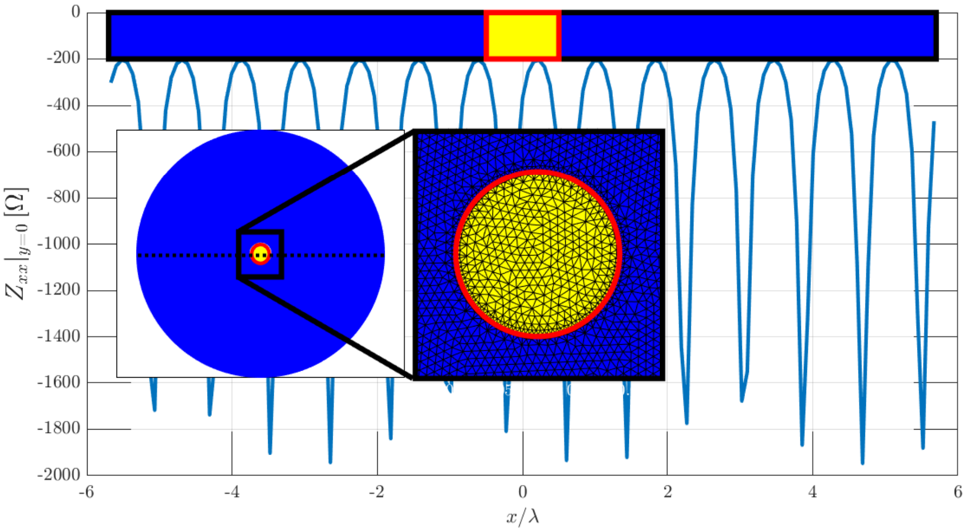

Figure 2.6: Analytic impedance profile (x-axis cut) used in the design of the scalar MS antenna presented in [14], see (2.15). On the bottom side a zoom of the feed region of the antenna when this region is included. When circular domain is used, the discretization of IBC-EFIE involves also the part related to the feed: yellow triangles).

Table 2.2: Summary of simulation parameters

	frequency	ε_r	radius	$\boldsymbol{h}$	$\boldsymbol{\mathcal{Z}}_s$
sect. 2.7.1	17 GHz	3.66	$5.7\lambda_0$	1.524 mm	scalar
sect. 2.7.2	15 GHz	6.15	$10\lambda_0$	1.016 mm	tensorial

2.7.1 Convergence Analysis

We use an antenna described in [14]. In that paper, a planar circularly polarized holographic MS antenna, with radius $5.7\lambda_0$, excited with a single-point feed at frequency $f = 17$ GHz, is presented. The grounded dielectric slab has thickness $h_d = 1.524$ mm and permittivity $\varepsilon_r = 3.66$. The *impenetrable* surface impedance in the scalar case is reduced to:

$$\boldsymbol{\mathcal{Z}}_s^+ = j \begin{bmatrix} X & 0 \\ 0 & X \end{bmatrix}, X = X_s \left[1 + M_0 \sin(\beta_{sw}\rho - \phi)\right], \tag{2.15}$$

which defines a spiral-shape reactance profile and the superscript '$+$' stands for impenetrable impedance. After removing the grounded slab's contribution according to [18], we obtain the *penetrable* (i.e. transparent) impedance profile needed for the IBC-EFIE. A vertical probe excites a cylindrical surface wave on the isotropic surface impedance, and the latter converts the excitation into a circularly polarized. The excitation in (2.3) has then a transverse component which is asymptotically

$$\boldsymbol{E}_t^{sw} \approx jX_0 H_1^{(2)}(\beta_{sw}^{GS}\rho)\hat{\boldsymbol{\rho}} \tag{2.16}$$

where $H_1^{(2)}$ is the Hankel function of the second kind and first order, and the reactance X_0 and the wavenumber β_{sw}^{GS} are derived solving the characteristic equation of the grounded dielectric slab of thickness h_d and permittivity ε_r.

To validate the method it is important to make sure that the compression maintains an adequate accuracy, both in the far-field and at surface current levels. We compare the solution obtained with RWG, i.e. solving (2.6), and the solution obtained with EBF, i.e. solving (2.11). As a figure of merit, we consider the L_2 distance between the computed currents, δ_J,

$$\delta_J = \left\| \boldsymbol{J}^{\Lambda} - \boldsymbol{J}^{\Psi} \right\|_{L^2} \tag{2.17}$$

In Fig. 2.7 we show the compression error (2.17) for the modulated scalar MS antenna presented in [14] as a function of the number of modes along $\hat{\boldsymbol{\phi}}$, M, for different values of the number of modes along $\hat{\boldsymbol{\rho}}$, N. The violet hexagram represents the minimal modal collection configuration ($M = 6, N = 30$) that keeps the compression error below 10^{-2}. The reference solution is calculated with a FFT-based fast-solver

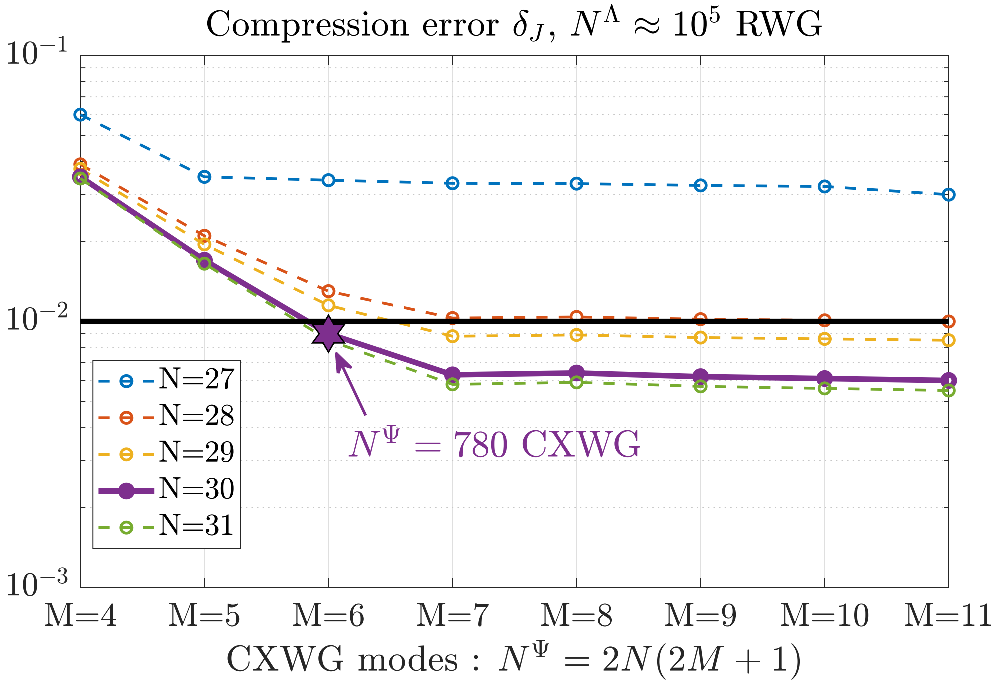

Figure 2.7: The plot shows the compression error δ_J as a function of M, number of modes along $\hat{\boldsymbol{\phi}}$, for different values of N, the minimum number of modes along $\hat{\boldsymbol{\rho}}$,. The violet hexagram represents the first modes configuration that keeps the compression error below 10^{-2}. The reference solution is obtained with approximately 10^5 RWG.

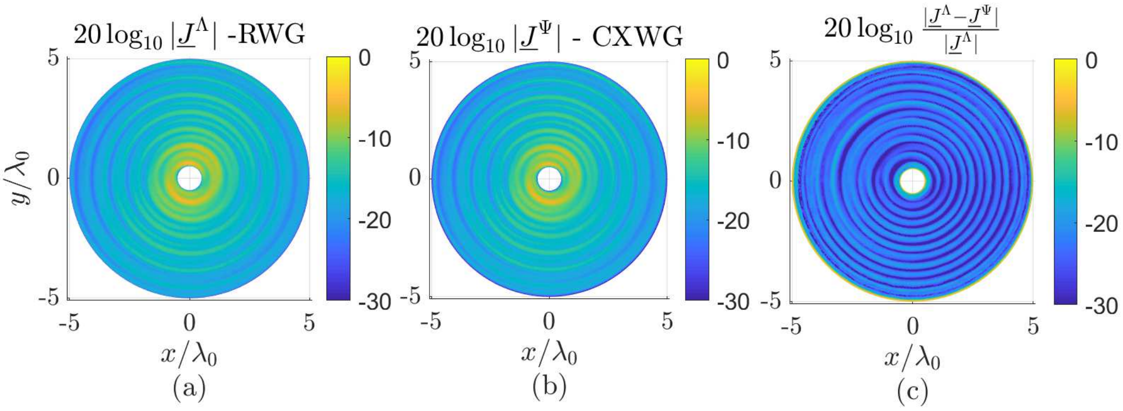

(a)

(b)

(c)

Figure 2.8: Magnitude of surface currents for an isotropic MS antenna similar to [14]: (a) full RWG system ($N_\Lambda = 129713$); (b) compressed system with $N_\Psi = 908$ CXWG modes ($N = 28$ and $M = 8$); (c) relative error between the current distributions (a) and (b).

using $N_\Lambda = 195253$. This plot can be used as a guide to determine the number of modes needed to achieve a desired accuracy.

A visual representation of the error for a fixed number of CXWG modes ($N_\Psi = 908$),

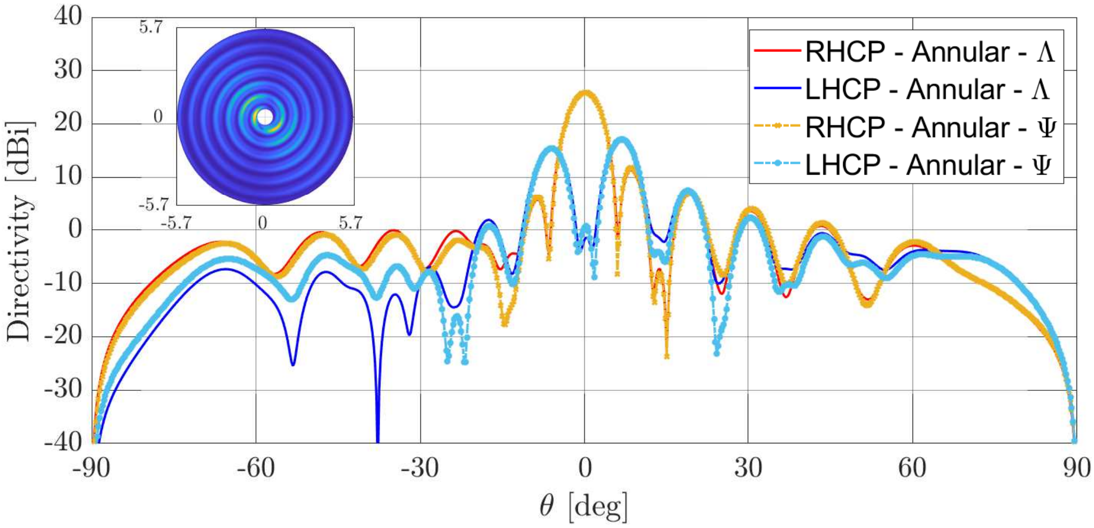

Figure 2.9: The directivity of isotropic MS antenna similar to [14]: left-hand circular polarization (LHCP) and right-hand circular polarization (RHCP) radiated by the antenna for $\theta \in [-90,90]$ and $\phi = 0$ simulated with $N_\Lambda = 195253$ RWG and with $N_\Psi = 908$ coaxial entire-domain basis functions.

is depicted in Fig. 2.8. The first two panels, (a) and (b), represent the magnitude of the surface currents calculated with RWG and CXWG basis functions, respectively, in log-scale, while the third panel (c) depicts the relative error. The relative error observed at the current level is $\delta_J < 10^{-2}$, which also corresponds to the maximum deviation shown in Fig.2.8c. The far-field filtering effect reduces this difference even more, as seen in the directivity plot of Fig. 2.9, where the two curves, both compressed and uncompressed cases, are almost identical. This validates the use of WG modes as EBFs able to provide figures of merit generally used in optimization routines (i.e directivity peak, side lobe level, axial ratio, etc.).

2.7.2 Modulated Tensorial Holographic Impedance

The polarization control is achieved through tensorial impedance [35]. Here, we consider a high-performance antenna with broadside beam and low cross-polarization. In this case, the IBC leads to the definition of a full surface impedance tensor which, in cylindrical coordinates, takes the following form:

$$\boldsymbol{\mathcal{Z}}_s = j\begin{bmatrix} X_{\rho\rho} & X_{\rho\phi} \\ X_{\phi\rho} & X_{\phi\phi} \end{bmatrix} \tag{2.18}$$

where each component of the tensor $\boldsymbol{\mathcal{Z}}_s$ is spatially modulated along $\hat{\rho}$ and $\hat{\phi}$ following a spiral-shape with radial modulation tapering $M(\rho)$ and $\bar{X}_0$ as in [12]:

$$\begin{aligned} X_{\rho\rho} &= \bar{X}_0\left[1 + M(\rho)\sin(\beta_{sw}\rho - \phi)\right] & (2.19)\\ X_{\rho\phi} = X_{\phi\rho} &= \bar{X}_0\left[M(\rho)\sin(\beta_{sw}\rho - \phi)\right] & (2.20)\\ X_{\phi\phi} &= \bar{X}_0\left[1 - M(\rho)\sin(\beta_{sw}\rho - \phi)\right]. & (2.21) \end{aligned}$$

The antenna is excited by a single-point feed at $f = 15$ GHz and has a radius of $10\lambda_0$. The grounded dielectric slab has thickness $h_d = 1.016$ mm and permittivity $\varepsilon_r = 6.15$. The domain is discretized with 450716 triangular facets, corresponding to $N_\Lambda \approx 674716$. In this case, the compressed solution is computed using CWG modes instead of CXWG modes, as done in Fig.2.9. The solution is obtained with $N_\Psi = 1098$ modes and is compared to the solution obtained with RWG functions in terms of directivity, see Fig.2.10. Table 2.3 summarizes the main quantities of interest to compare the proposed approach to the RWG case.

2.8 Conclusions

This chapter offers an efficient numerical approach for the optimization of large planar metasurfaces based on spatially modulated tensorial impedance. The full-wave method presented dramatically speeds up the optimization loop in the design process

Table 2.3: Summary of computational results obtained with Intel Xeon CPU E5-2687W v4 @3GHz.

Case of Sect.	basis function	DoF	Factorization $\underline{\underline{Z}}$	Compression $\underline{\underline{\Psi}}^T \underline{\underline{Z}}\,\underline{\underline{\Psi}}$	Solving time	GMRES steps
2.7.1	RWG	195253	48m	–	16m	186
	CXWG	908	48m	5h2m	$<$ 1s	12
2.7.2	RWG	674716	3h15m	–	50m	1658
	CWG	1098	3h15m	6h17m	$<$ 1s	51

when the surface impedance is considered as a homogenization type of approximation for electrically thin structures, i.e. transparent impedance boundary conditions.

We achieve this numerical efficiency starting by aggregating RWG functions into div-conforming entire-domain basis functions, and computing all matrix entries via fast factorization.

Especially in metasurface antennas based on leaky-wave radiation, due to the presence of the grounded slab, the geometrical discretization of the IBC-EFIE is extremely sensitive to the dielectric properties. Thus, to guarantee a stable solution in a conventional way, a very large number of RWG basis functions are needed and a very large Krylov subspace is required to reach convergence. In this paper, we discuss how to

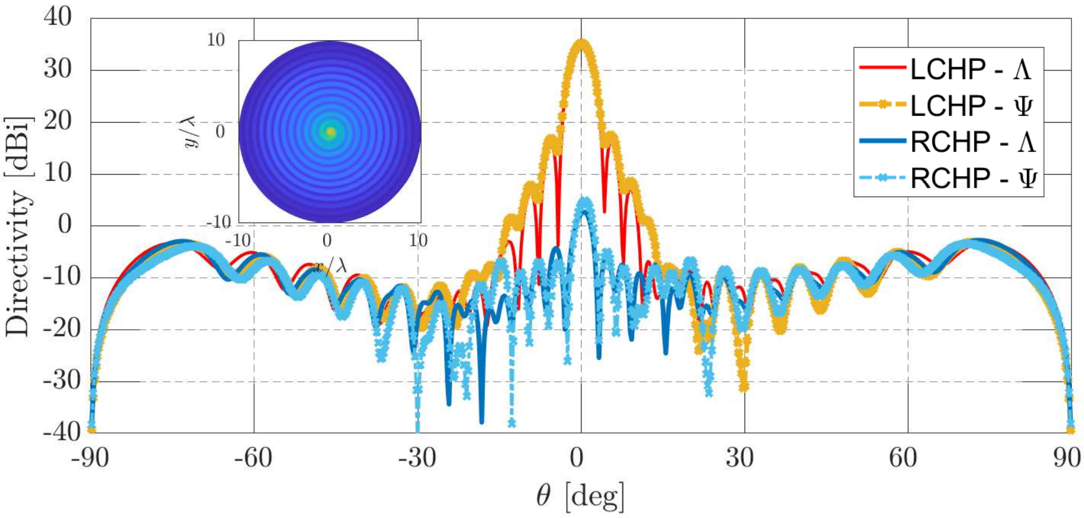

Figure 2.10: Directivity for an anisotropic MS antenna: LHCP and RHCP radiated by the antenna for $\theta \in [-90{,}90]$ and $\phi = 0$ simulated with $N_\Lambda \approx 7 \times 10^5$ RWG and $N_\Psi \approx 10^3$ CWG.

use div-conforming entire-domain basis functions to compress and regularize the system matrix, keeping the solution accuracy controllable with a limited number of degrees of freedom. We show the flexibility of the method by modeling the antenna in an annular domain, avoiding ambiguous interpretation of an impedance defined over the feeding region. Eventually, the problem is well-suited for antenna synthesis, pattern optimization problems. For structures with radius of $10\lambda_0$, the method allows a reduction in the number of operations that must be performed by a factor 10. Results which show benefit in terms of computational cost have been presented. The use of the div-conforming entire-domain basis functions in actual optimization endeavours is the subject of the next chapter. The feed region modeling options are the subject of the last chapter.

Chapter 3

Numerical Synthesis of Metasurface Antennas with Arbitrary Pattern Mask using Entire Domain Basis Functions

The real power of the impedance boundary condition (IBC) description is in the design of MS components. Designing the antenna via the spatial profile of the IBC allows one to break the design task in two: 1) design of the individual unit cells that locally yield the desired value of the surface impedance; 2) design of the IBC distribution. The first task is usually done in the approximation of local periodicity; in the typical procedure, one chooses a given unit-cell geometry, described by a few parameters (e.g. a tilted ellipse) and maps the value of achieved impedance over these; design of the unit cells is then achieved with lookup tables or more sophisticated mappings. This task is not of central interest in this chapter; the only information needed is the synthesizable range of reactance of an arbitrary unit cell, which for canonical geometries can be analytically estimated a priori. The latter and second task is of primary interest here. We approach the design of the spatial IBC distribution as an optimization process. The use of full-wave simulation in this optimization cycle is made possible by aggregating the underlying RWG functions into entire-domain basis functions (EBF), in the form of waveguide modes. It is shown in the previous chapter that this is advantageous in terms of the total numerical resources required in the optimization process. The numerical synthesis of annular and rectangular metasurface antennas — with broadside and tilted beam radiation pattern masks — confirms the applicability of the method proposed.

3.1 Introduction and Motivations

In this chapter we show the automatic design of metasurface (MS) antennas based on leaky-wave (LW) radiation via numerical synthesis of a modulated tensorial sheet impedance, namely $\boldsymbol{\mathcal{Z}}_s$. As known in literature and also seen in chapter 2, MS antennas radiation is well described in terms of a continuous slowly varying electric sheet tensorial reactance interacting with a surface-wave (SW) which is gradually transformed into a leaky-wave (LW) structure [14]. Thus, in a simplified "approximated" model of the antenna, designing a purely imaginary $\boldsymbol{\mathcal{Z}}_s$ profile means designing an antenna which radiates the prescribed pattern.

Numerical simulation of large MS antennas have shown stable discretization and accurate results if the MS is modeled with "transparent" impedance boundary conditions (IBC) and the electric field integral equation (EFIE) in a layered media environment [18]. The use of the *transparent* rather the *opaque* boundary conditions intrinsically accounts for space dispersion of the surrounding background (i.e., a grounded slab in practical implementations) [18]. The resulting method of moment (MoM) system is the same as derived in Chap.2 and is reported here as follows:

$$\left(\underline{\underline{Z}} - \underline{\underline{Z}}_s\right) \underline{J}^{\Lambda} = \underline{b}^{\Lambda}, \tag{3.1}$$

where $\underline{\underline{Z}}$ is the MoM matrix resulting from the discretization of the layered media electric field integral operator with canonical Rao-Wilton-Glisson (RWG) basis functions. The matrix $\underline{\underline{Z}}_s$ is the Galerkin test of the RWG representation of the tensorial sheet impedance $\boldsymbol{\mathcal{Z}}_s$. The vector $\underline{J}$ collects the unknown coefficients of the equivalent currents $\boldsymbol{J}$ of the IBC-EFIE and $\underline{b}^{\Lambda}$ is the right-hand-side. The state-of-art analysis and design mainly is associated with the asymptotic expression of the planar surface wave, as shown in [3], and reported in Eq. (2.16). It is worth noting that this option does not give direct information on feeder design parameters, such as return loss (RL). Indeed, right-hand-side modeling options are discussed for the first time in detail (for this particular class of antennas) in Chap. 4 and improved discussed solutions can be effortless integrated in the scheme proposed here. In fact, feeder related figures of merits will be available using the fast-factorization of the IBC-EFIE using div-conforming annular entire-domain basis functions (EBFs), together with a more accurate model of the of the feed region (based on a realistic 3D geometry).

It has been shown in Chap. 2 that the use of EBF compresses and regularizes the system of Eq. (3.1). This allows reduction of the numerical burden associated with the whole optimization cycle, where every step requires the numerical solution for each intermediate profile until the radiated field satisfies the prescribed constraints. The EBF MoM system reads:

$$\left(\underline{\underline{\Psi}}^{T} \underline{\underline{Z}}\,\underline{\underline{\Psi}} - \underline{\underline{Z}}_s^{\Psi}\right) \underline{J}^{\Psi} = \underline{\underline{\Psi}}^{T} \underline{b}^{\Lambda} \tag{3.2}$$

where $\underline{\underline{\Psi}}$ represents the basis change matrix from RWG to EBF defined in subsection 2.3.3. However, finding an optimal $\boldsymbol{\mathcal{Z}}_s$ for a specific radiation pattern mask requires the solution of a strongly non-linear, non-convex problem [25].

In Sect. 3.2 we declare the global optimization instances, including the definition of the cost function used. Moreover, it is explained how to reduce the overall computational time of the optimization loop, for large structures, from days to hours. In order of appearance, we show the additional cost due to the far-field pattern radiation of the compressed solution, and the impedance (IBC) update into the optimization loop. Section 3.3 shows numerical results for the optimization of a pencil-beam MS antennas based on leaky-wave radiation with both annular and rectangular domains. Results confirm the flexibility of the method proposed and a great improvement in speed of computation of the antenna parameters related to the cost function.

3.2 Optimization Instances

In the table 3.1, we show the pseudocode of a design algorithm; optimization algorithms vary significantly, especially in the update method (step 12 of Tab. 3.1). The common trait is the necessity to evaluate a cost function F at each step; hence, ability to evaluate this cost function quickly is an enabling factor. In our case, this cost function will have to involve solution of the IBC equation (3.1) and the computation of the radiated field. We observe (as already mentioned in Chap.2) that an initial overhead may well be tolerable if the cost per iteration and the number of iterations justify it in terms of total time of the optimization process. Entire-domain basis functions are a good candidate in this sense, while requiring special handling of various parts of the above-sketched computations; this will be the subject of Sect. 3.2.2. The second observation is that the typical design problem we want to address is not amenable to convex

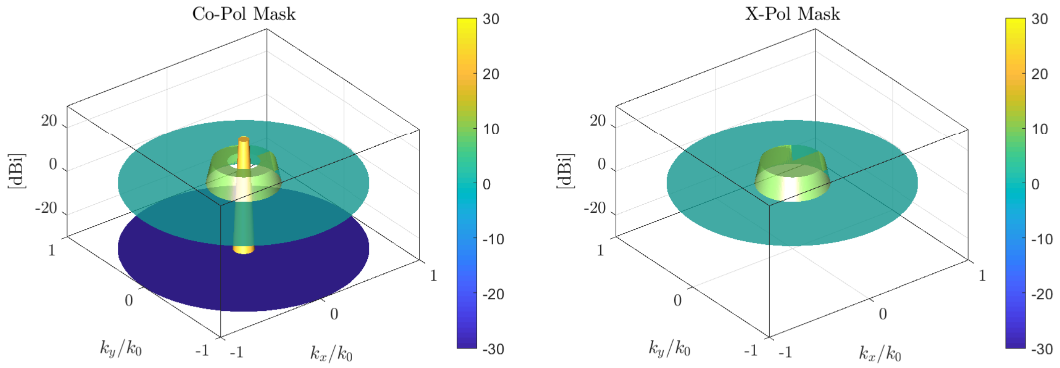

(a) (b)

Figure 3.1: Pattern masks for broadside pencil beam radiation used in the broadside design of Sect. 3.3.1. The colorbar indicates the levels to which each mask is set. Left: the co-pol (a) upper (greenish) and lower mask (blue and yellow). Right: the x-pol upper mask.

optimization, thus requiring global optimization approaches. A general property of all these methods is that eventually the number of iterations is exponential with respect to the no. of optimization parameters. Hence, it is crucial to keep the no. of design parameters small. This will be dealt with ad-hoc parametrization of the impedances for the two design examples of Sect. 3.3. To emphasize the dependency of $\underline{\underline{Z}}^s$ on N_{design} design parameters, we collect the N_{design} parameters in the array p and write $\underline{\underline{Z}}^s(p)$.

3.2.1 Cost Function for Pattern Synthesis

The general, and most practical way of describing the specifications on the desired radiation pattern is through amplitude masks, namely a lower and an upper bound on the amplitude for each direction. Figure 3.1 shows an example of a lower and upper masks.

Accordingly, we define our cost function to be optimized in terms of satisfaction of the requisite masks. The upper and lower masks (inequalites) define the set of radiated fields that comply with the specifications. Our cost function will then measure the distance from this set, which we call the compliance set. A practical way of doing so is "projecting" a given candidate pattern onto the compliance set (as indicated below), and then measuring the norm (L2) of the difference from the pattern and its projection.

Table 3.1: Pseudocode of the design algorithm

```
procedure SURFACE IMPEDANCE DESIGN INSTANCE: ($\boldsymbol{\mathcal{Z}_s}(p)$)
    $\underline{\underline{Z}}^s \leftarrow \boldsymbol{\mathcal{Z}_s}(p)$
    Compute $\underline{\underline{\Psi}}$
    Solve (3.1) : $\left(\underline{\underline{Z}} - \underline{\underline{Z}}^s\right)\underline{J} = \underline{b}^{\Lambda}$
    Compute and store $\underline{\underline{\Psi}}^T \underline{\underline{Z}}\,\underline{\underline{\Psi}}$
    $\underline{J}^{\Psi} \leftarrow$ Solve (3.2)
    Compute $\mathcal{F}(\underline{J}^{\Psi})$
    Evaluate cost function $F$
    Initialize iteration counter $N$
    while Stopping criteria are not satisfied do
        $N \leftarrow N + 1$
        Update $\underline{\underline{Z}}^s(p) \leftarrow \boldsymbol{\mathcal{Z}_s}(p)$
        $\underline{J}^{\Psi} \leftarrow$ Solve (3.2)
        Compute Radiation Pattern $\mathcal{F}(\underline{J}^{\Psi})$
        Evaluate cost function $F$
    end while
    Compute $\underline{J}^* = \underline{\underline{\Psi}}^T \underline{J}^{\Psi}$ and $\mathcal{F}(\underline{J}^*)$
    return
end procedure
```

In a narrative form, the projection is achieved by a) clipping the pattern that goes above or below the masks, and substituting it for the appropriate mask value; and b) leaving the pattern unchanged wherever it falls within the masks (i.e. compliance region).

We can formalize the above as follows. Denote with $\ell(\theta,\phi)$ and $u(\theta,\phi)$ the lower and upper bounds on the amplitude, as a function of the spherical coordinates θ and ϕ. Given a pattern $\mathcal{F}(\theta,\phi)$, the projection of $\mathcal{F}$ on the compliance set is $\tilde{\mathcal{F}}$ such that

$$|\tilde{\mathcal{F}}(\theta,\phi)| = C \min\left(\max\left(\left|\mathcal{F}(\theta,\phi)\right|/C, \ell(\theta,\phi), u(\theta,\phi)\right)\right), \tag{3.3}$$

with

$$C = \max_{\theta,\phi} |\mathcal{F}(\theta,\phi)| \tag{3.4}$$

The effect of the projection described in the Eq. (3.3) is depicted in Fig. 3.2. Thus, the norm of the difference between the pattern $\mathcal{F}$ and its clipped projection $\tilde{\mathcal{F}}$, is our cost function F,

$$F = \left\| \mathcal{F}(\theta,\phi) - \tilde{\mathcal{F}}(\theta,\phi) \right\| \tag{3.5}$$

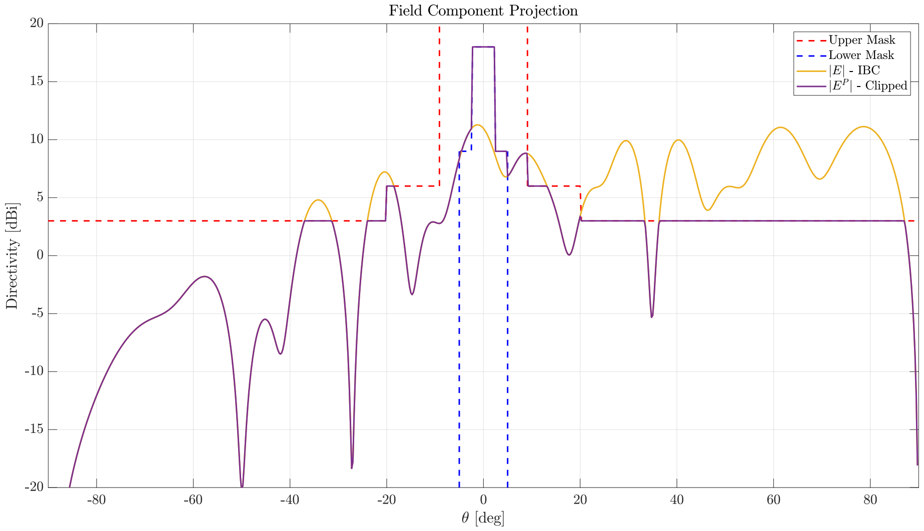

Figure 3.2: The red and the blue dotted lines are upper and lower pattern masks u and ℓ at $\phi = 0$, respectively. The yellow line is a random (w.r.t. the design parameters array p) representation of a generic field component at a given point of the IBC optimization, $\mathcal{F}$ (see Tab. 3.1, line 14). The violet line is $\tilde{\mathcal{F}}$, the projection of $\mathcal{F}$ within the masks u and ℓ. See Eq. (3.3) for more details.

3.2.2 Reduced Computational Cost in the Optimization Loop

In this subsection, the emphasis is given to two aspects of the pseudocode shown in table 3.1. The first one concerns the far-field pattern radiation of the compressed solution (i.e. line 14 of the optimization loop in table 3.1). The second is the update of the IBC matrix, namely $\underline{\underline{Z}}^s(p)$, for different instances of the design array p (i.e. line 12 of the optimization loop in table 3.1). Both efficient pattern computation and IBC matrix updates are of crucial importance in optimization endeavors of large structures. Compared to rectangular and circular domains, where closed-form integration is possible, annular EBF are more engaging and need special care. It is worth noting that the importance of this section is mainly due to the use of annular domains in most of the applications of interest. The 3D radiation pattern-matrix is computed in a semi-closed form and stored before starting the optimization routine. In both cases, the integrals to be evaluated have a negligible time cost due to a numerical integration along the radial component only. The rule-of-thumb used to determine the number of points is approximately 15 per wavelength. Thus, the compression effect of the EBF, explained in Sect. 2.5 comes again to help, allowing, among other benefits, the storage of the 3D pattern-matrix. Therefore, radiation pattern updates will be instantly available at each step of the optimization loop. The compressed IBC part of the resulting MoM matrix, i.e. $\underline{\underline{Z}}_s^{\Psi}$ of Eq. (3.2), is computed on-the-fly; however it results in a negligible update cost. Numerical results of the next Sect. 3.3.1 for annular EBF confirm the applicability of the proposed method.

The more parameters to be optimized (i.e. tensorial impedance with no parametrization available), the more optimization steps are needed. The larger the antenna and the more complex the impedance profile; the more EBFs we need to properly factorize the MoM system. The asymptotic complexity of this method tells us that optimization is possible for even large and complex MS antennas. The efficient computation of the pattern generated by the annular-ring div-conforming EBF reduces the overall cost of pattern computation by a factor of 100 after 1000 optimization steps. Consistent advantages are also obtained after only a few optimization steps (e.g. 20 as in the application example).

Efficient Computation of Annular EBF Radiation in LM: Derivations

For stationary phase points, i.e.

$$\mathbf{k}_\rho^s = k_N \sin\vartheta\,(\cos\varphi\,\hat{\boldsymbol{x}} + \sin\varphi\,\hat{\boldsymbol{y}}) \tag{3.6}$$

$$k_{zN}^s = k_N \cos\vartheta \tag{3.7}$$

we can write from equation (162) of [31] the far-field radiation integrals as follows

$$E_{\vartheta,\varphi} \approx \frac{e^{-jk_N r}}{2\pi j r} e^{-jk_{zN}^s z_0} k_N \underbrace{\langle \boldsymbol{f}_{\vartheta,\varphi} e^{j\mathbf{k}_\rho^s\cdot\boldsymbol{\rho}'}; \boldsymbol{J}\rangle}_{\mathcal{F}_{\vartheta,\varphi}^J} \tag{3.8}$$

where, for planar components only,

$$\boldsymbol{f}_{\vartheta}^{EJ} = V_i^e(z_0|z')\hat{\boldsymbol{\rho}} \tag{3.9}$$

$$\boldsymbol{f}_{\varphi}^{EJ} = \cos\vartheta V_i^h(z_0|z')\hat{\boldsymbol{\phi}}. \tag{3.10}$$

It is worth noting that at the stationary phase point $\hat{\boldsymbol{u}} = \hat{\boldsymbol{\rho}}$ and $\hat{\boldsymbol{\phi}} = \hat{\boldsymbol{v}}$, where the directions of the unit vectors $\hat{\boldsymbol{u}}$ and $\hat{\boldsymbol{v}} = \hat{\boldsymbol{z}} \times \hat{\boldsymbol{\rho}}$ are fixed by the observation angle φ. The EBF compressed solution, namely $\boldsymbol{J}^{\Psi}$, can be written as linear combination of RWGs as in Eq. (2.12) or directly in term of coaxial waveguide modes, $\mathbf{h}$. As discussed before, to compute at each optimization step the far-field in terms of N_Λ can be extremely expensive. That is why we need to compute the radiation of the corresponding waveguide modes. For rectangular and circular domains, this can be done in a closed form, as reported in Appendix D.1 for the rectangular domain. To the best of the author knowledge, the annular EBF have closed-form expressions for $\hat{\boldsymbol{\phi}}$ components only. The results of this derivation are reported in this section with supplementary materials in Appendix C. Thus, the $\hat{\boldsymbol{\rho}}$ component of each mode has to be integrated numerically.

Here we derive the semi-closed form expression for the generic mode $\mathbf{h}_\ell$. Without loss of generality, for the derivation we refer to $\mathbf{h}_\ell$ as a specific compressed solution $\boldsymbol{J}^{\Psi}$ of Eq. (3.2) with all unitary coefficients. Moreover, the subscript ℓ is dropped for the ease of the reader. It follows that

$$\begin{aligned}
\boldsymbol{J}^{\Psi} &= J_\rho(\rho',\phi')\hat{\boldsymbol{u}} + J_\phi(\rho',\phi')\hat{\boldsymbol{v}} \\
&= \left[g(\rho')h(\phi')\cos(\phi'-\varphi) - l(\rho')m(\phi')\sin(\phi'-\varphi)\right]\hat{\boldsymbol{\rho}} + \\
&\quad \left[g(\rho')h(\phi')\sin(\phi'-\varphi) + l(\rho')m(\phi')\cos(\phi'-\varphi)\right]\hat{\boldsymbol{\phi}},
\end{aligned}$$

where $g(\rho')$ and $l(\rho')$ are the Bessel's functions defined in table B.1, and

$$h(\phi') = \begin{cases} \cos m\phi', \text{even symmetry} \\ \sin m\phi', \text{odd symmetry} \end{cases}, \quad m(\phi') = \begin{cases} \sin m\phi', \text{even symmetry} \\ \cos m\phi', \text{odd symmetry} \end{cases}.$$

Thus, $\mathcal{F}_{\vartheta,\varphi}^{J^{\Psi}}$ of (3.8) are derived using (3.9) and (3.10), respectively. It follows that

$$\begin{aligned}
\mathcal{F}_{\vartheta}^{J^{\Psi}} &= \langle \boldsymbol{f}_{\vartheta} e^{j\mathbf{k}_\rho^s\cdot\boldsymbol{\rho}'}; \boldsymbol{J}^{\Psi}\rangle \\
&= V_i^e(z_0|z')\int_b^a\int_{-\pi}^{\pi} e^{j\mathbf{k}_\rho^s\cdot\boldsymbol{\rho}'}\hat{\boldsymbol{\rho}}\cdot J_\rho(\rho',\phi')\hat{\boldsymbol{u}}\rho' d\rho' d\phi' \\
&= V_i^e(z_0|z')\int_b^a d\rho'\rho' g(\rho')\underbrace{\int_{-\pi}^{\pi} d\phi' h(\phi')\cos(\phi'-\varphi)\, e^{j\mathbf{k}_\rho^s\cdot\boldsymbol{\rho}'}}_{\mathcal{I}_1} \\
&\quad -V_i^e(z_0|z')\int_b^a d\rho'\rho' l(\rho')\underbrace{\int_{-\pi}^{\pi} d\phi' m(\phi')\sin(\phi'-\varphi)\, e^{j\mathbf{k}_\rho^s\cdot\boldsymbol{\rho}'}}_{\mathcal{I}_2}
\end{aligned} \tag{3.11}$$

and

$$\begin{aligned}
\mathcal{F}_{\varphi}^{J^{\Psi}} &= \langle \boldsymbol{f}_{\varphi} e^{j\mathbf{k}_{\rho}^{s}\cdot\boldsymbol{\rho}'}; \boldsymbol{J}^{\Psi}\rangle \\
&= V_i^h(z_0|z')\cos\vartheta \int_b^a \int_{-\pi}^{\pi} e^{j\mathbf{k}_{\rho}^{s}\cdot\boldsymbol{\rho}'}\hat{\boldsymbol{\phi}}\cdot\boldsymbol{J}^{\Psi}\rho' d\rho' d\phi' \\
&= V_i^h(z_0|z')\cos\vartheta \int_b^a d\rho'\rho' g(\rho') \underbrace{\int_{-\pi}^{\pi} d\phi' h(\phi')\sin\left(\phi'-\varphi\right) e^{j\mathbf{k}_{\rho}^{s}\cdot\boldsymbol{\rho}'}}_{\mathcal{I}_2} \\
&\quad + V_i^h(z_0|z')\cos\vartheta \int_b^a d\rho'\rho' l(\rho') \underbrace{\int_{-\pi}^{\pi} d\phi' m(\phi')\cos\left(\phi'-\varphi\right) e^{j\mathbf{k}_{\rho}^{s}\cdot\boldsymbol{\rho}'}}_{\mathcal{I}_1} \qquad (3.12)
\end{aligned}$$

where

$$\mathbf{k}_{\rho}^{s}\cdot\boldsymbol{\rho}' = k\rho'\sin\vartheta\cos\left(\phi'-\varphi\right).$$

Summarizing

$$\mathcal{F}_{\vartheta}^{J} = V_i^e(z_0|z') \int_b^a d\rho'\rho' \begin{cases} g(\rho')\mathcal{I}_1^{\cos}, \text{ even symmetry} \\ -l(\rho')\mathcal{I}_1^{\sin}, \text{ odd symmetry} \end{cases} \qquad (3.13)$$

$$\mathcal{F}_{\varphi}^{J} = \cos\vartheta V_i^h(z_0|z') \int_b^a d\rho'\rho' \begin{cases} g(\rho')\mathcal{I}_2^{\cos}, \text{ even symmetry} \\ l(\rho')\mathcal{I}_2^{\sin}, \text{ odd symmetry} \end{cases} \qquad (3.14)$$

where $\mathcal{I}_1^{\cos}, \mathcal{I}_1^{\sin}, \mathcal{I}_2^{\cos}, \mathcal{I}_2^{\sin}$ are the closed-form ϕ integration calculated in detail in Appendix C.

To check the accuracy of the described method we compare three different ways of computing the radiating fields. The RWG and EBF solution considered is the one found for the MS antenna described in Sect. 2.7.1. The ground truth is considered to be the RWG radiation of the RWG solution, namely $\boldsymbol{J}^{\Lambda}$ in Chap.2. Then we compare the ground truth to the radiation of $\boldsymbol{J}^{\Psi}$ written both as linear combinations of RWG and of EBF (i.e. the method associated to the above derivation). In Fig. 3.3 we show the three different computations of the E-field at the cut $\varphi = 0$ and $\vartheta \in [0, 90]$. Overall, there is a certain degree of approximation in each adopted method. On the one hand, the comparison of the RWG radiation of $\boldsymbol{J}^{\Lambda}$ with the RWG radiation of $\boldsymbol{J}^{\Psi}$ gives us a better understanding of the level of approximation in far-field of the EBF factorization. On the other hand, the comparison between RWG and EBF radiation of $\boldsymbol{J}^{\Psi}$ only, gives us the quality of the projection of the WG modes into the RWGs. A poor agreement between the last two means a poor quality RWG mesh. This topic is briefly addressed in the subsection 2.3.3. Nevertheless, for the case of interest, we observe a good level of agreement among all the curves of Fig. 3.3. Eventually, we conclude that the use of the EBF radiation is the best choice in optimization endeavors.

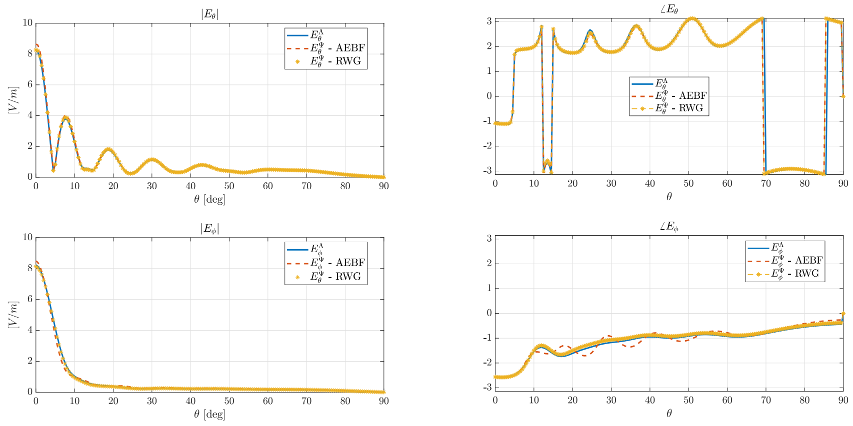

(a) E-field magnitude.

(b) E-field phase.

Figure 3.3: Comparison between three different ways of computing the radiating fields along the cut $\varphi = 0$ and $\vartheta \in [0, 90]$. The plots on the top are for the ϑ component. The plots on the bottom are for the φ component. The blue lines stand for RWG radiation of RWG (Λ) solution. The dotted red lines represent the EBF radiation of EBF (Ψ) solution. The yellow markers are the RWG radiation of the projected EBF solution.

Compressed IBC-MoM Matrix Entries

The issue discussed above — the lack of closed-form expression for annular EBF far-field radiation — also holds for the computation in a closed-form of the IBC matrix entries. Let us consider the ℓ-th annular EBF:

$$\begin{aligned}\mathbf{h}_\ell &= f_\ell^\rho(\rho) g_\ell^\rho(\phi)\hat{\boldsymbol{\rho}} + f_\ell^\phi(\rho) g_\ell^\phi(\phi)\hat{\boldsymbol{\phi}} \\ &= f_\ell^\rho(\rho)\begin{cases}\cos(\ell\phi) \\ \sin(\ell\phi)\end{cases}\hat{\boldsymbol{\rho}} + f_\ell^\phi(\rho)\begin{cases}\sin(\ell\phi) \\ \cos(\ell\phi)\end{cases}\hat{\boldsymbol{\phi}}. \end{aligned} \tag{3.15}$$

We will limit our investigation here to particular impedance profile of interest. The first assumption is that the transparent reactance is lossless, which produces an anti-hermitian tensor as follows:

$$\mathcal{Z}_s = j\mathcal{X} = j\eta_0\left[X_{\rho\rho}(\rho,\phi)\hat{\boldsymbol{\rho}}\hat{\boldsymbol{\rho}} + X_{\rho\phi}(\rho,\phi)(\hat{\boldsymbol{\rho}}\hat{\boldsymbol{\phi}} + \hat{\boldsymbol{\phi}}\hat{\boldsymbol{\rho}}) + X_{\phi\phi}(\rho,\phi)\hat{\boldsymbol{\phi}}\hat{\boldsymbol{\phi}}\right]$$

Thus, the ℓm matrix entry of (2.11) relative to the IBC part and expressed only in terms of annular EBF is

$$\langle \mathbf{h}_\ell; \mathcal{X}\cdot\mathbf{h}_m\rangle = \int_\Sigma \mathbf{h}_\ell(\rho,\phi)\cdot\left[\mathcal{Z}_s(\rho,\phi)\cdot\mathbf{h}_m(\rho,\phi)\right]\rho\,d\rho\,d\phi \tag{3.16}$$

where $\mathbf{h}_{\ell,m}$ are real vector-valued functions and Σ is their geometrical support, which corresponds to the entire antenna domain. The second assumption is that each component of the tensor can be written as follows:

$$X_{\rho\rho} = x^{\rho\rho} + \sum_{k=1}^{K} x_k^{\rho\rho} f_k(\rho)\cos(k\phi) + \sum_{k=1}^{K} x_{k+K}^{\rho\rho} f_k(\rho)\sin(k\phi) \tag{3.17}$$

$$X_{\rho\phi} = \sum_{k=1}^{K} x_k^{\rho\phi} f_k(\rho)\cos(k\phi) + \sum_{k=1}^{K} x_k^{\rho\phi} f_{k+K}(\rho)\sin(k\phi) \tag{3.18}$$

$$X_{\phi\phi} = x^{\phi\phi} + \sum_{k=1}^{K} x_k^{\phi\phi} f_k(\rho)\cos(k\phi) + \sum_{k=1}^{K} x_k^{\phi\phi} f_{k+K}(\rho)\sin(k\phi) \tag{3.19}$$

where $x^{\rho\rho}, x^{\phi\phi}$ are the average reactances, K is the number of modes needed to represent each component of the impedance. Without loss of generality, we arbitrarily assumed K equal for all components of the impedance to avoid heavy notation. Thus,

$$\mathcal{X}\cdot\mathbf{h}_m = \left(X_{\rho\rho}+X_{\rho\phi}\right) f_m^{\rho}(\rho) g_m^{\rho}(\phi)\hat{\boldsymbol{\rho}} + \left(X_{\phi\phi}+X_{\rho\phi}\right) f_m^{\phi}(\rho) g_m^{\phi}(\phi)\hat{\boldsymbol{\phi}} \tag{3.20}$$

Substituting (3.20) and (3.15) into (3.16) we obtain:

$$\begin{aligned}
\langle \mathbf{h}_\ell; \mathcal{X}\cdot\mathbf{h}_m\rangle \;=\; & \int_b^a \int_{-\pi}^{\pi} f_\ell^{\rho}(\rho) g_\ell^{\rho}(\phi)(x^{\rho\rho}+x^{\phi\phi}) f_m^{\rho}(\rho) g_m^{\rho}(\phi)\rho\, d\rho\, d\phi \\
& + \sum_{k=1}^{K}\left(x_k^{\rho\rho}+x_k^{\rho\phi}\right)\int_b^a f_\ell^{\rho}(\rho) f_k(\rho) f_m^{\rho}(\rho)\rho\, d\rho \underbrace{\int_{-\pi}^{\pi} g_\ell^{\rho}(\phi) g_m^{\rho}(\phi)\cos(k\phi)\, d\phi}_{\mathcal{I}^{\rho}_{\cos}=\mathcal{I}_1,\mathcal{I}_4} \\
& + \sum_{k=1}^{K}\left(x_{k+K}^{\rho\rho}+x_{k+K}^{\rho\phi}\right)\int_b^a f_\ell^{\rho}(\rho) f_k(\rho) f_m^{\rho}(\rho)\rho\, d\rho \underbrace{\int_{-\pi}^{\pi} g_\ell^{\rho}(\phi) g_m^{\rho}(\phi)\sin(k\phi)\, d\phi}_{\mathcal{I}^{\rho}_{\sin}=\mathcal{I}_6,\mathcal{I}_7} \\
& + \sum_{k=1}^{K}\left(x_k^{\rho\phi}+x_k^{\phi\phi}\right)\int_b^a f_\ell^{\phi}(\rho) f_k(\rho) f_m^{\phi}(\rho)\rho\, d\rho \underbrace{\int_{-\pi}^{\pi} g_\ell^{\phi}(\phi) g_m^{\phi}(\phi)\cos(k\phi)\, d\phi}_{\mathcal{I}^{\phi}_{\cos}=\mathcal{I}_1,\mathcal{I}_4} \\
& + \sum_{k=1}^{K}\left(x_{k+K}^{\rho\phi}+x_{k+K}^{\phi\phi}\right)\int_b^a f_\ell^{\phi}(\rho) f_k(\rho) f_m^{\phi}(\rho)\rho\, d\rho \underbrace{\int_{-\pi}^{\pi} g_\ell^{\phi}(\phi) g_m^{\phi}(\phi)\sin(k\phi)\, d\phi}_{\mathcal{I}^{\phi}_{\sin}=\mathcal{I}_6,\mathcal{I}_7}
\end{aligned}$$

Closed-form expressions, namely $\mathcal{I}_1, \mathcal{I}_4, \mathcal{I}_6, \mathcal{I}_7$, are derived for ϕ' integration and reported in the Appendix C.2. Hence, the (ℓ, m)-th element of the $\underline{\underline{X}}_s$ matrix computed with annular EBF is:

$$\begin{aligned} X_s^{\ell m} &= \left(x^{\rho\rho} + x^{\phi\phi}\right) \int_b^a f_\ell^\rho(\rho) f_m^\rho(\rho) \rho \, d\rho \begin{cases} \pi/2, \text{if } \ell = m \\ 0, \text{if } \ell \neq m \end{cases} \\ &+ \sum_{k=1}^K \left(x_k^{\rho\rho} + x_k^{\rho\phi}\right) \int_b^a f_\ell^\rho(\rho) f_k(\rho) f_m^\rho(\rho) \rho \, d\rho \begin{cases} \mathcal{I}_1 \\ \mathcal{I}_4 \end{cases} \\ &+ \sum_{k=1}^K \left(x_{k+K}^{\rho\rho} + x_{k+K}^{\rho\phi}\right) \int_b^a f_\ell^\rho(\rho) f_k(\rho) f_m^\rho(\rho) \rho \begin{cases} \mathcal{I}_6 \\ \mathcal{I}_7 \end{cases} \\ &+ \sum_{k=1}^K \left(x_k^{\rho\phi} + x_k^{\phi\phi}\right) \int_b^a f_\ell^\phi(\rho) f_k(\rho) f_m^\phi(\rho) \rho \, d\rho \begin{cases} \mathcal{I}_1 \\ \mathcal{I}_4 \end{cases} \\ &+ \sum_{k=1}^K \left(x_{k+K}^{\rho\phi} + x_{k+K}^{\phi\phi}\right) \int_b^a f_\ell^\phi(\rho) f_k(\rho) f_m^\phi(\rho) \rho \, d\rho \begin{cases} \mathcal{I}_6 \\ \mathcal{I}_7 \end{cases} \end{aligned} \tag{3.21}$$

As a result, to update $\underline{\underline{Z}}_s = j\eta_0 \underline{\underline{X}}_s$, only one numerical integration has to be performed along $\hat{\boldsymbol{\rho}}$ for each matrix entry. Moreover, as shown in the supplementary material in Appendix C.2, $\mathcal{I}_1, \mathcal{I}_4, \mathcal{I}_6, \mathcal{I}_7$ are non-zero only for a small number of combinations of k, ℓ, m, resulting in but only few modes to be computed. At the same time, the number of sample in ρ' scales with the antenna radius and not with its area. Thus, especially when the antenna dimensions are large with respect to wavelength, the computational cost is dramatically reduced compared to the matrix multiplication $\underline{\underline{\Psi}}^T \underline{\underline{Z}}_s \underline{\underline{\Psi}}$ that should have been computed instead.

3.3 Design Study Cases

In this section, we show numerical results of the automatic design of practically important and challenging MS antennas. In particular, we will address design of two large, high-gain so-called "holographic" MS antennas, and one linear leaky-wave antenna. The designs presented here rely on a-priori knowledge of existing literature results; most notably we take advantage of the knowledge of the relevant radiation mechanism behind these antennas, and we embed that into our parametrization of the antenna. Also, for each class of antennas we proceed as usual in any MS device design exercise: we start from a unit cell type, and map out reactance values with respect to geometrical parameters, as necessary in the final design phase from the IBC to actual antenna layout. In this case, what we need to know is only what are the *ranges* that the components of the reactance tensor take for realizable choice of unit cell parameters; this will constitute the bounds of the relevant parameters in our optimization. In this, we adopted results available in the literature. Knowledge of the relevant wave radiation mechanism allows to significantly restrict the number of parameters that describe the (continuous) impedance surface, learning from existing literature. For both the "holographic" and the leaky-wave antennas to be examined, the basic wave radiation mechanism can be traced to leaky-wave phenomena, and in particular to the fundamental work of Oliner-Hessel [32] and the leaky-wave interpretation of Maci et al. [3] of holographic antennas.

Holographic MS Antennas. We address center-fed circular layout MS antennas, with intrinsically tensor impedance and circular polarization radiation. We adopt the analytic form of the impedance spatial profile proposed in [12] and reported below in Sect. 3.3.1; of course, here the various parameters will be found through our numerical synthesis approach. The synthesizable range of unit cell layouts can also be derived from the literature, in particular in [12]. We will address both broadside radiation and tilted-beam cases. These antennas have a center region where the IBC surface is not present; hence, the most appropriate canonical shape is a circle with a circular hole, i.e. an annular shape; this explains this terminology in the following. We further note that in Chap.4, we show different kinds of modelling options for the feed region based on its complete 3D geometry. It is worth noting that, the approach based on the study of the feed in isolation of Sect. 4.2.3 can be integrated into the numerical synthesis by changing the right-hand-side of Eq. (3.1). This, however, falls out of the scope of the present work.

Rectangular Leaky-Wave Antenna. The basic architecture in this case is inspired by the work in [33]. That work is based on the classical Oliner-Hessel sinusoidal modulation, that led to the well-known semi-analytical design rules; here we extend the classical impedance profile to achieve flexibility, and in particular to obtain broadside radiation. This is motivated by the fact that broadside radiation is critical for designs based on the Oliner-Hessel theory [32], such as the method described in [33]; thus it well demonstrates the versatility of our hybrid analytical-numerical approach. In this case, we also design the actual antenna layout by realizing the synthesized IBC profile via rectangular strips, as in [33]. This appears to be a novel approach, also for its use of div-conforming rectangular EBF (described in Appendix D.1), and for the fast-factorization of transparent IBC-EFIE, and the comparison between the IBC radiation and that of the actual physical antenna.

3.3.1 Annular Holographic Metasurface Antenna: Pencil Beam

In the first two study cases we set the working frequency as $f = 30$ GHz, outer and inner radius $a = \lambda/4$ and $b = 5.7\lambda$ respectively, $\epsilon_r = 3$ and the layer thickness, $h = 0.764mm$. Starting from an impedance profile parametrized as in [12], and applying the algorithm of Tab. 3.1 with the amplitude masks depicted in Fig. 3.1, we obtain the results reported from Fig. 3.4 to Fig. 3.10. In this case, a reduced dimension, N_{design}, of the array p is possible due to the holographic theory on which the analytical design of such antennas [12] is based. The tensorial impedance profile $j\mathcal{X}$ is parametrized as follows:

$$
\begin{aligned}
X_{\rho\rho}(\rho,\phi) &= \bar{X}_{\rho}\left[1+M(\rho)(\cos(\beta_{sw}\rho-\Gamma(\rho,\phi))\right] && (3.22)\\
X_{\rho\phi}(\rho,\phi) &= \bar{X}_{\rho\phi}\sin(\beta_{sw}\rho-\Gamma(\rho,\phi)) && (3.23)\\
X_{\phi\phi}(\rho,\phi) &= \bar{X}_{\phi}\left[1-M(\rho)(\cos(\beta_{sw}\rho-\Gamma(\rho,\phi))\right] && (3.24)
\end{aligned}
$$

where

$$\Gamma(\rho,\phi) = k\rho\sin\theta_0\cos\phi+\phi=\Gamma$$

To obtain in an efficient update of the compressed IBC-MoM Matrix, as shown in Sect. 3.2, a slightly different ϕ' integration is performed due to the presence of the additional term

$$k\rho\sin\theta_0\cos\phi' = x\cos\phi'.$$

The derivation is not reported here but it is derived with the same procedure as in Sect. 3.2. The only additional tool needed to have a closed-form integration in ϕ' is the integral representation of the m-th order Bessel function:

$$\mathcal{J}_m(x)=\frac{(\pm j)^m}{2\pi}\int_{-\pi}^{\pi} e^{\mp j[x+\cos(\phi')\phi']}\,d\phi'. \tag{3.25}$$

Then, from the characteristic equation of the grounded dielectric slab (GS) we find X_0 and β_{sw}^{GS}. These parameters are needed in the transverse magnetic (TM) surface wave right-hand side model of (4.5). Taking into account the dependence of $\bar{X}_\rho$ from β_{sw} as in [13], we set the upper and lower bound for parameters of p as follows:

- p_1: $1.1<\beta_{sw}/k<1.8$ means $\bar{X}_\rho$ s.t. unit cells are synthesizable [13];
- p_2: $|M_\rho|<1$ radial modulation index;
- p_3: $|\bar{X}_{\rho\phi}|<0.4\eta_0$ s.t. unit cells are synthesizable;
- (p_4,p_5): geometrical tapering parameters of $M(\rho)$. $M(\rho)$ is a trapezoidal window, similar to Fig. 3.11.
- p_6: $\theta_0\in(-\pi,\pi)$ pencil-beam direction angle.

With p within the above listed constraints, we perform two different designs, one pointing at $\vartheta=0$, the other at $\vartheta=20$ [deg]. The results relative to the optimized design parameters p_i^* are summarized in Tab. 3.2. The computational effort is listed in Tab. 3.3.

Broadside Radiation: $\theta_0 = 0$

In this first case, based on the consideration of Sect. 2.4, we have factorized the IBC-EFIE MoM matrix with $M = 10$ axial and $N = \lceil 6a \rceil = 36$ radial annular waveguide modes, respectively. This mode selection results in $N_\Psi = 1511$ annular entire-domain basis functions. The selection is based on a fast spectral content estimation of the parametrized impedance profile via a similar calculation to those of Sect. 3.2. More details about the mode set selection can be found in Sect. 2.4. Figure 3.4 collects the radiation patterns for co-pol and x-pol, respectively. The masks used for the determination of the cost function F are depicted in Fig. 3.1 and Fig.3.5. The maximum directivity of 29.9 dBi is reached for co-pol (right-hand circular polarization) at $\theta_0 = 0$; the x-pol (left-hand circular polarization) is everywhere below 3 dBi. Continuous transparent IBC realizations (Eq. (3.22) and Eq. (3.23)) of p^*, namely $\underline{\underline{Z}}^s(p^*)$, are shown in Fig.3.6. The equivalent current density $\boldsymbol{J}^\Psi(p^*)$ is plotted in Fig.3.7a.

Tilted Beam Radiation: $\theta_0 = 20$

In the tilted beam case, the spectral content of the parametrized impedance profile is higher than the broadside case. Thus, we factorize the IBC-EFIE MoM system with $M = 20$ axial and $N = \lceil 6a \rceil = 36$ radial coaxial WG modes. This mode selection results in $N_\Psi = 2951$ annular EBFs. Figure 3.9 collects the u-v radiation pattern for co-pol (i.e. right-hand circular polarization) and x-pol (left-hand circular polarization). The radiation fits everywhere within the defined masks: Fig. 3.8. For the sake of completeness, (continuous) transparent IBC realizations (Eq. (3.22) and Eq. (3.23)) of p^*, namely $\underline{\underline{Z}}^s(p^*)$, are shown in Fig. 3.6. The equivalent current density $\boldsymbol{J}^\Psi(p^*)$ is plotted in Fig. 3.7b.

Table 3.2: List of p_i^* for broadside and 20 [deg] tilted-beam radiation

i	parameter	broadside	tilted-beam
1	β_{sw}/k	1.1146	1.1151
2	M_ρ	0.4453	0.447
3	$\bar{X}_{\rho\phi}$	-0.4η_0	-0.39η_0
4	r_b	0.25λ	0.25λ
5	r_a	0.14λ	0.06λ
6	θ_0	0	20

Table 3.3: Summary of computational results for numerical synthesis via annular EBF. Results obtained with Intel Xeon CPU E5-2687W v4 @3GHz.

Case	BF	DoF	Fact. $\underline{\underline{Z}}$	Compr. $\underline{\underline{\Psi}}^T \underline{\underline{Z}}\,\underline{\underline{\Psi}}$	Solving time	n of MoM eval	N it.
$\theta_0 = 0$	RWG	107710	40m	–	11m	684	106
	AEBF	1511	40m	22m	$<$ 1s		
$\theta_0 = 20$	RWG	107710	40m	–	11m	1096	176
	AEBF	2951	40m	1h20m	$<$ 1s		

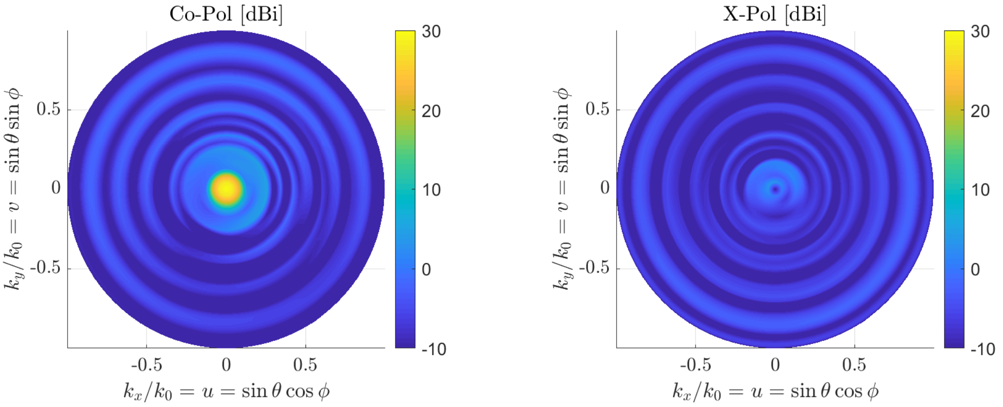

(a)

(b)

Figure 3.4: Polar radiation pattern generated by the designed anisotropic MS antenna. The masks for co-pol and x-pol are depicted in Fig. 3.1. Left (a): co-pol with a pencil beam centered in $\theta = 0$ and maximum directivity of 29.9 dBi. Right (b): x-pol uniformly below 3 dBi.

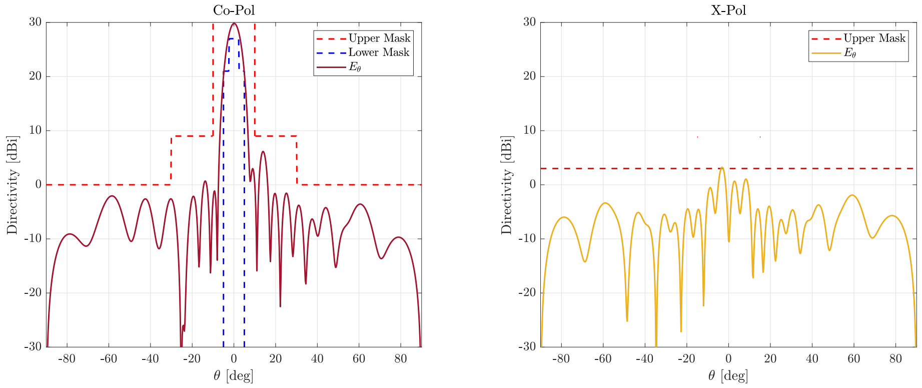

Figure 3.5: Directivity for the optimized sheet impedance $\underline{\underline{Z}}^s(p^*)$ vs amplitude masks (cut at $\phi = 0$) used in the design process. Left: co-pol directivity in solid dark red line, the dotted red and blue lines are the upper and lower masks. Right: x-pol directivity and relative upper mask set at a level 25dB lower than the max directivity.

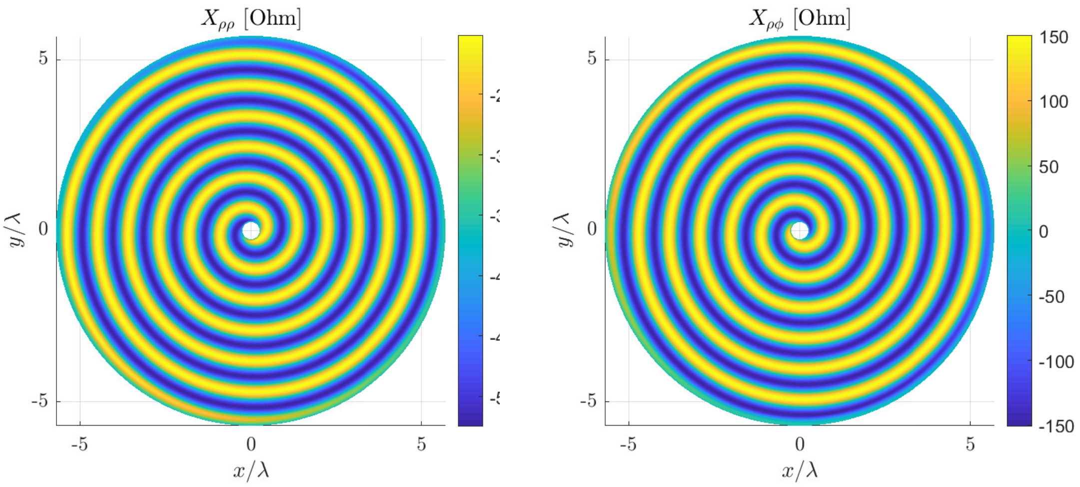

(a)

(b)

Figure 3.6: Continuous transparent IBC realization of p^*, namely $\underline{\underline{Z}}^s(p^*)$. Left (a): $\hat{\boldsymbol{\rho}}\hat{\boldsymbol{\rho}}$ component Eq.(3.22), with $\bar{X} = -362.6365\,\Omega$. Right (b): off-diagonal component, Eq.(3.23), of the tensor $\underline{\underline{Z}}^s(p^*)$.

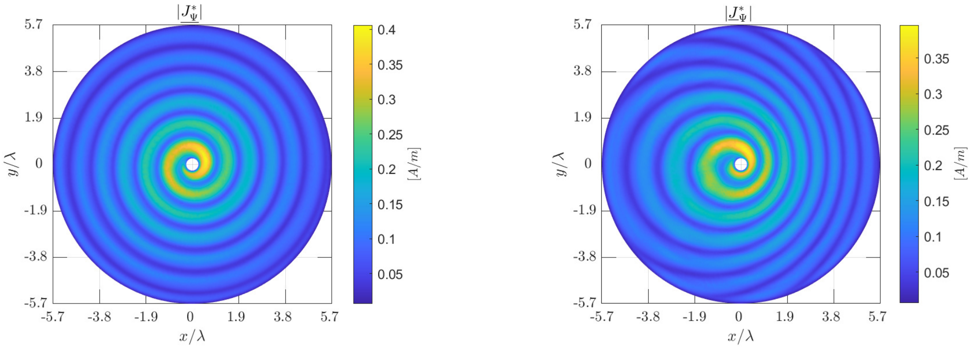

(a)

(b)

Figure 3.7: Left (a): equivalent current density $\boldsymbol{J}^{\Psi}(p^*)$ for broadside radiation. Right (b): equivalent current density $\boldsymbol{J}^{\Psi}(p^*)$ for squinted angle radiation of 20 degrees.

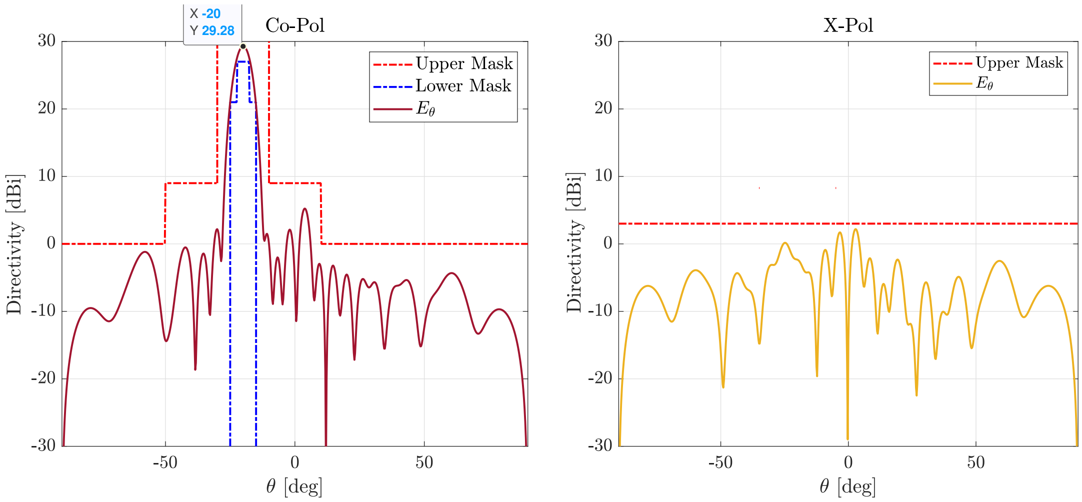

Figure 3.8: Directivity for the optimized sheet impedance $\underline{\underline{Z}}^s(p^*)$ vs amplitude masks (cut at $\phi = 0$) used in the design process. Left: co-pol directivity in solid dark red line, the dotted red and blue lines are the upper and lower masks. Right: x-pol directivity and relative upper mask at a level 25dBi lower than the max directivity.

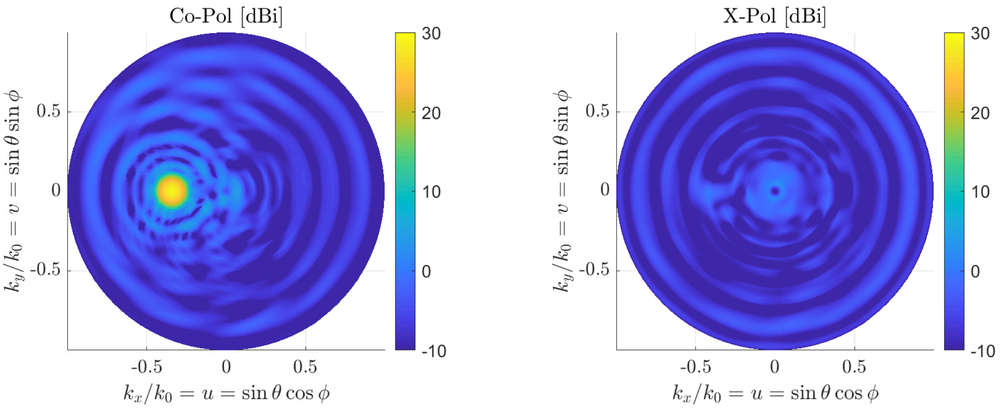

(a) (b)

Figure 3.9: Polar radiation pattern generated by the designed anisotropic MS antenna pointing at $\theta = 20$ degrees. Left (a): co-pol with a pencil beam centered in $\theta = 20$ deg and maximum directivity of 29.9 dBi. Right (b): x-pol uniformly below 3 dBi.

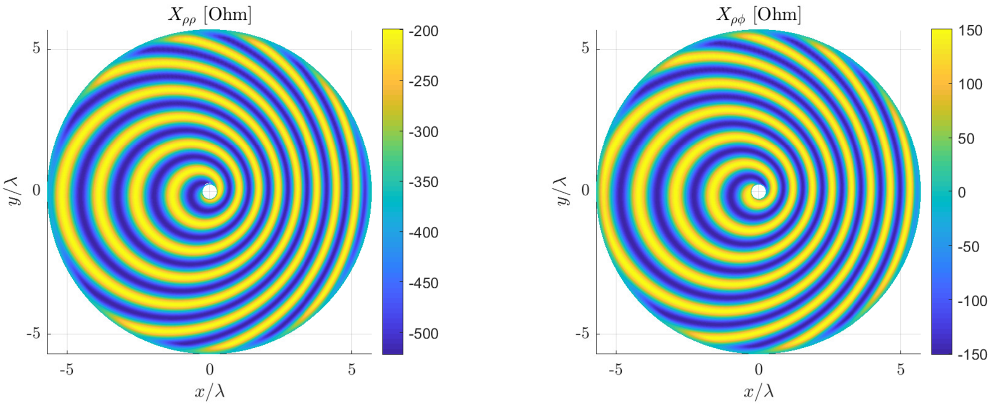

Figure 3.10: Continuous transparent tensorial IBC realization of p^*, namely $\underline{\underline{Z}}^s(p^*)$. Left (a): $\hat{\boldsymbol{\rho}}\hat{\boldsymbol{\rho}}$ component. Right (b): off-diagonal component of the tensor $\underline{\underline{Z}}^s(p^*)$, with $X_{\rho\phi} = -0.399\eta_0\,\Omega$.

3.3.2 Rectangular Leaky-Wave Metasurface Antenna: Broadside Radiation

This work is based on the classical Oliner-Hessel sinusoidal opaque modulation

$$Z(x) = jX_0\left(1 + M\cos\left(\frac{2\pi}{P}x\right)\right) \tag{3.26}$$

that led to the well-known semi-analytical design rules [33]. The scalar value X_0 is the average opaque impedance, M is the constant modulation factor, and P is the period of the modulation. Among others, one of the objectives in this test is to show the novel application of rectangular div-conforming EBF (see Appendix D.1 for supplementary materials). Of practical interest, the design of a LW antenna with broadside radiation. Here, we first set the working frequency to $f = 30$ [GHz], the dimension of the rectangular support along x and y as $a = 8\lambda$ and $b = \lambda$ respectively, $\epsilon_r = 3$ and the layer thickness $h = 0.764$ [mm]. Using the above mentioned background information, and the method described in [1], we extract the unit cell sheet impedance for a rectangular strip with a variable gap size as done in [33]. This is crucial for defining an admissible reactance range, and for the final geometrical implementation as textured unit cells, shown in Fig. 3.14a. Eventually, without reference to Floquet Theory, we derive a numerical optimal (w.r.t. cost function F) design of such a LW antenna.

Continuous Scalar IBC Optimal Design

The continuous scalar IBC resulting the from numerical synthesis is

$$X_{xx}(x) = \bar{X}\left(1 + M(x_1, x_2)\cos\left(\frac{2\pi}{P}(x - x_0)\right)\right) \tag{3.27}$$

Broadside radiation with directivity of 19.3 dBi and a side lobe levels lower than 10dBi are obtained for $\underline{\underline{Z}}^s(p^*)$. Figures 3.12 and 3.13 show the results for the equivalent current density and for the directivity at $\phi = 0$. It is worth noting the two side lobes fall out of the imposed mask. Further effort will be put in the automatic determination of ad-hoc masks starting from imposed antenna dimensions or conversely, ad-hoc antenna dimensions starting from imposed masks.

In the analyzed case, the number of RWGs defined over the rectangular domain is $N_\Lambda = 21864$. We set the rectangular EBFs to be $N = \lceil 6a \rceil = 48$ along $\hat{\boldsymbol{x}}$ and $N = \lceil 4b \rceil = 4$ along $\hat{\boldsymbol{y}}$; this choice results in $N_\Psi = 436$ rectangular EBFs.

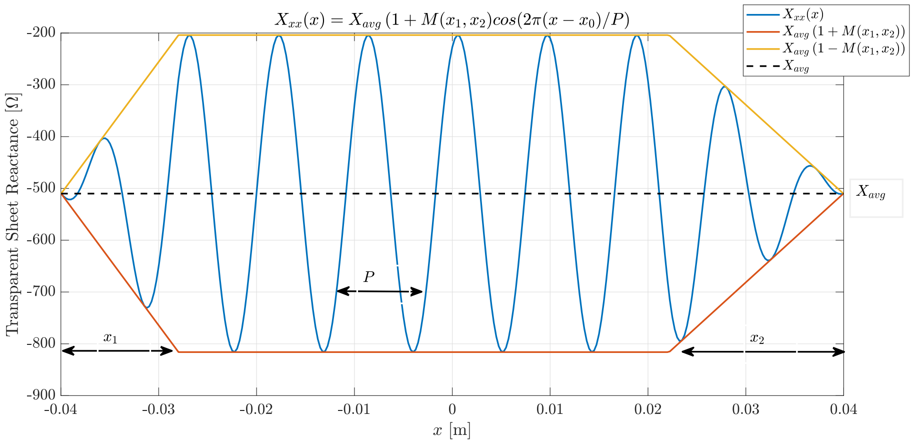

Figure 3.11: The blue line is the continuous scalar transparent IBC $\underline{\underline{Z}}^s(p^*)$ obtained for broadside radiation masks. The yellow and the red lines represents the trapezoidal window used to taper the IBC. The black dotted line is the average sheet reactance.

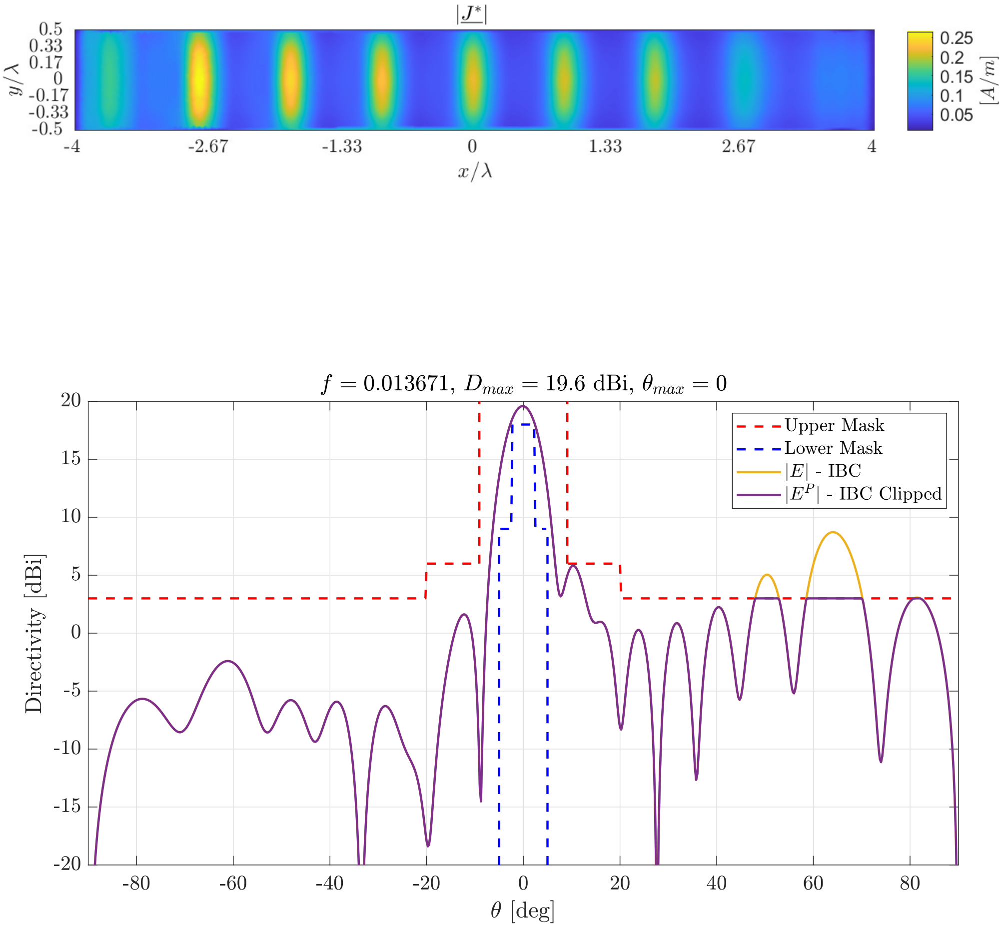

Figure 3.12: Top: Equivalent current density $\boldsymbol{J}^{\Psi}(p^*)$ obtained with continuous IBC model. Bottom: Directivity of IBC model (yellow line) vs. the clipped version (dark red) when convergence is already reached. The L2 norm defined between the yellow and the dark red lines strictly defines the cost function, $F = 0.013$, see Eq. (3.5). The dotted red and blue lines are the upper and lower masks, respectively

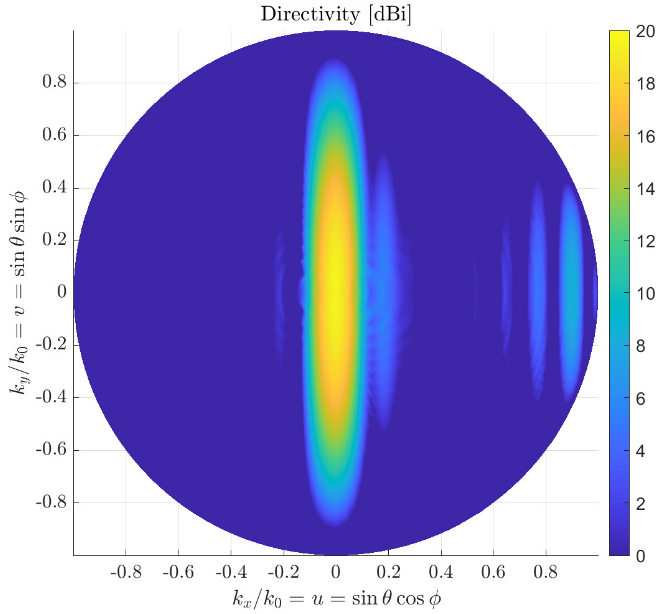

Figure 3.13: Broadside radiation with directivity of 19.3 dBi and a SLL of 10dB are obtained. The $u - v$ pattern of the textured Leaky-Wave Antenna.

Table 3.4: List of p_i^* for broadside LW antenna radiation, see Fig. 3.11 for cross-reference to parameter definition

i	Parameter	p_i^*
1	$\bar{X}$	-1.353η_0
2	M	0.6
3	P	0.915λ
4	x_0	1.20λ
5	x_1	3.05λ
6	x_2	-3.23λ

Comparison between Continuous IBC Model and Textured Unit Cells Realization

A sinusoidal modulation is physically realized by varying the gap width between parallel strips. To this purpose the graph in Fig. 3.14b is used. The first step requires the computation of the sheet admittance of this surface. Using the technique described in [1], a unit cell made by a rectangular patch printed on a grounded dielectric substrate is implemented in an in-house periodic solver. In order to extract the scalar impedance, two orthogonal illuminations are performed. From the obtained data, the sheet admittance is derived and plotted in Fig. 3.14b and Fig. 3.14a as a function of the gap between two neighboring unit cells. Comparison between the continuous scalar IBC model and its actual textured realization of Fig. 3.14a are shown in Fig. 3.15. Directivity comparison between the continuous scalar IBC model and the its textured realization show a good agreement.

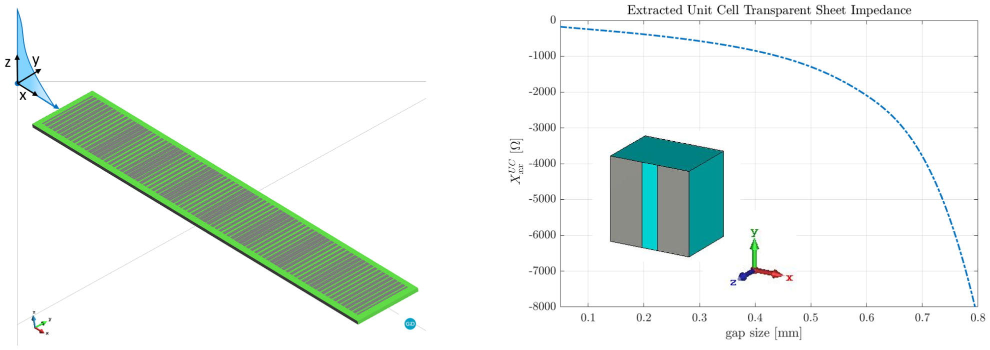

(a) (b)

Figure 3.14: (a) Textured Leaky-Wave Antenna made of sub-wavelength strips designed at 30GHz. The structure is excited by a TM Surface Wave (blue rendering) propagating along the structure. (b) Unit cell (geometry depicted in inset) sheet impedance for a rectangular strip with a variable gap size as in [33].

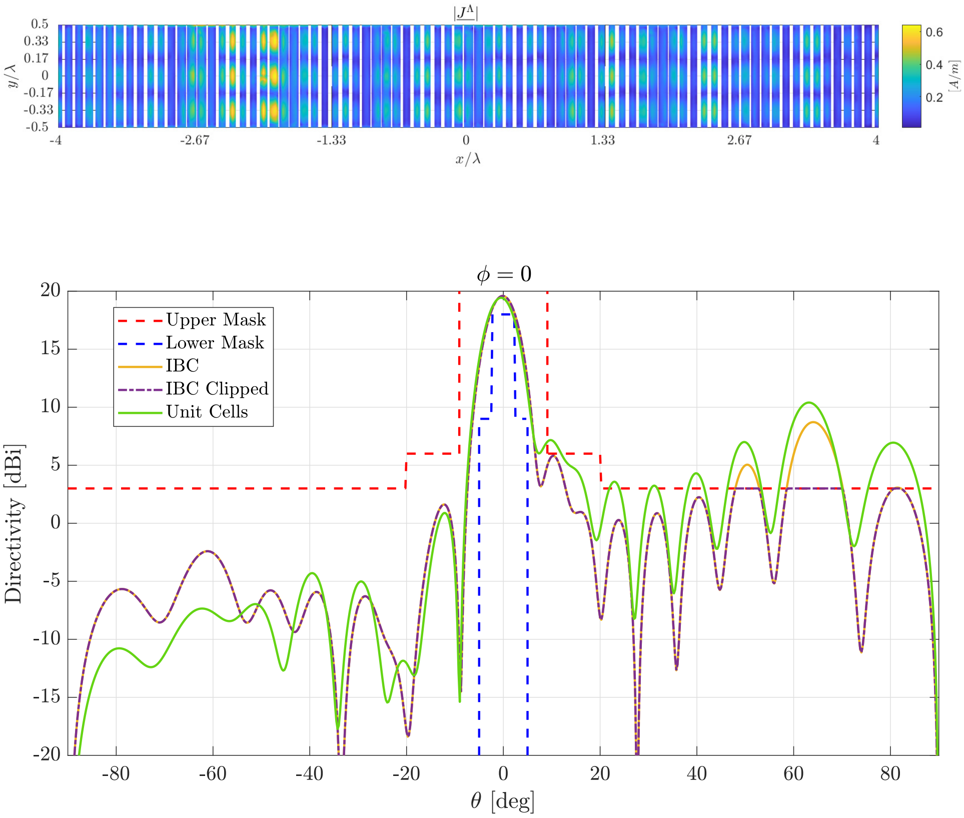

Figure 3.15: Comparison between continuous scalar IBC model and its actual textured realization of Fig. 3.14a.Top: Equivalent current density $\boldsymbol{J}^\Lambda(p^*)$; note that the electric current is on the conducting strips only. Bottom: Directivity comparison between continuous scalar IBC model (yellow line) and its textured realization (green line). The dotted red and blue lines are the upper and lower masks, respectively.

3.4 Conclusions

The design of metasurface antennas is approached as an optimization process for the spatial distribution of the impedance boundary condition (IBC). The use of full-wave simulation in this optimization cycle is made possible by aggregating the underlying RWG functions into entire-domain basis functions (EBF), in the form of waveguide modes. It is shown that this is advantageous in terms of the total numerical resources required in the optimization process. The scheme is applied to the design of two relevant classes of metasurface antennas. We present numerical results on the optimization of the tensorial sheet impedance for metasurface antennas to satisfy amplitude constraints imposed with masks. Leveraging on a compressed formulation which greatly reduces the computational burden associated with repeated solutions of the integral equations describing the currents solution, we develop an algorithm which modifies the surface impedance to obtain a surface current radiating a pattern within the imposed mask. Further research will be addressed to the automatic determination of ad-hoc masks starting from imposed antenna dimensions or conversely, the determination of ad-hoc antenna dimensions starting from imposed masks.

Chapter 4

Analysis of Modeling Options for Metasurface Antennas

State-of-the-art metasurface antenna modeling still relies on an approximated feed scheme which aims to either reproduce experimental or ideal theoretical results. We develop a 3-D full-wave numerical approach based on electric field integral equation (EFIE) to describe the feed accurately, and to gain access to the related figure of merit. Moreover, the 3-D full-wave analysis is also integrated into the approximated IBC-EFIE model, extensively used in the preceding two chapters in its 2-D planar version. Here we demonstrate the agreement between our 3-D solution and already established methodology. We also compare to commercial solver the return loss (RL) for the feed in isolation. Comparison with actual measurements is ongoing. Due to the peculiar nature of these antennas, we show that the feed region can be decoupled from the radiative parts (i.e. IBC or unit cells). Its standalone analysis gives relevant design information. This characteristic allows us also to propose novel 2-D models derived from the analysis of the feed region in isolation. This results, for instance, can give access to the feed-related figure of merit during the optimization loop described in Chap. 3. To the best of the author knowledge, these results have not been published before. Eventually, we compared the numerical results (IBC and Unit Cells) to real-life measurements. To this aim, we acknowledge the University of Siena and Wave-Up for providing results for the test cases. This chapter concludes with the introduction of a novel hybrid scheme for the analysis of a large MS with full 3-D mesh. Preliminary results concerning the compression of the feed region are shown.

4.1 Introduction and Motivations

Metasurface antennas are planar multi-layer configurations of sub-wavelength building blocks (i.e. unit cells) typically printed on a grounded dielectric slab (e.g. [4]). Due to the sub-wavelength nature of the unit cells, homogenization techniques can be applied, leading to a macro-scale description via an "approximate" IBC model [39]. Thus, even in the numerical modeling, MS antennas are intrinsically a multiscale problem; however, recent literature has shown that most of the design can be done via MS homogenization and the IBC-EFIE [18]. Moreover, MS antennas radiation is well described in terms of a continuous slowly varying electric sheet tensorial reactance, namely $\boldsymbol{\mathcal{Z}}^s$, interacting with a surface wave, which is gradually transformed into a leaky wave [14]. A vertical probe (i.e., the copper core of a coaxial cable: layout and detail of the feed region on the left side of Fig. 4.1) excites a cylindrical surface wave on the surface impedance, and the latter converts the excitation into a leaky wave. The excitation of the surface integral equation (SIE) can be modeled at two different scales. The microscale involves the 3D feed modeling, while the macroscale implies the closed-form calculation of the asymptotic field produced by a vertical dipole in a grounded slab. The right side of Fig. 4.1 shows the mesh of a typical feed structure, composed by planar equivalent magnetic currents, modeling a cross-section of the coaxial cable at the ground level (blue triangles), and electric equivalent currents, modeling a vertical cylindrical probe and two planar annular rings at the unit-cell level, i.e. h_d (red triangles). The use of a decoupled 2-D expression dramatically simplifies the numerical complexity in a layered media environment, reducing the computational problem from a 3-D problem to a planar problem. To this aim, we propose in subsection 4.2.3 a novel 2-D approach derived from the analysis of the 3-D feed region in isolation. The same approach can be extended, for instance, to the feed region surrounded by an IBC plate loaded with an average reactance. It is worth noting that the average reactance of the IBC plays a crucial role in the feed design because it is responsible for launching the surface wave. In Sect. 4.2 we show in detail three different source modeling options. For the sake of completeness, we briefly describe the TM Surface Wave model. Then we describe the 3-D feed region and also how to use it in a fast MoM framework such

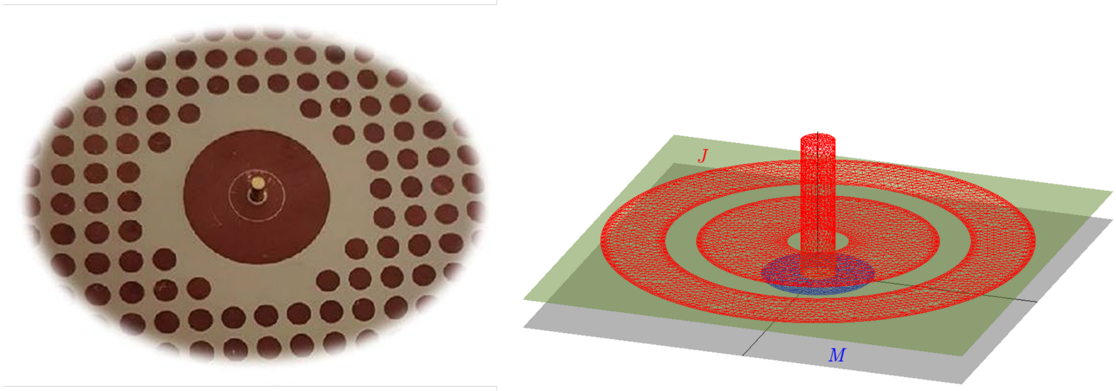

Figure 4.1: Left: example of MS textured layout and details of the feed [4]. Right: schematics and mesh of the feed model.

as the discretization of the IBC electric field integral equation (EFIE). It is worth noting that, this approach is not only valid for the "homogenized" IBC-EFIE, as shown in Sect. 4.2.5, but also for the standard EFIE in layered media, used to simulate the actual MS made of sub-wavelength patches. Then, in Sect. 4.2.3 we proceed with the analysis of the feed in isolation, including the S_{11} comparison with the commercial software CST. Section 4.2.4 explores the impact and the contribution of the presented modeling options to the IBC radiation. Eventually, we extend the analysis comparing the IBC approximation with the actual MS antenna realized with textured unit cells. The numerical results are also compared to measurements using a test antenna realized and provided by the company Wave Up. In Fig. 4.2 is shown the equivalent current density of the provided IBC model, and Fig. 4.3 schematically shows the relative positions and details of feed region. As mentioned in the manuscript roadmap, Chap. 1, the class of antennas under investigation in this chapter is center-fed. The feed structure almost invariably involves vertical metalizations, that are know to slow the solution in the layered-medium formulation. To ease that burden, Sect. 4.3 introduces of an ad-hoc hybrid factorization scheme for the analysis of large metasurface using a full 3D mesh. Preliminary results concerning the compression of the feed region are shown.

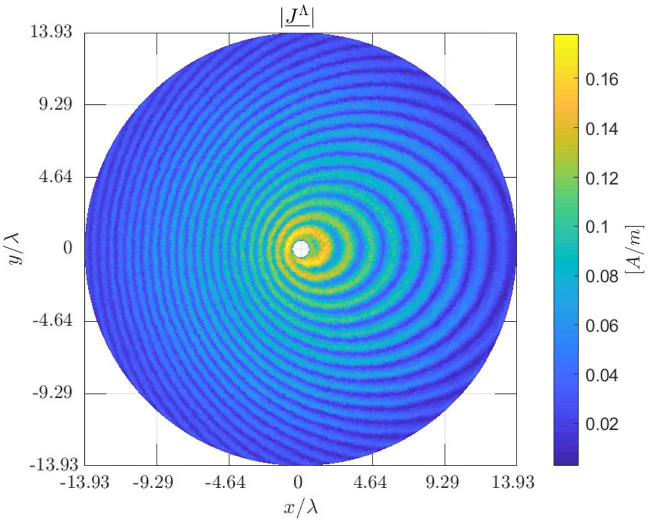

Figure 4.2: Equivalent current density of IBC-EFIE solution for the case of study of this chapter.

4.2 Feed Modeling in MoM Formulation

The surfece integral equation (SIE) formulation for the equivalent current $\boldsymbol{J}$ of the IBC-EFIE [18] follows the standard MoM approach which leads to the linear system

$$\left(\underline{\underline{Z}} - \underline{\underline{Z}}^s\right)\underline{J} = \underline{b}, \tag{4.1}$$

where $\underline{J}$ is the vector which collects the unknown coefficients of $\boldsymbol{J}$ in the RWG basis; the matrix entries are

$$\begin{aligned} Z_{m\ell} &= \langle \boldsymbol{\Lambda}_m; \boldsymbol{\mathcal{G}}^{\boldsymbol{EJ}}; \boldsymbol{\Lambda}_\ell \rangle && (4.2)\\ Z^s_{m\ell} &= \langle \boldsymbol{\Lambda}_m; \boldsymbol{\mathcal{Z}}^s \cdot \boldsymbol{\Lambda}_\ell \rangle. && (4.3) \end{aligned}$$

where $\boldsymbol{\mathcal{G}}^{\boldsymbol{EJ}}$ is the layered media dyadic Green's function when only electric sources are considered and $\boldsymbol{\Lambda}$ are the RWG basis/test functions used for the electric current discretization. The layered media formulation employed is the mixed-potential "Formulation-C" introduced by Michalski et al. in [31]. The m-th element of the right-hand side is:

$$b_m = \langle \boldsymbol{\Lambda}_m; \boldsymbol{E}^i \rangle. \tag{4.4}$$

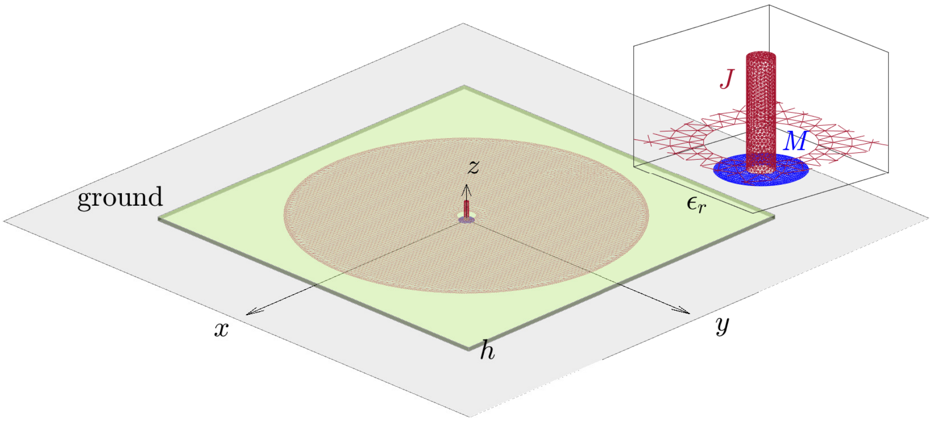

Figure 4.3: Simple MS schematics with mesh of both electric (red) and magnetic (equivalent) currents on the ground plane (blue) for the vertical feed model.

4.2.1 The TM Surface Wave

A vertical probe (i.e. copper core of a coaxial cable: layout and detail of the feed region on the left-side of Fig. 4.1) excites a cylindrical surface wave on the surface impedance, and the latter converts the excitation into a leaky wave. The excitation of the SIE has then a transverse component which is asymptotically

$$\boldsymbol{E}_t^{sw} \approx jX_0 H_1^{(2)}(\beta_{sw}^{GS}\rho)\hat{\boldsymbol{\rho}} \tag{4.5}$$

where $H_1^{(2)}$ is the Hankel function of the second kind and first order. The reactance X_0 and the wavenumber β_{sw}^{GS} are derived solving the characteristic equation of the grounded dielectric slab (GS) of thickness h_d and permittivity ε_r. A simple schematic of the MS is provided in Fig. 4.3. The use of such an expression greatly simplifies the numerical complexity in a layered media environment, reducing by one-dimension the computational problem, i.e, from 3-D to planar. On the one hand, the use of such a closed-form asymptotic expression provides reliable results during the first stage of the design, when only the directivity is of interest; on the other hand, it is an "approximate" model and, among other things, does not give access to the figure of merit such as S_{11}, which is of crucial importance in the final stage of the MS antenna design.

4.2.2 Full Geometry of Feed

The incident field $\boldsymbol{E}^i$ is modeled assuming that the aperture of the transmission line contains only a TEM mode field distribution. Using the well-known magnetic frill excitation model [38] the aperture electric field is replace by equivalent magnetic currents on the ground plane, $\boldsymbol{M}_a$ (see Fig. 4.3), and the incident field can be written as

$$\boldsymbol{E}^i(\boldsymbol{r}) = \int_{\Sigma} \boldsymbol{\mathcal{G}}^{\boldsymbol{EM}}(\boldsymbol{r},\boldsymbol{r}') \cdot \boldsymbol{M}_a(\boldsymbol{r}')d\boldsymbol{r}' \tag{4.6}$$

where $\boldsymbol{\mathcal{G}}^{\boldsymbol{EM}}$ is the multi-layer dyadic Green's function with only magnetic sources. The reflection coefficient at the point of feed Γ, often called S_{11}, is an extremely important design parameter. It is linked to the input impedance Z_{in} through

$$\Gamma = \frac{Z_{in} - Z_0}{Z_{in} + Z_0} \tag{4.7}$$

[26]. In order to calculate the antenna input impedance or, equivalently, the antenna admittance $Y_{in} = 1/Z_{in}$, we follow the variational approach in [28] useful for coaxial fed antennas. The input admittance is expressed by

$$Y_{in} = -\frac{\langle \boldsymbol{M}_a, \boldsymbol{H}_T \rangle}{V^2} + \frac{\langle \boldsymbol{J}, \boldsymbol{E}_T \rangle}{V^2} \tag{4.8}$$

where $\boldsymbol{H}_T$ and $\boldsymbol{E}_T$ are the total magnetic and electric fields due to both $\boldsymbol{M}_a$ and $\boldsymbol{J}$ and V is the voltage across the gap at the aperture of the coaxial line. If Galerkin's method is used as in our case, then it is easily shown that $\langle \boldsymbol{J}, \boldsymbol{E}_T \rangle = 0$. In this case, only the first term in Eq. (4.8) remains or

$$Y_{in} = -\frac{\langle \boldsymbol{M}_a, \boldsymbol{H}_a \rangle}{V^2} = -\frac{\langle \boldsymbol{M}_a, \boldsymbol{H}_s \rangle}{V^2} - \frac{\langle \boldsymbol{M}_a, \boldsymbol{H}_T \rangle}{V^2} \equiv Y_{coax} + Y_{antenna} \tag{4.9}$$

The first term on the right-hand side is identifiable as the contribution to the input admittance from the coaxial gap capacitance (proportional to ω). The second term is due to the antenna structure and can be, for convenience, further divided into sub-contributions due to well identified antenna sub-structures (ex. feed, coupler, etc.). Interestingly, if the medium dyadic Green's function posseses certain properties (see [38]) the admittance can be easily calculated from the electric current solution $\underline{J}$ and system forcing term (r.h.s) $\underline{b}$:

$$Y_{antenna} = -\frac{\underline{J}^T \underline{b}}{V^2} \tag{4.10}$$

Calculation of input admittance/impedance and S_{11} and comparison with other numerical approaches will be shown in the following sections.

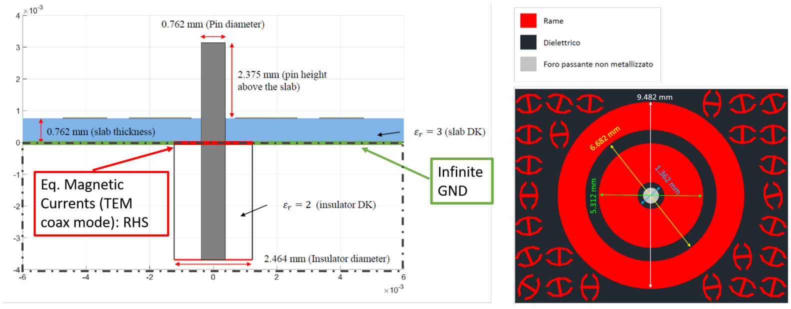

Figure 4.4: Feed region schematic. Left: xz-view of the feed region. Right: xy-view of the feed placed in a Metasurface Antenna.

4.2.3 Structure Domain Decomposition: Feed in Isolation

It is not only instructive but also a useful design approach to consider the feed part of the antenna structure in isolation (i.e., disconnected from the rest of the antenna). In the case of the MS type of antennas under consideration, this is particularly meaningful because it often constitutes the only fully 3D structure of the antenna, and it leads thus to a natural and intuitive system domain decomposition. Figure 4.4 shows the feed geometry schematics. To validate our MoM model for the feed, we compare the directivity and S_{11} with CST calculations. In order to reproduce the infinite slab medium underlying our model, we use an absorbing boundary condition in CST, which eliminates the reflection of the wave travelling in the dielectric layer. The comparison in Fig. 4.5 shows reasonable agreement between the two approaches. The near field of the isolated feed can be used to excite the 2D radiating antenna (IBC or unit cells) similarly to the incident field generated by the magnetic current in Eq. (4.6) as described in the next section.

We then compare the far-field pattern of the MS antenna calculated with the surface wave equation (2D), the full 3D structure with magnetic frill excitation (3D), and the isolated feed $\boldsymbol{E}^i$ (2D). As can be seen in Fig. 4.7, the patterns are very similar among the three forcing models, which suggests that, for these kinds of structures, the feed can be substantially decoupled from the rest of the structure. This conclusion is further corroborated by the analysis of the different contributions to the total input admittance as shown in Fig. 4.6b.

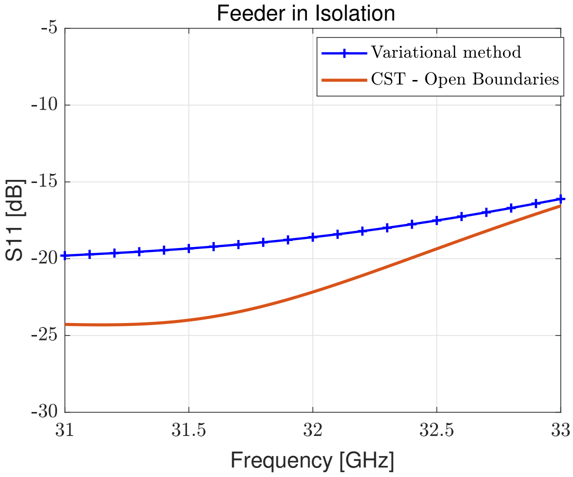

Figure 4.5: Comparison between S_{11} computed at different points in frequency with the variational method (blue line) and the CST (red line).

4.2.4 Impact of Feed Modeling on IBC Radiation

We simulated a MS antenna at 32.3 [GHz] of radius almost 14λ with a IBC model provided by Wave-Up. The permittivity is $\epsilon_r = 3$ and the layer thickness is $h = 0.764$ [mm]. Such problem, produces a IBC-EFIE MoM system with almost 800K RWGs. We have shown the equivalent electric current density in Fig.4.2. In Fig.4.7 we compare the directivity using three excitation models: the realistic 3D model with magnetic frill excitation in Fig. 4.3, with SW from Eq. (4.5) and the isolated feed radiation $\boldsymbol{E}^i$. It is worth noting that the computational effort for the three simulations is rather different since the last two needs only 2D geometry, whereas the first is a full 3D model. The far-field patterns of the MS antenna calculated, are very similar among the three models, which strongly suggests that, for these kinds of structures, the feed unknowns can be substantially decoupled from the rest. This result is not very surprising on the Far-Field radiation, considering that also the well-established 2D TM surface wave model is based on the same concept and has always provided reliable results in recent years.

This conclusion is further corroborated by the analysis of separate contributions to the total input admittance as in 4.6b. The input admittance of the isolated feed, divided into coaxial and self contributions (full lines in Fig. 4.6b), is only slightly modified by the presence of the primary antenna. The feed dominates the total Y_{in} of the antenna, with $Y_{coaxial}$ being dominant in the imaginary part and the self-feed Y_{feed} in the real part. The IBC contribution is found to be rather negligible in these cases. These results open up the possibility of a simplified feed and main antenna design and optimization by decoupling the two sub-systems.

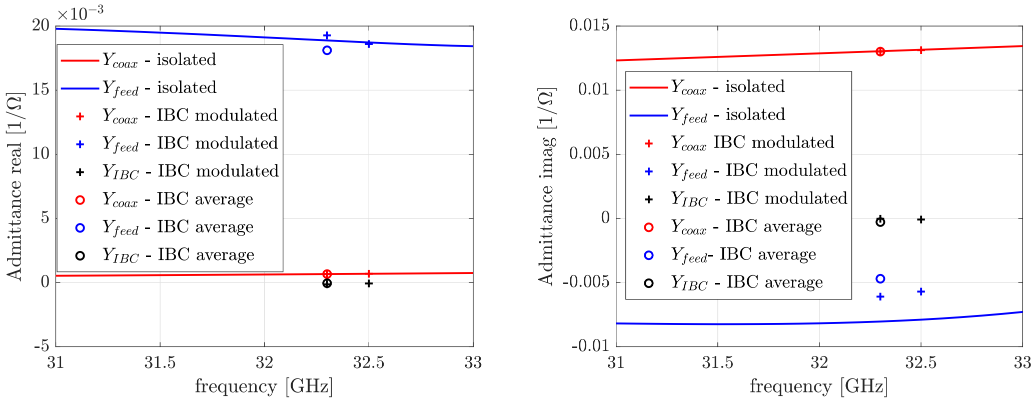

(a) (b)

Figure 4.6: Input admittance analysis and decomposition. Both real (left) and imaginary (right) parts are given. The full lines refer to the isolated (decoupled) feed, the symbols to the decomposition of admittance contributions in a full 3D simulation with modulated (cross) and average (circle) IBC.

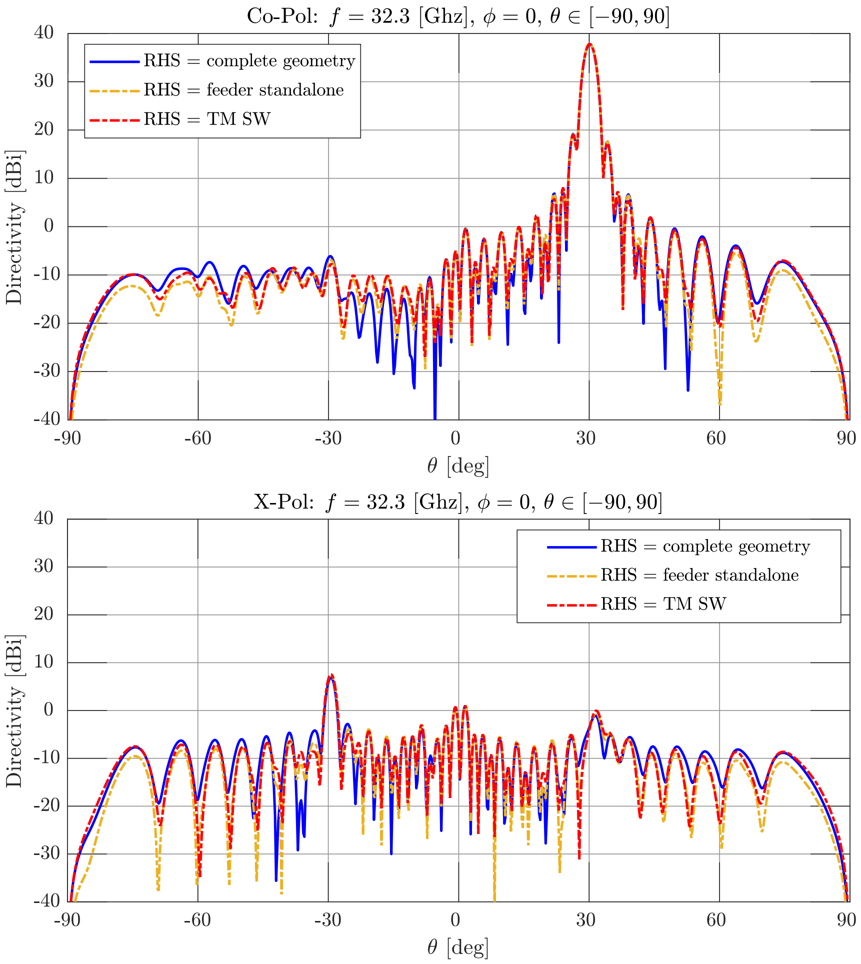

Figure 4.7: Directivity of isotropic MS antenna: co-pol (top) and x-pol (bottom) radiated by the antenna for $\theta \in [-90{,}90]$ and $\phi = 0$ with different r.h.s. Blue solid lines refer to complete 3D model, red solid lines to the SW model (2D), and the dashed orange line to the isolated feed excitation (2D).

4.2.5 Comparison between IBC Approximation, Full Unit Cell Model and Measurements

In this subsection, solutions obtained with IBC and the full layout are compared with one each other, and against measured data on the realized antenna. The full layout is depicted together with the equivalent current densities in Fig. 4.8. This section ties together many aspects to which this thesis was devoted. Encouraging results of Fig. 4.9 show good agreement between the unit cell model and the approximated IBC. Measured data confirm the validity of both models used so far. There is still space for improvements though, e.g. on side lobes. We suspect that the lack of accuracy may be due to the infinite model of the background (ground and dielectric). Possible solutions to overcome these limits are under investigation as well as possible multi-mode modeling of the coaxial feed via mode-matching. The Table 4.1 summarizes the computational effort needed to simulate the full layout of the MTS antenna under investigation in this chapter. Summing together the total computational times, we conclude that the full-simulation of MTS of similar dimension takes approximately a day. This significant overall timing for the computation only one solution on a high performance machine, explains why different approaches were adopted at different scales to tackle the analysis and the design of such devices. Similar computational results can be found for the IBC counterpart. With the aim of also further reducing the computational cost for the final analysis of the full layout, we present a hybrid GIFFT-Skeletonization formulation in the next section.

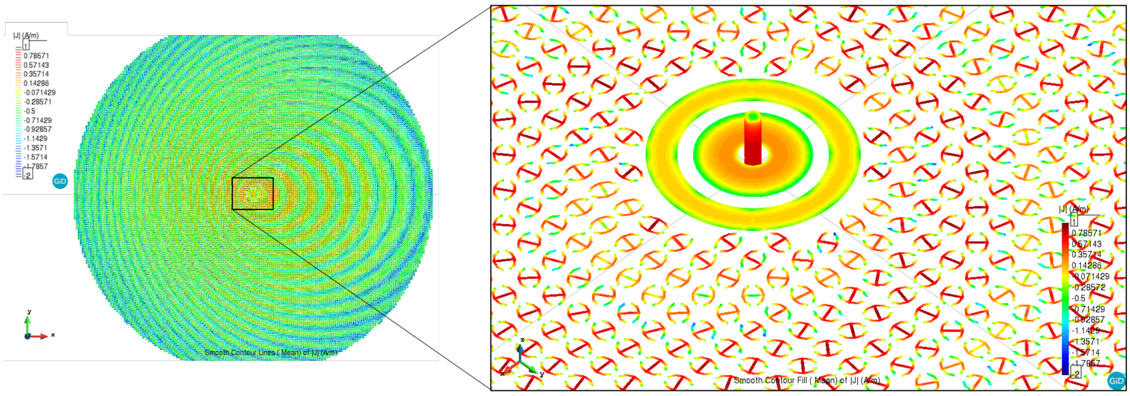

Figure 4.8: Left: equivalent current density of the full textured unit cell model. Right: zoom on the feed region.

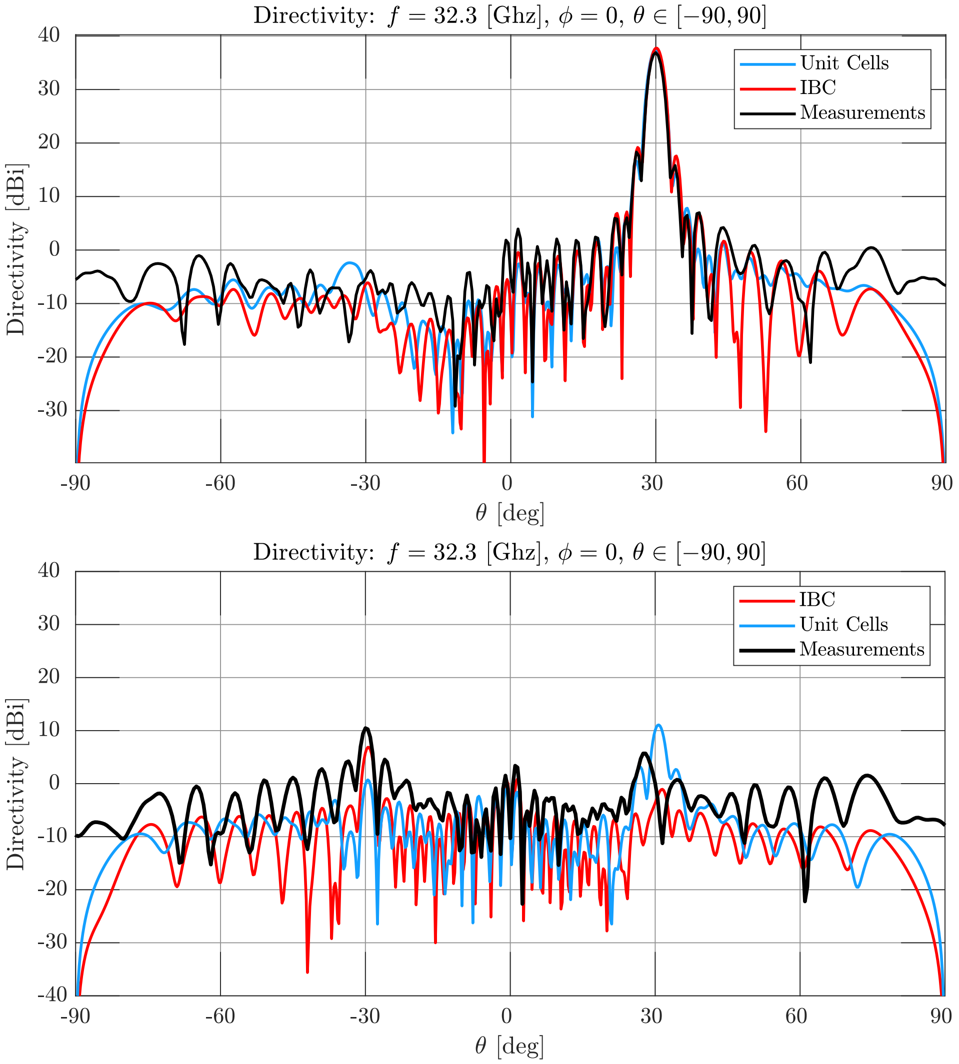

Figure 4.9: Directivity of isotropic MS antenna: co-pol (top) and x-pol (bottom) radiated by the antenna for $\theta \in [-90{,}90]$ and $\phi = 0$. Blue solid lines refer to the unit cell model, red solid lines to the IBC model. The black lines are the measurements of a prototype (i.e. textured unit cells).

4.3 Fast Hybrid Scheme: GIFFT and Skeletonization

As already mentioned, to be able to treat a large planar structure with vertical terms appearing in a few parts, e.g. in the feed, we apply the GIFFT acceleration-compression method [5] to the 2D self-planar part of the MoM matrix. This method alone allows us to run a full-wave MoM solver on antennas with planar parts of typical linear size of 10-15λ discretized with about $N_p \approx 10^6$ RWG and a vertical feed region with $N_f \approx 10^3$ RWG within reasonable CPU times (10-24h on multi-core machines) and memory (<100GB).
Dealing with multiple-feed points, multi-layers or simply larger structures requires further acceleration and system matrix compression. The cross planar-vertical, inter-planar and electrically large self-vertical subblocks of the system matrix represent interactions between clustered groups of "far" basis functions and are (numerically) rank deficient. Thus, due to their low-rank nature, algebraic methods, such as the skeletonization schemes of [27, 34], efficiently compress the sub-blocks mentioned above.

4.3.1 Formulation and Implementation

Following the scheme introduced in [27], we describe the interaction between two groups of (far) basis functions in terms of the following factorization:

$$Z \approx U^T \tilde{Z} V \equiv Z_{approx} \tag{4.11}$$

where U^T and V are the anterpolation and interpolation matrices and $\tilde{Z}$ is the low-rank interaction matrix between the two sub-groups and contains the interactions between the principal functions often called skeletons. Hierarchical schemes, such as Octree, subdivide larger domains. To find the skeleton list and the anterpolation/interpolation matrices of a sub-groups, we use the idea of proxy surfaces. Indeed, instead of building

Table 4.1: Summary of the resources required with the Intel Xeon CPU E5-2687W v4 @3GHz. N_Λ is the total number of RWG. "RHS Eval." is the time necessary to evaluate the RHS in the full geometry model when about 500 magnetic functions are used to represent the TEM fundamental mode of the coaxial waveguide. "Far-Field Factorization" and "Near Field" are the far-field factorization time and near-field time, respectively. The "Planar-Vertical" column is the time needed to compute the planar-vertical and self-vertical interactions. "Solving Time" refers to the number of iterations reported in the "Iterations" column using the Flexible GMRES iterative solver.

N_Λ	RHS Eval.	Far-Field Factorization	Near Field	Planar Vertical	Solving Time	Iterations	Memory Peak
1M	1h30m	15m	45m	4h15m	11h	550	40 GB

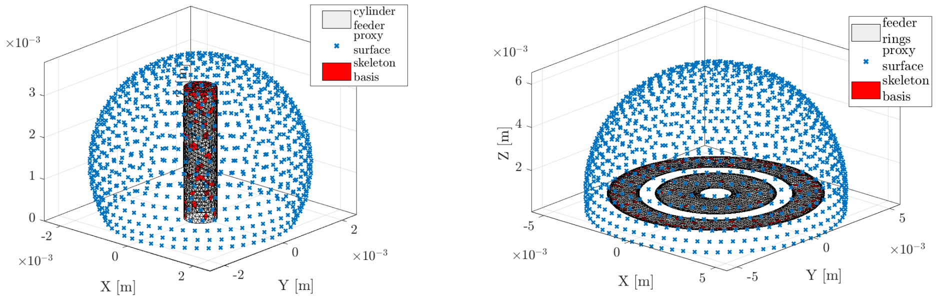

(a) (b)

Figure 4.10: Left(a): Skeleton cylinder. Right(b): Skeleton rings. Red triangles reveal the skeleton basis function. The blue dots represent the delta-function discretisation of the spherical proxy surface.

the entire block row and block column of a group (in order to compress it), we only evaluate the interactions between the sources (test) of the group and a set of test (sources) auxiliary functions. The proxy surface, typically a canonical surface, such as the sphere sector of Fig. 4.10, can be discretized with test vector Dirac deltas (sometimes referred to as samples) or linear functions such as RWGs. The electric field of the sources is then projected onto the test functions. This procedure generates a matrix Z_S , that is compressed using the interpolative decomposition (ID) representing the interaction between the sub-domain and the proxy surface. The ID takes as input the low-rank matrix Z_S and a user-defined tolerance; then it outputs the rank of the matrix, a set of the dominant indices, I_s (that corresponds to the skeletons), and a basis matrix V which is used for the interpolation. Eventually, the scheme proceeds to the second sub-groups in order to obtain factorization of the original sub-block as in Fig. 4.11. Figure 4.10 shows a simple test in free-space (with the ground plane) for a feed using spherical proxy and delta-Dirac function discretization. The red RWGs correspond to the selected skeletons. Compression ratios, defined as the number of skeletons over the total RWGs, larger than 10 can be easily achieved with a residual Frobenius norm $\|Z - Z_{approx}\| < 1\%$.

4.3.2 Preliminary Results

The skeleton method has been applied in different and successful ways to the free-space Green's function kernel. It also belongs to the so-called kernel-free methods, which do not rely on any specific property of kernel one wishes to approximate and compress. Thus, a priori, it should be directly applicable to the layered media Green's function kernel under consideration. In order to check this expectation we performed a compressibility test by applying a SVD to the previous interaction matrix Z in free-space and in a layered media with $\varepsilon_r = 3$. The singular values are plotted in Fig. 4.11. As expected the spectrum in free-space is rapidly decaying indicating good compressibility. Free-space Green's function are easily written in closed form and thus numerically very accurate. However, the layered media Green's function is numerically approximated in several ways. First, no closed form is available and the evaluation requires numerical integration which introduces certain — to some extent controllable — inaccuracy. Second, to further accelerate its evaluation, interpolation methods are often used [27, 34] which inevitably reduces the global accuracy. Less accuracy means more (white) noise which is incompressible having a flat random distribution. We may then anticipate ID to be less effective for numerically evaluated kernels. Unfortunately this seems to fit well with the very different SVD spectrum observed for the layered case in Fig. 4.11. The present interpolator implemented in the MoM code uses, as standard, a mesh with 40 points per λ. With this set up the SVD spectrum is very flat (green line). Not surprisingly, it turns out that the corresponding cross-term interaction matrix cannot be well approximated with the skeleton method explained in the previous section (ex. no. of skeleton $\sim$ no. of basis function). A faster decaying spectrum is obtained by removing the Green's function interpolation (black line). We note that we are very far from the exponential decay of the free-space case. Moreover, without interpolation, the computational cost of the Green's function is too high for our applications. Nevertheless this level of accuracy is sufficient to provide a compression ratio of 3-5. As a compromise between computational cost and accuracy we find that a finer interpolation mesh with 200 points per λ allows one to recover similar compressibility as for the case of no

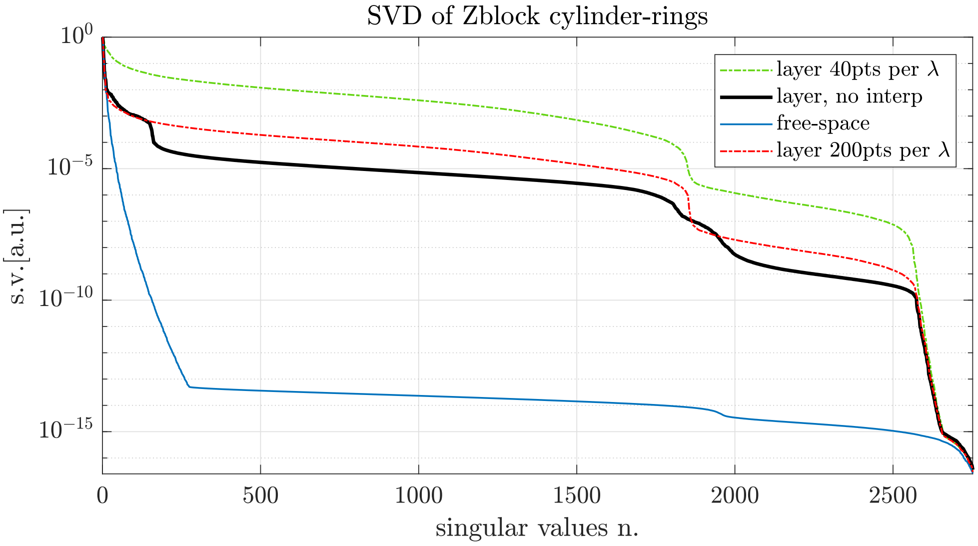

Figure 4.11: SVD singular values of sub-block interaction matrix between cylinder in rings of the feed. Free-space and layered Green's function kernels are used with different level of evaluation accuracy: course interpolation, fine interpolation, no interpolation

interpolation. The computational cost reduction in the calculation of the interaction integrals (without the overhead of the method itself) is thus $(3-10)^2 \approx 10-100$ which is a substantial improvement even without resorting to more complex nested compression schemes.

4.4 Conclusions and Future Work

This chapter presents an unprecedented analysis of different modeling options for the metasurface center-fed antennas. We deal with the full metalization layout (unit cell), and the important issue of the launching structure for the wave that then propagates on the IBC radiating surface. Solutions obtained with IBC and the full layout are compared with one another and with measured data for realized antennas. Impacts and integration of the modeling options onto the IBC approximation for possible integration in the numerical synthesis of Chap. 3 are exposed and discussed. A full-wave method of moment hybrid fast-formulation for the analysis of metasurface antennas [12] is introduced. Thus, for the first time, we introduce in the feed region a realistic 3-D model of the feed. Our formulation comprises a FFT-like method for the co-planar parts (e.g. [5]) of the structure and a skeletonization technique (e.g. [27, 34]) for the remainder of the structure. Numerical results comparing this work to well-known 2-D approximate models of the feed are presented. The technique can also be used to provide a more accurate calculation of the overall feed efficiency. Future investigations will also explore automatic procedures for the numerical optimization of the feed.

Appendix A

Notation

Throughout this paper, an $\exp(\mathrm{j}\omega\mathrm{t})$ time dependence is assumed and suppressed, where ω is the angular frequency. A bold-symbol font is used to denote physical vectors (i.e. elements of $\mathbb{C}^3$ or $\mathbb{R}^3$), single and double underline is used to denote one-dimensional and two-dimensional computational arrays (i.e. arrays and matrices in a numerical code). If $\boldsymbol{f}$ is a vector-valued function which is a linear combination of vector-valued functions $\boldsymbol{q}_\ell$ with coefficients a_ℓ, with $\ell = 1, \dots L$, namely

$$\boldsymbol{f} = \sum_{\ell=1}^{L} a_\ell \boldsymbol{q}_\ell, \tag{A.1}$$

we have that the one-dimensional array which collects the coefficients a_ℓ is $\underline{a}$.

The pseudo-inner product between the vector quantities $\boldsymbol{f}$ and $\boldsymbol{g}$ is defined as:

$$\langle \boldsymbol{f}; \boldsymbol{g} \rangle = \int_{\mathcal{S}} \boldsymbol{f}(\boldsymbol{r}) \cdot \boldsymbol{g}(\boldsymbol{r}) \; d\mathcal{S} \tag{A.2}$$

where $\boldsymbol{r}$ is a three-dimensional vector spanning the surface $\mathcal{S}$.

In integral equation formulations, convolution integral between $\boldsymbol{f}$ and a dyadic Green's function $\boldsymbol{\mathcal{G}}(\boldsymbol{r}, \boldsymbol{r}')$ appears in pseudo-inner product with $\boldsymbol{g}$. This case is expressed via the compact notation:

$$\langle\, \boldsymbol{f};\, \boldsymbol{\mathcal{G}};\, \boldsymbol{g} \,\rangle = \int_{\mathcal{S}} \int_{\mathcal{S}'} \boldsymbol{f}(\boldsymbol{r}) \cdot \boldsymbol{\mathcal{G}}(\boldsymbol{r}, \boldsymbol{r}') \cdot \boldsymbol{g}(\boldsymbol{r}') \; d\mathcal{S}' d\mathcal{S} \tag{A.3}$$

where $\boldsymbol{r}'$ is a three-dimensional vector spanning the surface $\mathcal{S}'$.

Appendix B

Circular and Annular Waveguide Modes

A magnetic eigenfunction, namely $\mathbf{h}$, has the form:

$$\mathbf{h} = h_\rho(\rho) h_\rho(\phi) \hat{\boldsymbol{\rho}} + h_\phi(\phi) h_\phi(\phi) \hat{\boldsymbol{\phi}}. \tag{B.1}$$

where, $h_\rho(\rho)$, $h_\rho(\phi)$, $h_\phi(\phi)$, $h_\phi(\phi)$ are summarized in Table B.1.

Circular waveguide (CWG) spatial frequencies depend on χ_{mn}, which is the nth non-vanishing root of the mth-order Bessel functions $\mathcal{J}_m(\chi_{mn})$, and χ'_{mn}, the nth non-vanishing root of the derivative of the mth-order Bessel functions. Similarly, coaxial (i.e., annular) waveguide (CXWG) modes depend on a different χ_{mn}, which is the nth non-vanishing root of the mth-order Bessel-Neumann combination $\mathcal{Z}_m\left(c\chi_{mn}\right)$, and χ'_{mn}, the nth non-vanishing root of another combination of Bessel-Neumann functions of mth-order $\mathcal{Z}'_m\left(c\chi'_{mn}\right)$. The parameter $c = a/b$ is the ratio between outer and inner radius. The total number of modes in both cases is $N_\Psi = 2N(2M+1)$, where M is the total number of axial modes and N is the total number of radial modes.

B.1 General basis change matrix entries for EBF

The analytic expression of the ℓ-th waveguide-mode, $\mathbf{h}_\ell$, is used to find the RWG representation of the entire-domain basis function (EBF) $\boldsymbol{\Psi}_\ell$:

$$\boldsymbol{\Psi}_\ell = \sum_{p=1}^{N_\Lambda} \Psi_{p\ell} \boldsymbol{\Lambda}_p, \tag{B.2}$$

The coefficients $\Psi_{p\ell}$, with $p = 1, \ldots, N_\Lambda$, are obtained via weighted-residual, enforcing the difference between the analytic expression $\mathbf{h}_\ell$ and its RWG representation $\boldsymbol{\Psi}_\ell$ to be outside the space spanned by the RWG set,

$$\langle \boldsymbol{\Lambda}_\kappa ; \mathbf{h}_\ell - \boldsymbol{\Psi}_\ell \rangle = 0, \ \ \forall_\kappa = 1, .., N_\Lambda. \tag{B.3}$$

where by writing $\boldsymbol{\Psi}_\ell$ as in (2.12) and rearranging the terms, we have the linear system:

$$\sum_{p=1}^{N_\Lambda} \Psi_{p\ell} \langle \boldsymbol{\Lambda}_\kappa ; \boldsymbol{\Lambda}_p \rangle = \langle \boldsymbol{\Lambda}_\kappa ; \mathbf{h}_\ell \rangle, \;\; \forall \kappa = 1, .., N_\Lambda, \tag{B.4}$$

to be solved for $\Psi_{p\ell}$, where on the left-hand side we have the Gram matrix, namely $\underline{\underline{G}}^\Lambda$:

$$G^\Lambda_{\kappa p} = \langle \boldsymbol{\Lambda}_\kappa ; \boldsymbol{\Lambda}_p \rangle = \iint_{\lhd\!\rhd_\kappa \times \lhd\!\rhd_p} \boldsymbol{\Lambda}_\kappa(x,y) \cdot \boldsymbol{\Lambda}_p(x,y)\, dx\, dy \tag{B.5}$$

where $\lhd\!\rhd_\kappa$ and $\lhd\!\rhd_p$ represent the support of the κ-th and p-th RWG, respectively.

Each column of the matrix $\underline{\underline{\Psi}}$ is then obtained solving (B.4). This step represents a negligible computational cost, as the Gram matrix (B.5) on the left-hand side of (B.4) is very sparse, positive-definite, and with condition number $\mathcal{O}(1)$, so that convergence with an iterative solver (e.g. Conjugate Gradient) is attained within few iterations.

$$\underline{\underline{\Psi}} = \begin{bmatrix} \Psi_{1,1} & \dots & \Psi_{1,N_\Psi} \\ \vdots & \Psi_{\kappa,\ell} & \vdots \\ \Psi_{N_\Lambda,1} & \dots & \Psi_{N_\Lambda,N_\Psi} \end{bmatrix} = \begin{bmatrix} \boldsymbol{\Psi}_1 & \dots & \boldsymbol{\Psi}_\ell & \dots & \boldsymbol{\Psi}_{N_\Psi} \end{bmatrix} \tag{B.6}$$

On one hand, the Gram Matrix in the EBF can be calculated by applying the basis change matrix (B.6) to (B.5) as follows:

$$\tilde{\underline{\underline{G}}}^\Psi = \underline{\underline{\Psi}}^T \, \underline{\underline{G}}^\Lambda \, \underline{\underline{\Psi}} \tag{B.7}$$

On the other hand, the Gram Matrix for the EBF can be derived directly from the analytic expressions of the corresponding EBF as

$$\underline{\underline{G}}^\Psi_{\kappa\ell} = \langle \mathbf{h}_\kappa ; \mathbf{h}_\ell \rangle = \iint_{\mathcal{S}} \mathbf{h}_\kappa(x,y) \cdot \mathbf{h}_\ell(x,y)\, dx\, dy = \begin{cases} 1 \text{ if } \kappa = \ell \\ 0 \text{ otherwise} \end{cases} \tag{B.8}$$

where $\mathcal{S}$ is the support of the corresponding EBF. The ∞-norm calculated between these two representations allow us to define the projection error due to the mesh size, when the EBF are use to factorize RWG systems:

$$\delta_h = \left\| \underline{\underline{G}}^\Psi - \tilde{\underline{\underline{G}}}^\Psi \right\|_\infty \tag{B.9}$$

Table B.1: Summary of CWG and CXWG modes for $m = 0,1,\ldots,M$ and $n = 1,2,\ldots,N$.

Support	Mode	Type	$h_\rho(\rho)$	$h_\rho(\phi)$	$h_\phi(\rho)$	$h_\phi(\phi)$
Circular	TM	even	$\mathcal{J}_m\left(\frac{\chi_{mn}}{a}\rho\right)$	$\sin m\phi$	$\mathcal{J}'_m\left(\frac{\chi_{mn}}{a}\rho\right)$	$\cos m\phi$
		odd		$\cos m\phi$		$\sin m\phi$
	TE	even	$\mathcal{J}'_m\left(\frac{\chi'_{mn}}{a}\rho\right)$	$\cos m\phi$	$\mathcal{J}_m\left(\frac{\chi'_{mn}}{a}\rho\right)$	$\sin m\phi$
		odd		$\sin m\phi$		$\cos m\phi$
Annular	TM	even	$\mathcal{Z}_m\left(\frac{\chi_{mn}}{b}\rho\right)$	$\sin m\phi$	$\mathcal{Z}'_m\left(\frac{\chi_{mn}}{b}\rho\right)$	$\cos m\phi$
		odd		$\cos m\phi$		$\sin m\phi$
	TE	even	$\mathcal{Z}'_m\left(\frac{\chi'_{mn}}{b}\rho\right)$	$\cos m\phi$	$\mathcal{Z}_m\left(\frac{\chi'_{mn}}{b}\rho\right)$	$\sin m\phi$
		odd		$\sin m\phi$		$\cos m\phi$
	TEM				$\frac{1}{\rho}$	

Appendix C

Annular Entire Domain Basis Functions

C.1 Fast Far-field Radiation: Supplementary material

For non-stationary phase points, which have to be integrated in dr', $\hat{\boldsymbol{u}} \neq \hat{\boldsymbol{\rho}}$ and $\hat{\boldsymbol{\phi}} \neq \hat{\boldsymbol{v}}$, then we have:

$$\begin{cases} \hat{\boldsymbol{\rho}} = \cos\varphi \hat{\boldsymbol{x}} + \sin\varphi \hat{\boldsymbol{y}} \\ \hat{\boldsymbol{\phi}} = -\sin\varphi \hat{\boldsymbol{x}} + \cos\varphi \hat{\boldsymbol{y}} \end{cases} , \quad \begin{cases} \hat{\boldsymbol{u}} = \cos\phi' \hat{\boldsymbol{x}} + \sin\phi' \hat{\boldsymbol{y}} \\ \hat{\boldsymbol{v}} = -\sin\phi' \hat{\boldsymbol{x}} + \cos\phi' \hat{\boldsymbol{y}} \end{cases} \tag{C.1}$$

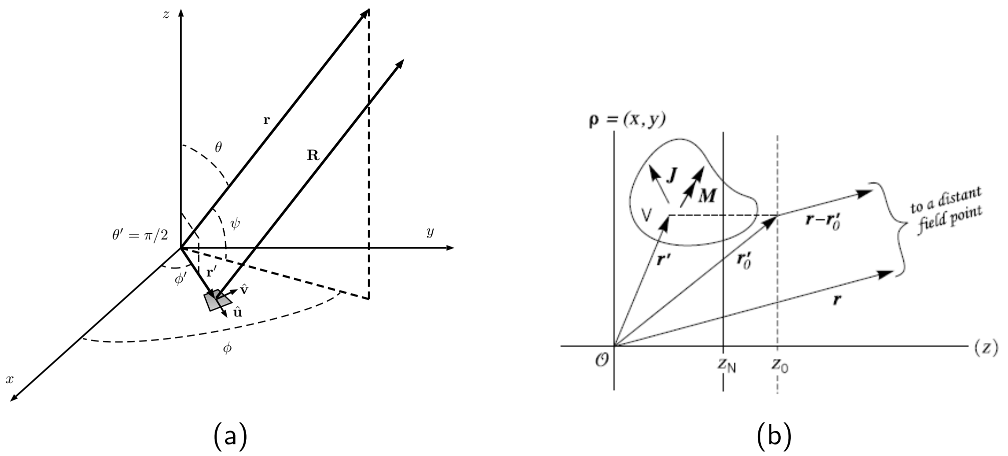

(a) (b)

Figure C.1: Geometrical background for far-field derivation. Left(a): 3d view. Right(b): ρz view.

Thus

$$\begin{aligned}\hat{\boldsymbol{u}} &= (\cos\phi'\cos\varphi + \sin\phi'\sin\varphi)\,\hat{\boldsymbol{\rho}} + (-\cos\phi'\sin\varphi + \sin\phi'\cos\varphi)\,\hat{\boldsymbol{\phi}} \qquad \text{(C.2)}\\ \hat{\boldsymbol{v}} &= (-\sin\phi'\cos\varphi + \cos\phi'\sin\varphi)\,\hat{\boldsymbol{\rho}} + (\sin\phi'\sin\varphi + \cos\phi'\cos\varphi)\,\hat{\boldsymbol{\phi}} \qquad \text{(C.3)}\end{aligned}$$

which can be rewritten as

$$\begin{aligned}\hat{\boldsymbol{u}} &= \cos(\phi'-\varphi)\,\hat{\boldsymbol{\rho}} + \sin(\phi'-\varphi)\,\hat{\boldsymbol{\phi}} \qquad \text{(C.4)}\\ \hat{\boldsymbol{v}} &= -\sin(\phi'-\varphi)\,\hat{\boldsymbol{\rho}} + \cos(\phi'-\varphi)\,\hat{\boldsymbol{\phi}}. \qquad \text{(C.5)}\end{aligned}$$

In the background scenario described in sec.3.2, we can calculate the following integrals:

$$\mathcal{F}^J_\vartheta = V^e_i(z_0|z')\int_b^a d\rho'\rho' \begin{cases} g(\rho')\mathcal{I}^{cos}_1, \text{ even symmetry}\\ -l(\rho')\mathcal{I}^{sin}_1, \text{ odd symmetry}\end{cases} \qquad \text{(C.6)}$$

$$\mathcal{F}^J_\varphi = \cos\vartheta V^h_i(z_0|z')\int_b^a d\rho'\rho' \begin{cases} g(\rho')\mathcal{I}^{cos}_2, \text{ even symmetry}\\ l(\rho')\mathcal{I}^{sin}_2, \text{ odd symmetry}\end{cases} \qquad \text{(C.7)}$$

Integration along ϕ'

$$\mathcal{I}^{\cos}_1 = \frac{1}{2}\left(\mathcal{I}^{m+1}_{\cos} + \mathcal{I}^{m-1}_{\cos}\right) \qquad \text{(C.8)}$$

$$\mathcal{I}^{\sin}_1 = \frac{1}{2}\left(\mathcal{I}^{m+1}_{\sin} + \mathcal{I}^{m-1}_{\sin}\right) \qquad \text{(C.9)}$$

$$\mathcal{I}^{\cos}_2 = \frac{1}{2}\left(\mathcal{I}^{m+1}_{\sin} - \mathcal{I}^{m-1}_{\sin}\right) \qquad \text{(C.10)}$$

$$\mathcal{I}^{\sin}_2 = -\frac{1}{2}\left(\mathcal{I}^{m+1}_{\cos} - \mathcal{I}^{m-1}_{\cos}\right) \qquad \text{(C.11)}$$

where

$$\mathcal{I}^{m+1}_{\cos} = \pi e^{jm\varphi}\left(\frac{\mathcal{J}_{m+1}(x)}{(-j)^{m+1}} + \frac{\mathcal{J}_{m+1}(-x)}{(+j)^{m+1}}\right) \qquad \text{(C.12)}$$

$$\mathcal{I}^{m-1}_{\cos} = \pi e^{jm\varphi}\left(\frac{\mathcal{J}_{m-1}(x)}{(-j)^{m-1}} + \frac{\mathcal{J}_{m-1}(-x)}{(+j)^{m-1}}\right) \qquad \text{(C.13)}$$

$$\mathcal{I}^{m+1}_{\sin} = \pi e^{j\left(m\varphi-\frac{\pi}{2}\right)}\left(\frac{\mathcal{J}_{m+1}(x)}{(-j)^{m+1}} + \frac{\mathcal{J}_{m+1}(-x)}{(+j)^{m+1}}\right) \qquad \text{(C.14)}$$

$$\mathcal{I}^{m-1}_{\sin} = \pi e^{j\left(m\varphi-\frac{\pi}{2}\right)}\left(\frac{\mathcal{J}_{m-1}(x)}{(-j)^{m-1}} + \frac{\mathcal{J}_{m-1}(-x)}{(+j)^{m-1}}\right) \qquad \text{(C.15)}$$

Integration of (C.8)

If $h(\phi') = \cos m\phi'$ we integrate along ϕ' as follows:

$$\begin{aligned}
\mathcal{I}_1^{\cos} &= \int_{-\pi}^{\pi} d\phi' h(\phi') \cos(\phi' - \varphi)\, e^{j\mathbf{k}_\rho^s \cdot \boldsymbol{\rho}'} \\
&= \int_{-\pi}^{\pi} d\phi' \cos(\phi' - \varphi) \cos m\phi' e^{j\mathbf{k}_\rho^s \cdot \boldsymbol{\rho}'} \\
&= \frac{1}{2}\left[\underbrace{\int_{-\pi}^{\pi} d\phi' \cos((m+1)\phi' - \varphi)\, e^{j\mathbf{k}_\rho^s \cdot \boldsymbol{\rho}'}}_{\mathcal{I}_{\cos}^{m+1}} + \underbrace{\int_{-\pi}^{\pi} d\phi' \cos((m-1)\phi' + \varphi)\, e^{j\mathbf{k}_\rho^s \cdot \boldsymbol{\rho}'}}_{\mathcal{I}_{\cos}^{m-1}}\right] \\
&= \frac{1}{2}\left(\mathcal{I}_{\cos}^{m+1} + \mathcal{I}_{\cos}^{m-1}\right) \qquad \text{(C.16)}
\end{aligned}$$

Let us evaluate the following integrals:

$$\begin{aligned}
\mathcal{I}_{\cos}^{m} &= \int_{-\pi}^{\pi} d\phi' \cos(m\phi' \pm \varphi)\, e^{j\mathbf{k}_\rho^s \cdot \boldsymbol{\rho}'} \\
&= \int_{-\pi}^{\pi} d\phi' \cos(m\phi' + m\varphi - m\varphi \pm \varphi)\, e^{jxcos(\phi' - \varphi)} \\
&= \int_{-\pi}^{\pi} d\phi' \cos(m(\phi' - \varphi) + (m \pm 1)\varphi)\, e^{jxcos(\phi' - \varphi)} \\
&= \int_{-\pi}^{\pi} d\phi' \cos(\alpha + \beta)\, e^{jxcos(\phi' - \varphi)} \\
&= \int_{-\pi}^{\pi} d\phi' \left[\cos\alpha \cos\beta - \sin\beta \sin\alpha\right] e^{jxcos(\phi' - \varphi)} \\
&= \cos\beta \int_{-\pi}^{\pi} d\phi' \cos\alpha e^{jxcos(\phi' - \varphi)} - \sin\beta \int_{-\pi}^{\pi} d\phi' \sin\alpha e^{jxcos(\phi' - \varphi)} \\
&= \cos\beta \underbrace{\int_{-\pi}^{\pi} d\phi' \cos(m(\phi' - \varphi))\, e^{jxcos(\phi' - \varphi)}}_{\mathcal{I}_{\cos}^{\mathcal{J}}} \\
&\quad - \sin\beta \underbrace{\int_{-\pi}^{\pi} d\phi' \sin(m(\phi' - \varphi))\, e^{jxcos(\phi' - \varphi)}}_{\mathcal{I}_{\sin}^{\mathcal{J}}} \qquad \text{(C.17)}
\end{aligned}$$

where

$$\begin{aligned}
\mathcal{I}^{\mathcal{J}}_{\cos} &= \int_{-\pi}^{\pi} d\phi' \cos\left(m(\phi'-\varphi)\right) e^{jxcos(\phi'-\varphi)} \\
&= \frac{1}{2}\int_{-\pi}^{\pi} d\phi' e^{j[xcos(\phi'-\varphi)+m(\phi'-\varphi)]} + \frac{1}{2}\int_{-\pi}^{\pi} d\phi' e^{-j[(-x)cos(\phi'-\varphi)+m(\phi'-\varphi)]} \\
&= \frac{1}{2}\left(\frac{2\pi}{(-j)^m}\mathcal{J}_m(x) + \frac{2\pi}{(+j)^m}\mathcal{J}_m(-x)\right) \qquad \text{(C.18)}
\end{aligned}$$

and

$$\begin{aligned}
\mathcal{I}^{\mathcal{J}}_{\sin} &= \int_{-\pi}^{\pi} d\phi' \sin\left(m(\phi'-\varphi)\right) e^{jxcos(\phi'-\varphi)} \\
&= \frac{1}{2j}\int_{-\pi}^{\pi} d\phi' e^{j[xcos(\phi'-\varphi)+m(\phi'-\varphi)]} - \frac{1}{2j}\int_{-\pi}^{\pi} d\phi' e^{-j[(-x)cos(\phi'-\varphi)+m(\phi'-\varphi)]} \\
&= \frac{1}{2j}\left(\frac{2\pi}{(-j)^m}\mathcal{J}_m(x) - \frac{2\pi}{(+j)^m}\mathcal{J}_m(-x)\right) \qquad \text{(C.19)}
\end{aligned}$$

Thus

$$\begin{aligned}
\mathcal{I}^{m}_{\cos} &= \int_{-\pi}^{\pi} d\phi' \cos\left(m\phi' \pm \varphi\right) e^{j\mathbf{k}^s_\rho\cdot\boldsymbol{\rho}'} \\
&= \frac{\cos\left((m\pm 1)\varphi\right)}{2}\left(\frac{2\pi}{(-j)^m}\mathcal{J}_m(x) + \frac{2\pi}{(+j)^m}\mathcal{J}_m(-x)\right) \\
&\quad -\frac{\sin\left((m\pm 1)\varphi\right)}{2j}\left(\frac{2\pi}{(-j)^m}\mathcal{J}_m(x) - \frac{2\pi}{(+j)^m}\mathcal{J}_m(-x)\right) \qquad \text{(C.20)}
\end{aligned}$$

It follows that

$$\begin{aligned}
\mathcal{I}^{m+1}_{\cos} &= \int_{-\pi}^{\pi} d\phi' \cos\left((m+1)\phi' - \varphi\right) e^{j\mathbf{k}^s_\rho\cdot\boldsymbol{\rho}'} \\
&= \pi\cos(m\varphi)\left(\frac{\mathcal{J}_{m+1}(x)}{(-j)^{m+1}} + \frac{\mathcal{J}_{m+1}(-x)}{(+j)^{m+1}}\right) \\
&\quad +j\pi\sin(m\varphi)\left(\frac{\mathcal{J}_{m+1}(x)}{(-j)^{m+1}} - \frac{\mathcal{J}_{m+1}(-x)}{(+j)^{m+1}}\right) \\
&= \pi e^{jm\varphi}\left(\frac{\mathcal{J}_{m+1}(x)}{(-j)^{m+1}} + \frac{\mathcal{J}_{m+1}(-x)}{(+j)^{m+1}}\right) \qquad \text{(C.21)}
\end{aligned}$$

In a straightforward similar manner the integration for the eqs. (C.13), (C.14), (C.15) can be performed. The knowledge of closed-form integrals leads via eqs. (C.8), (C.9), (C.10) and (C.11) to the knowledge of the closed-form integration along ϕ of the far-field radiation integral described in section 3.2.

C.2 IBC MoM Matrix Entries: Supplementary material

$$\begin{aligned}
\langle \mathbf{h}_\ell ; \mathcal{X}\cdot \mathbf{h}_m \rangle &= \underbrace{\int_b^a \int_{-\pi}^{\pi} f_\ell^\rho(\rho) g_\ell^\rho(\phi) \left(X_{\rho\rho} + X_{\rho\phi}\right) f_m^\rho(\rho) g_m^\rho(\phi) \rho \, d\rho \, d\phi}_{\mathcal{I}^\rho} \\
&\quad + \underbrace{\int_b^a \int_{-\pi}^{\pi} f_\ell^\phi(\rho) g_\ell^\phi(\phi) \left(X_{\phi\phi} + X_{\rho\phi}\right) f_m^\phi(\rho) g_m^\phi(\phi) \rho \, d\rho \, d\phi}_{\mathcal{I}^\phi} \\
&= \left(\mathcal{I}^\rho + \mathcal{I}^\phi\right) \qquad \text{(C.22)}
\end{aligned}$$

where

$$\begin{aligned}
\mathcal{I}^\rho &= x_{\rho\rho} \int_b^a f_\ell^\rho(\rho) f_m^\rho(\rho) \rho \, d\rho \int_{-\pi}^{\pi} g_\ell^\rho(\phi) g_m^\rho(\phi) \, d\phi \\
&\quad + \sum_{k=1}^{K} \left(x_k^{\rho\rho} + x_k^{\rho\phi}\right) \int_b^a f_\ell^\rho(\rho) f_k(\rho) f_m^\rho(\rho) \rho \, d\rho \underbrace{\int_{-\pi}^{\pi} g_\ell^\rho(\phi) g_m^\rho(\phi) \cos(k\phi) \, d\phi}_{\mathcal{I}^\rho_{\cos}} + \\
&\quad + \sum_{k=1}^{K} \left(x_k^{\rho\rho} + x_k^{\rho\phi}\right) \int_b^a f_\ell^\rho(\rho) f_k(\rho) f_m^\rho(\rho) \rho \, d\rho \underbrace{\int_{-\pi}^{\pi} g_\ell^\rho(\phi) g_m^\rho(\phi) \sin(k\phi) \, d\phi}_{\mathcal{I}^\rho_{\sin}}
\end{aligned} \qquad \text{(C.23)}$$

The same derivation can be made for $\mathcal{I}^\phi$. Summarizing, we have to solve 10 different integrals along $\hat{\boldsymbol{\rho}}$ (the 8 shown below plus 2 for EBF Gram Matrix for constant average reactance terms):

- $\ell, m, k \in \mathbb{N}^*$

i	g_ℓ	g_m	g_k	$\mathcal{I}_i$
1	$\cos \ell\phi$	$\cos m\phi$	$\cos k\phi$	$\pi/2$
2	$\sin \ell\phi$			0
3	$\cos \ell\phi$	$\sin m\phi$		0
4	$\sin \ell\phi$			$\pm\pi/2$
5	$\cos \ell\phi$	$\cos m\phi$	$\sin k\phi$	0
6	$\sin \ell\phi$			$\pm\pi/2$
7	$\cos \ell\phi$	$\sin m\phi$		$\pm\pi/2$
8	$\sin \ell\phi$			0

- $\nexists \ell, m, k \in \mathbb{N}^*$ s.t. $(\ell + m + k) \neq 0$
- the integration has to be performed only when $(\ell - m - k) = 0$, $(\ell + m - k) = 0$ or $(\ell - m + k) = 0$. Otherwise all the other integrals vanish;
- the sign of each integral depends on which of the 3 possible index combinations is satisfied;
- integrals $\mathcal{I}_1, \mathcal{I}_4$ have to be computed for $k = 1, \ldots, K$;
- integrals $\mathcal{I}_6, \mathcal{I}_7$ have to be computed for $k = 1, \ldots, K$.

Appendix D

Rectangular Entire Domain Basis Functions

The magnetic eigenfunction are defined in a cartesian coordinate system xy as:

$$\mathbf{h} = h_x(x,y)\hat{\boldsymbol{x}} + h_y(x,y)\hat{\boldsymbol{y}} \tag{D.1}$$

Both h_x and h_y are defined over a rectangular domain $\mathcal{R}$ centred in $\mathcal{O} = (0{,}0)$ with sides a and b along $\hat{\boldsymbol{x}}$ and $\hat{\boldsymbol{y}}$ directions, respectively.

The TM modes associated to (D.1) for $m,n = 1{,}2{,}3,\ldots$ are:

$$h_x(x,y) = \frac{2}{b}\frac{n}{\sqrt{m^2\frac{b}{a}+n^2\frac{a}{b}}}\sin\frac{m\pi}{a}x\cos\frac{n\pi}{b}y \tag{D.2}$$

$$h_y(x,y) = -\frac{2}{a}\frac{m}{\sqrt{m^2\frac{b}{a}+n^2\frac{a}{b}}}\cos\frac{m\pi}{a}x\sin\frac{n\pi}{b}y, \tag{D.3}$$

The TE modes for $m,n = 0{,}1{,}2{,}3,\ldots$ are

$$h_x(x,y) = \frac{2}{a}\frac{m}{\sqrt{m^2\frac{b}{a}+n^2\frac{a}{b}}}\sin\frac{m\pi}{a}x\cos\frac{n\pi}{b}y \tag{D.4}$$

$$h_y(x,y) = \frac{2}{b}\frac{n}{\sqrt{m^2\frac{b}{a}+n^2\frac{a}{b}}}\cos\frac{m\pi}{a}x\sin\frac{n\pi}{b}y. \tag{D.5}$$

where the mode $m,n = 0$ is excluded.

D.1 Fast Far Field Radiation: Derivations

Rectangular EBF can be generally written as a planar electric current over the rectangular domain $\mathcal{R} = [-a/2, a/2] \times [-b/2, b/2]$:

$$\begin{aligned} \boldsymbol{J}(x', y') &= J_x(x', y')\hat{\boldsymbol{x}}' + J_y(x', y')\hat{\boldsymbol{y}}' \\ &= J_{xx}(x')J_{xy}(y')\hat{\boldsymbol{x}}' + J_{yx}(x')J_{yy}(y')\hat{\boldsymbol{y}}' \end{aligned} \tag{D.6}$$

and then from eq. (162) of [31]

$$E_{\vartheta,\varphi} \approx \frac{e^{-jk_N r}}{2\pi j r} e^{-jk^s_{zN} z_0} k_N \underbrace{\langle \boldsymbol{f}_{\vartheta,\varphi} e^{j\mathbf{k}^s_\rho \cdot \boldsymbol{\rho}'} ; \boldsymbol{J} \rangle}_{\mathcal{F}^J_{\vartheta,\varphi}} \tag{D.7}$$

where

$$\boldsymbol{f}^{EJ}_{\vartheta} = V^e_i(z_0|z') \left(\cos\varphi \hat{\boldsymbol{x}} + \sin\varphi \hat{\boldsymbol{y}}\right) \tag{D.8}$$

and

$$\boldsymbol{f}^{EJ}_{\varphi} = \cos\vartheta V^h_i(z_0|z') \left(-\sin\varphi \hat{\boldsymbol{x}} + \cos\varphi \hat{\boldsymbol{y}}\right) \tag{D.9}$$

and

$$\begin{aligned} e^{j\mathbf{k}^s_\rho \cdot \boldsymbol{\rho}'} &= e^{jk_0 x' \sin\vartheta \cos\varphi} e^{jk_0 y' \sin\vartheta \sin\varphi} \\ &= e^{jk_x x'} e^{jk_y y'} \end{aligned} \tag{D.10}$$

where

$$k_x = k_0 \sin\vartheta \cos\varphi \tag{D.11}$$

$$k_y = k_0 \sin\vartheta \sin\varphi \tag{D.12}$$

Then $\mathcal{F}^J_\vartheta$ from (D.7) can be divided in $\hat{\boldsymbol{x}}$ and $\hat{\boldsymbol{y}}$ component as follows:

$$\begin{aligned} \mathcal{F}^{J_x}_\vartheta &= \cos\varphi V^e_i(z_0|z') \iint_{\mathcal{R}} J_x(x', y') e^{jk_0 x' \sin\vartheta\cos\varphi} e^{jk_0 y' \sin\vartheta \sin\varphi}\, dx' dy' \\ &= \cos\varphi V^e_i(z_0|z') \underbrace{\int_{-a/2}^{a/2} J_{xx}(x') e^{jk_x x'}\, dx'}_{\mathrm{F}_x\{J_{xx}(x')\Pi(x'/a)\}} \underbrace{\int_{-b/2}^{b/2} J_{xy}(y') e^{jk_y y'}\, dy'}_{\mathrm{F}_y\{J_{xy}(y')\Pi(y'/a)\}} \end{aligned} \tag{D.13}$$

where for instance $\mathrm{F}_x\{\}$ indicates the Fourier Transform along the direction x. Then we have:

$$\mathcal{F}^{J_y}_\vartheta = \sin\varphi V^e_i(z_0|z') \mathrm{F}_x\{J_{yx}(x')\Pi(x'/a)\} \mathrm{F}_y\{J_{yy}(y')\Pi(y'/a)\} \tag{D.14}$$

Similarly, for $\mathcal{F}^J_\varphi$ we obtain:

$$\mathcal{F}^{J_x}_\varphi = -\sin\varphi \cos\vartheta V^h_i(z_0|z') \mathrm{F}_x\{J_{xx}(x')\Pi(x'/a)\} \mathrm{F}_y\{J_{xy}(y')\Pi(y'/a)\} \tag{D.15}$$

and

$$\mathcal{F}^{J_y}_\varphi = \cos\varphi \cos\vartheta V^h_i(z_0|z') \mathrm{F}_x\{J_{yx}(x')\Pi(x'/a)\} \mathrm{F}_y\{J_{yy}(y')\Pi(y'/a)\} \tag{D.16}$$

References

[1] A. M. Patel and A. Grbic. “Effective Surface Impedance of a Printed-Circuit Tensor Impedance Surface”. In: *IEEE Trans. on Microw. Theory and Techn.* 32.4 (2013), pp. 1403–1413. DOI: 10.1109/TMTT.2013.2252362.

[2] A. M. Patel and A. Grbic. “Modeling and Analysis of Printed-Circuit Tensor Impedance Surfaces”. In: *IEEE Trans. on Antennas and Propag.* 61.1 (2013), pp. 211–220. DOI: 10.1109/TAP.2012.2220092.

[3] M. Faenzi et al. “Metasurface Antennas: New Models, Applications and Realizations”. In: *Sci Rep* 10178.9 (2019). DOI: https://doi.org/10.1038/s41598-019-46522-z.

[4] A. Li et al. “Metasurfaces and Their Application”. In: *IEEE Trans. on Antennas and Propag.* 7.6 (2018), pp. 989–1011. DOI: 10.1515/nanoph-2017-0120.

[5] B. J. Fasenfest et al. “A Fast MoM Solution for Large Arrays: Green’s Function Interpolation with FFT”. In: *IEEE Antennas and Wireless Propag. Lett.* 3.3 (2004), pp. 161–164. DOI: 10.1109/LAWP.2004.833713.

[6] C. L. Holloway et al. “An Overview of the Theory and Applications of Metasurfaces: The Two-Dimensional Equivalents of Metamaterials”. In: *IEEE Antennas and Propag. Magazine* 54.2 (2012), pp. 10–35. DOI: 10.1109/MAP.2012.6230714.

[7] D. González-Ovejero et al. “Additive Manufactured Metal-Only Modulated Metasurface Antennas”. In: *IEEE Trans. on Antennas and Propag.* 66.11 (2018), pp. 6106–6114. DOI: 10.1109/TAP.2018.2869135.

[8] E. F. Kuester et al. “Averaged Transition Conditions for Electromagnetic Fields at a Metafilm”. In: *IEEE Trans. on Antennas and Propag.* 51.10 (2003), pp. 2641–2651. DOI: 10.1109/TAP.2003.817560.

[9] F. Vernì et al. “Entire-Domain Spectral Basis Functions for the Efficient Design of Metasurface Antennas of Circular Shape”. In: *Int. Symp. on Antennas and Propag. and USNC/URSI Nat. Radio Sci. Meeting* (Boston, USA). Ed. by IEEE. 2018, pp. 2361–2362. DOI: 10.1109/APUSNCURSINRSM.2018.8608462.

[10] F. Vipiana et al. "A Mesh-Adapted Closed-Form Regular Kernel for 3D Singular Integral Equations". In: *IEEE Trans. on Antennas and Propag.* 56.6 (2008), pp. 508–519. DOI: `10.1109/TAP.2008.923334`.

[11] F. Vipiana et al. "Spectral Properties of the EFIE-MoM Matrix for Dense Meshes With Different Types of Bases". In: *IEEE Trans. on Antennas and Propag.* 55.11 (2007), pp. 508–519. DOI: `10.1109/TAP.2007.908827`.

[12] G. Minatti et al. "Flat Optics for Leaky-Waves on Modulated Metasurfaces: Adiabatic Floquet-Wave Analysis". In: *IEEE Trans. on Antennas and Propag.* 64.9 (2016), pp. 3896–3906. DOI: `10.1109/TAP.2016.2590559`.

[13] G. Minatti et al. "Modulated Metasurface Antennas for Space: Synthesis, Analysis and Realizations". In: *IEEE Trans. on Antennas and Propag.* 63.4 (2015), pp. 1288–1300. DOI: `10.1109/TAP.2014.2377718`.

[14] G. Minatti et al. "Spiral Leaky-Wave Antennas Based on Modulated Surface Impedance". In: *IEEE Trans. on Antennas and Propag.* 59.12 (2011), pp. 4436–4444. DOI: `10.1109/TAP.2011.2165691`.

[15] G. Vecchi et al. "A Numerical Regularization of the EFIE for Three-dimensional Planar Structures in Layered Media". In: *Int. J. of Microw. and Millimeter-Wave Comput.-Aided Eng.* Ed. by John Wiley and Sons. 1997, pp. 410–431. DOI: `10.1002/(SICI)1522-6301(199711)7:6<410::AID-MMCE4>3.0.CO;2-R`.

[16] G. Vecchi et al. "Hybrid Spectral-Spatial Method for the Analysis of Printed Antennas". In: *Radio Sci.* 31.5 (1996), pp. 1263–1270. DOI: `10.1029/96RS01096`.

[17] G. Vecchi et al. "On the Use of Cavity Modes as Basis Functions in the Full Wave Analysis of Printed Antennas". In: *IEEE Trans. on Antennas and Propag.* 46.4 (1998), pp. 589–594. DOI: `10.1109/8.664125`.

[18] M. A. Francavilla et al. "On the Numerical Simulation of Metasurfaces With Impedance Boundary Condition Integral Equations". In: *IEEE Trans. on Antennas and Propag.* 63.5 (2015), pp. 4436–4444. DOI: `10.1109/TAP.2015.2407372`.

[19] M. Bodehou et al. "Method of Moments Simulation of Modulated Metasurface Antennas With a Set of Orthogonal Entire-Domain Basis Functions". In: *IEEE Trans. on Antennas and Propag.* 67.2 (2019), pp. 1119–1130. DOI: `10.1109/TAP.2018.2880075`.

[20] M. Bodehou et al. "Numerical Analysis of Modulated Metasurface Antennas using Fourier-Bessel Basis Functions". In: *MTT-S Int. Conf. on Numer. Electromagn. and Multiphys. Model. and Optim. for RF, Microw., and Terahertz Appl. (NEMO)* (Seville, Spain). Ed. by IEEE. 2017, pp. 158–160. DOI: `10.1109/NEMO.2017.7964219`.

[21] M. Bodehou et al. "Numerical Analysis of Modulated Metasurface Antennas using Fourier-Bessel Basis Functions". In: *IEEE Antennas and Wireless Propag. Lett.* 17.4 (2018), pp. 675–678. DOI: `10.1109/LAWP.2018.2811620`.

[22] S. Ali et al. “Vector Hankel Transform Analysis of Annular-Ring Microstrip Antenna”. In: *IEEE Trans. on Antennas and Propag.* 30.4 (1982), pp. 637–644. DOI: 10.1109/TAP.1982.1142870.

[23] S. Pandi et al. “Design of Scalar Impedance Holographic Metasurfaces for Antenna Beam Formation With Desired Polarization”. In: *IEEE Trans. on Antennas and Propag.* 63.7 (2015), pp. 3016–3024. DOI: 10.1109/TAP.2015.2426832.

[24] S. Rao et al. “Electromagnetic Scattering by Surfaces of Arbitrary Shape”. In: *IEEE Trans. on Antennas and Propag.* 30.3 (1982), pp. 409–418. DOI: 10.1109/TAP.1982.1142818.

[25] J. L. Araque Quijano and G. Vecchi. “Alternating Adaptive Projections in Antenna Synthesis”. In: *IEEE Transactions on Antennas and Propagation* 58.3 (2010), pp. 727–737. DOI: 10.1109/TAP.2009.2039307.

[26] C. Balanis. In: *Antenna Theory*. Ed. by Wiley-Interscience. 2005.

[27] M. A. E. Bautista et al. “$\mathcal{O}(N)$ Nested Skeletonization Scheme for the Analysis of Multiscale Structures Using the Method of Moments”. In: *IEEE Journal on Multiscale and Multiphysics Computational Techniques* 1 (2016), pp. 139–150. DOI: 10.1109/JMMCT.2016.2645838.

[28] W. C. Chew et al. “Analysis of a probe-fed microstrip disk antenna”. In: *IEE Proceedings H - Microwaves, Antennas and Propagation* 138.2 (1991), pp. 185–191. DOI: 10.1049/ip-h-2.1991.0030.

[29] D. González-Ovejero and S. Maci. “Gaussian Ring Basis Functions for the Analysis of Modulated Metasurface Antennas”. In: *IEEE Trans. on Antennas and Propag.* 63.9 (2015), pp. 3982–3993. DOI: 10.1109/TAP.2015.2442585.

[30] N. Marcuvitz. “Transmission-line modes”. In: *Waveguide Handbook*. Ed. by McGraw-Hill. Vol. 21. IEE Electromagn. Waves Series. 2003. Chap. 2, pp. 55–100.

[31] K. A. Michalski and J. R. Mosig. “Multilayered Media Green’s Functions in Integral Equation Formulations”. In: *IEEE Trans. on Antennas and Propag.* 45.3 (1997), pp. 508–519. DOI: 10.1109/8.558666.

[32] A. Oliner and A. Hessel. “Guided waves on sinusoidally-modulated reactance surfaces”. In: *IRE Transactions on Antennas and Propagation* 7.5 (1959), pp. 201–208. DOI: 10.1109/TAP.1959.1144771.

[33] A. M. Patel and A. Grbic. “A Printed Leaky-Wave Antenna Based on a Sinusoidally-Modulated Reactance Surface”. In: *IEEE Transactions on Antennas and Propagation* 59.6 (2011), pp. 2087–2096. DOI: 10.1109/TAP.2011.2143668.

[34] Z. Peng et al. “High-Fidelity, High-Performance Computational Algorithms for Intrasystem Electromagnetic Interference Analysis of IC and Electronics”. In: *IEEE Transactions on Components, Packaging and Manufacturing Technology* 7.5 (2017), pp. 653–668. DOI: 10.1109/TCPMT.2016.2636296.

[35] C. Pfeiffer and A. Grbic. "Cascaded Metasurfaces for Complete Phase and Polarization Control". In: *Appl. Phys. Lett.* 102.23 (2013), pp. 1263–1270. DOI: 10.1063/1.4810873.

[36] M. Ranjbar and A. Grbic. "Analysis and Synthesis of Cascaded Metasurfaces using Wave Matrices". In: *Int. Symp. on Antennas and Propag. and USNC/URSI Nat. Radio Sci. Meeting* (Fajardo, Puerto Rico). Ed. by IEEE. 2016, pp. 103–104. DOI: 10.1109/APS.2016.7695760.

[37] Y. Saad. "Krylov Subspace Methods Part I". In: *Iterative Methods for Sparse Linear Systems*. Ed. by SIAM (Soc. Ind. Appl. Math.) 2003. Chap. 6, pp. 171–193.

[38] T. J. Cui and W. C. Chew. "Accurate model of arbitrary wire antennas in free space, above or inside ground". In: *IEEE Transactions on Antennas and Propagation* 48.4 (2000), pp. 482–493. DOI: 10.1109/8.843661.

[39] S. Tretyakov. "Interfaces and Higher–Order Boundary Conditions". In: *Analytical Modeling in Applied Electromagnetics*. Ed. by Artech House. 2003. Chap. 3, pp. 44–46.

[40] F. Vernì, M. Righero, and G. Vecchi. "On the Use of Entire-Domain Basis Functions and Fast Factorizations for the Design of Modulated Metasurface". In: *IEEE Transactions on Antennas and Propagation* 68.5 (2020), pp. 3824–3833. DOI: 10.1109/TAP.2020.2966040.

This Ph.D. thesis has been typeset by means of the TEX-system facilities. The typesetting engine was pdfLATEX. The document class was `toptesi`, by Claudio Beccari, with option `tipotesi =scudo`. This class is available in every up-to-date and complete TEX-system installation.